FORSCHUNGSZENTRUM ROSSENDORF FZR

WISSENSCHAFTLICH-TECHNISCHE BERICHTE
FZR-320
Mai 2001
ISSN 1437-322X

Editor: Horst-Michael Prasser

4. Workshop

Measurement techniques of stationary and transient multiphase flow

Rossendorf, November 16 - 17, 2000

Forschungszentrum Rossendorf e. V.
Mitglied der Wissenschaftsgemeinschaft Gottfried Wilhelm Leibniz

Herausgeber:
Forschungszentrum Rossendorf e.V.
Postfach 51 01 19
D-01314 Dresden
Telefon +49 351 26 00
Telefax +49 351 2 69 04 61
http://www.fz-rossendorf.de/

Als Manuskript gedruckt

FORSCHUNGSZENTRUM ROSSENDORF
WISSENSCHAFTLICH-TECHNISCHE BERICHTE
FZR-320
Mai 2001

Editor: Horst-Michael Prasser

4. Workshop

Measurement techniques of stationary and transient multiphase flow

Rossendorf, November 16 - 17, 2000

CONTENT

Preface

In November 2000, the 4th Workshop on **Measurement Techniques for Stationary and Transient Multiphase Flows** took place in Rossendorf. Three previous workshops of this series were national meetings; this time participants from different countries took part. The programme comprised 14 oral presentations, 9 of which are included in these proceedings in full length. A special highlight of the meeting was the main lecture "Ultrasonic doppler method for bubbly flow measurement" of Professor Masanori Aritomi, Dr. Hiroshige Kikura and Dr. Yumiko Suzuki, which was read by Dr. Hiroshige Kikura.

The workshop again dealt with high-resolution phase distribution and phase velocity measurement techniques based on electrical conductivity, ultrasound, laser light and high-speed cinematography. A number of presentations were dedicated to the application of wire-mesh sensors developed by FZR for different applications used by the Technical Universities of Delft and Munich and the Tokyo Institute of Technology.

We would like to continue the tradition of the workshop in Rossendorf and hope that in the future it will again find a considerable interest among the scientists working in the field of two-phase and multiphase flow instrumentation.

Prof. Frank-Peter Weiß
Forschungszentrum Rossendorf
Institute of Safety Research
Director

Prof. Rainer Hampel
HTWS Zittau/Görlitz (FH)
Institute of Process Technology,
Process Automation and Measuring
Techniques (IPM)
Director

4th Workshop on Measurement Technique for
Stationary and Transient Two-Phase Flows
Rossendorf, Germany, November 16-17, 2000

ULTRASONIC DOPPLER METHOD FOR BUBBLY FLOW MEASUREMENT

Masanori Aritomi, Hiroshige Kikura and Yumiko Suzuki

Research Laboratory for Nuclear Reactors, Tokyo Institute of Technology
2-12-1 Ohokayama, Meguro-ku, Tokyo 152-8550, Japan

ABSTRACT

The Ultrasonic Velocity Profile technique has been developed to measure multi-dimensional flow characteristics in bubbly flows with the void fraction smaller than 7%. This measurement system can measure instantaneous mixture velocity profiles along a measuring line. By analyzing statistically the measured data, velocity profiles of both phases, the void fraction profile, turbulence intensity of the liquid phase in a channel and flow structure of the liquid phase surrounding a bubble can be obtained. The flow structure around bubbles was proposed to be divided into three regions: viscous sublayer, buffer region, and turbulence region.

Keywords: Bubbly flow measurement, Velocity profiles, Ultrasonic Doppler measurement

1. INTRODUCTION

The flow structure surrounding bubbles is one of the interesting topics in the field of two-phase bubbly flow. A great number of experimental studies have been carried out to understand the fundamental mechanism of two-phase flows. The quick closing valves is one of the most simple and early-developed methods to measure the average void fraction of steady and uniform two-phase flow [1]. To measure local void fraction, probe techniques and radiation techniques have been used for a long time [2] and [3]. In recent years, a laser Doppler anemometer has been applied to the bubbly flow measurement as a strong device to investigate the flow structure in detail, such as local void fraction profile, liquid velocity and its fluctuation [4] and [5]. Flow visualization techniques have also been used commonly in order to understand bubble deformation and coalescence phenomena [6] and [7]. These methods have made a great contribution in clarifying the flow structure of the bubbly two-phase flow. However, there still does not exist a measurement technique which can easily measure the velocity profile around a gas-liquid interface, even though it is necessary to clarify the flow structure around the bubble surface in order to understand the microscopic mechanism of bubbly flows.

The authors attempt to apply UVP method to measure multi-dimensional flow characteristics in bubbly flows with void fraction less than 7%. The ultrasonic pulse is reflected on both micro-particles in liquid phase and gas-liquid interfaces, so that instantaneous mixture velocity profile along the measuring line can be measured. By

treating statistically the measured instantaneous mixture velocity profile, a probability density function profile of the mixture velocities can be obtained. From the results, velocity profiles of both phases, the void fraction profile, turbulence intensity of the liquid phase can be obtained in a channel. Since velocity information of both phases is included in the measured instantaneous mixture velocity profile, the phase discrimination of the measured instantaneous mixture velocity profile is one of the important processes in order to study the flow structure of liquid phase surrounding bubbles. From the measured instantaneous velocity profiles, the position of the bubble surface was decided and the data was rearranged according to the distance from the bubble surface.

In this paper, a measurement system using the UVP monitor is proposed and its measurement principle is explained first. Furthermore, the proposed measurement system is applied to bubbly flows in a vertical rectangular channel to verify its capability. Finally, improvement of the proposed measurement system is discussed as our future work.

2. MEASUREMENT METHOD OF ULTRASONIC VELOCITY PROFILE MONITOR

2.1 Experimental Setup

Figure 1 shows the schematic diagram of the experimental apparatus. It consisted of a water circulation system, an air supply system, a test section which is a rectangular channel made of Plexiglas and a measurement system of Ultrasonic Velocity Profile (UVP) monitor. Working fluids were air and tap water. Micro particles of nylon powder were mixed in the water as reflector of ultrasonic pulses. The average diameter of the powder was about 40 μm, and the specific density was 1.02.

In the measurement of counter-current flows, water was fed from the upper tank into the test section. Water flow rate was controlled by a needle valve and it was measured by an orifice flowmeter, both of which were located at the bottom part of the apparatus. Air was injected into water through five needles (inner diameter: 0.17 mm) at the air-water mixing section, which were also located at the lower end of the test section. The air flow rate was regulated by a float flow meter and an air control valve. In the measurement of co-current flows, water flowed upward into the test section from the lower entrance of the test section. Air was injected from the same air-injection needles as those of the counter-current flows. During an experiment, water temperature was kept between 19 and 21 degrees using a subcooling system. Also in parallel to the measurement by the UVP, the pressure drop was measured between pressure taps installed on the sidewall to get average void fraction. All experiments were carried out under the atmospheric pressure.

Figure 2 shows the test section located between the upper tank and the air-water mixer. The test section was a vertical rectangular channel made of Plexiglas measuring 10 mm × 100 mm × 1700 mm. An ultrasonic transducer was set on the outer surface with a contact angle of 45 degrees toward the liquid main flow direction. Gap between the transducer and the wall was filled with ultrasonic jelly to

prevent the reflection of ultrasonic pulses on the wall. Under each experimental condition, measurement was carried out and 9,216 velocity profiles were obtained along the measuring line. The experimental conditions are tabulated in Table 1. Also, the UVP configurations used in this study are summarized in Table 2.

An outline of video camera equipment is shown in Fig.3. It consists of a digital video camera, alight source and a translucent sheet to unify the luminance brightness. The speed, diaphragm and gain of the video camera can be manually regulated and a speed of 60 flames per second can be obtained. After videotaping, the video digital data were recorded in a personal computer through an image converter. The picture elements were 720×480 dots, the color was monotone, and the brightness resolution was 1/256. Figure 4 is an example of the photos of the counter-current flow. In Fig. 5, the relationship between the average void fraction in the channel and average bubble diameter is shown.

2.2 Measurement Principle

The working principle of the UVP is to use the information contained in the echo of ultrasonic pulses reflected by micro particles suspended in the fluid. Since the detailed information of its measurement principle has been reported by Takeda [8], [9], only a simple explanation is made here.

The position information, x, is obtained from the time lapsed, τ, from the emission to the reception of the echo:

$$x = \frac{c\tau}{2} \tag{1}$$

where c is a speed of sound in the fluid. The instantaneous local velocity, $u_{UVP}(x)$, is a component along the ultrasonic beam direction and is derived from the instantaneous Doppler shift frequency, f_D, in the echo:

$$u_{UVP} = \frac{cf_D}{2f} \tag{2}$$

where f is the basic ultrasonic frequency. The velocity resolution is given by

$$\delta u_{UVP} = \frac{u_{UVPmax}}{128} \tag{3}$$

The measured velocity profile is expressed by a location number, i, a profile number, j, and a velocity value, k.

$$k = u[i, j] \tag{4}$$

The position, $y(i)$, is determined from the wall location, i_1 and i_2 as

$$y(i) = \frac{i - i_1}{i_2 - i_1} W \tag{5}$$

where W is the width of the channel, 10mm.

The measured velocity, which is a component along the ultrasonic beam direction, u_{UVP}, is determined by

$$u_{UVP} = k\Delta u \tag{6}$$

where Δu is the conversion factor from Doppler unit to velocity. The velocity in the flow direction, u, is then given by

$$u = \frac{u_{UVP}}{\cos\theta} \tag{7}$$

where θ is the angle of the transducer with respect to the flow direction. The measurement error of velocity is estimated as ±5%.

2.3 Data Processing Method

Since the speed of sound of longitudinal waves is the most fundamental parameter for this method, it is incorrect to treat a two-phase medium as a homogeneous single phase medium because sound waves experience multiple reflection at bubbles. Since the ultrasonic pulse diameter using in this work is 5mm, which is larger than bubble diameter of about 3mm, the ultrasonic pulse and its reflection can potentially traverse straight on while creating a blind zone behind the bubble as shown in Fig.6. Typical patterns of instantaneous velocity profiles are shown in Fig.7 (a), (b) and (c): (a) is the case where there is no bubble in the measurement path, (b) is the case where a single bubble exists and (c) is the case where two bubbles exist. In case of Fig.7 (c), we cannot distinguish whether two bubbles exist in the measurement volume or if there are multiple reflection between bubbles as shown Fig.8 (a) and (b). Since a velocity profile like that shown in Fig.7(c) is rarely encountered under the present experimental conditions, it is omitted while data processing in this study. It is however, possible to obtain velocity profiles of the liquid phase, even at high void fraction, until a bubble approaches the transducer. The authors thus attempted to derive information from each individual profiles by analyzing their shapes.

Although the spatial resolution of the UVP measurement is not particularly fine because the ultrasonic beam diameter is 5mm, the nearly instantaneous water velocity profile near a bubble can be measured by the UVP measurement as shown in Figs. 7(b) and 7(c). If many velocity profiles are obtained and treated statistically, the flow characteristics near a bubble may be deduced.

2.3.1 Angle of the Ultrasonic Transducer

Since the velocity information is derived from the Doppler shift frequency, no data must exist at the wall. The diameter of the ultrasonic pulse beam is 5mm and the UVP transducer must be inclined with respect to the wall in order to measure velocities in the flow direction. Figure 9 (a), (b) and (c) show typical results of frequency of data existence in reference to the transducer angle at the wall. In single phase water flow, it can be seen from Fig. 9(c) that with the setting angle at 75ß, we have the most suitable angle in terms of the frequency of data existence. However, it is seen from Figs.9 (a) (b) and (c) that a transducer angle of 45ß is best in bubbly

flows to prevent multiple reflection. The ultrasonic pulse is perfectly reflected at the channel wall and can not be transmitted into the fluid. Therefore, a transducer angle of 45ß is adopted in this work.

2.3.2 Velocity and Void Fraction Profile in the Channel

The probability of data existence was examined along ultrasonic beam direction. It can be seen from Fig. 9(a) that the wall position is identical to the location where the probability of data existence is 50% in single phase liquid flow. The measurement error of the wall position is estimated as ±0.1mm and the measurement error of the location is estimated as ±0.6mm. Since the diameter of an ultrasonic pulse is 5mm, its measurement cross section is a circular disk in the main region of flow and the echo can be completely measured in the form of the circular cross section. On the other hand, the measurement cross section can not be circular near the wall region, so that the statistical average position of the measurement cross section is not the center of ultrasonic pulse. Assuming that the statistical average position of the measurement cross section divides the measuring cross section into two equal cross sections, the statistical average position is revised. Thus, the measuring cross sectional area less than 50% of the whole ultrasonic beam is omitted.

The probability of data existence, $P_1(y)$, is defined by

$$P_1(i) = \sum_{j=1}^{N} f_1(i,j) \Big/ N, \tag{8}$$

$$f_1(i,j) = 1 \quad \text{for } V[i,j] \neq 0,$$
$$= 0 \quad \text{for } V[i,j] = 0,$$

where N is the number of total profiles. A profile of the probability of data existence, $P_s(y)$, is obtained by converting the location number, i, into a real position, y.

Let us consider a velocity probability function:

$$P_2(i,k) = \sum_{J=1}^{N} f_2(i,j) \Big/ \sum_{J=1}^{N} f_1(i,j) \tag{9}$$

$$f_2(i,j) = 1 \quad \text{for } V[i,j] = k,$$
$$= 0 \quad \text{for } V[i,j] \neq k.$$

A probability density function, $P_u(y,u)$, is obtained by normalizing $P_2(i,j)$ and by converting the location number, i, into a real position.

A probability density function includes the velocity information. It is assumed that each probability density function of a given phase can be expressed by a normal distribution, as follows:

$$N[\bar{u},\sigma^2](u) = \frac{1}{\sqrt{2\pi\sigma^2}} exp\left[-\frac{(u-\bar{u})^2}{2\sigma^2}\right] \tag{10}$$

The probability density function of the mixture velocity is given by

$$P_v(y,u) = \varepsilon(y) N[\overline{u_G}(y), \sigma_G^2(y)](u) + (1-\varepsilon(y)) N[\overline{u_L}(y), \sigma_L^2(y)](u) \tag{11}$$

where σ_G and σ_L are average velocities and standard deviations of both phases respectively, and ε is the probability of bubble existence. These five variables, σ_G, σ_L and ε, are calculated numerically by the least-squares method.

Figure 10 compares a probability density function of mixture velocities calculated by the above-mentioned procedure with experimental results. In this figure, open circles indicate the results measured by the UVP and the line represents the calculated result.

Since the ultrasonic pulse is reflected at the interface as long as a bubble exists, the bubble velocity can always be detected as an interfacial velocity. On the other hand, the ultrasonic wave is not reflected in water where a micro-particle does not exist. As a result, the water velocity is not always measured in the profile. Therefore, it is necessary to revise the probability of bubble existence as follows:

$$\kappa(y) = P_s(y)\varepsilon(y) \tag{12}$$

where $\varepsilon(y)$ is called the probability of bubble data existence in this work.

The probability of bubble data existence means that a bubble exists in the path of the ultrasonic pulse when the pulse is emitted, and is related to the void fraction. The bubble size, its position and its configuration cannot be known directly from UVP measurements. Assuming that the bubble size and configuration are at random and that they are statistically uniform across the channel, the conversion factor, which relates the probability of bubble data existence to the void fraction, can be obtained. The following procedure was developed to establish the conversion factor.

The average volumetric flux of the bubble $\langle j_G \rangle$ is

$$\langle j_G \rangle = \frac{\int_A j_G dA}{A} = \frac{\int_A \alpha u_G dA}{A} \tag{13}$$

where j_G is the local volumetric flux of the bubble and A is the cross sectional area of the channel. Assuming that the local void fraction is proportional to the local probability of bubble data existence and that the proportionality constant (the conversion factor), k, is uniform in the channel since it is dependent on bubble size and configuration, the following equation can be obtained:

$$\langle j_G \rangle = k \frac{\int_A \kappa u_G dA}{A} \tag{14}$$

The average void fraction is expressed by

$$\langle \alpha \rangle = \frac{k \int_A \kappa dA}{A} \tag{15}$$

If the air flow rate is known, we can transform Eq.(14) to

$$k = \frac{\langle j_G \rangle A}{\int_A \kappa u_G dA} = \frac{\langle j_G \rangle}{\langle \kappa u_G \rangle} \tag{16}$$

Then, the local void fraction, $\alpha(y)$, is simply given by

$$\alpha(y) = k\kappa(y). \tag{17}$$

The average void fraction, $<\alpha>$, is also represented by

$$\langle\alpha\rangle = k\langle\kappa\rangle. \tag{18}$$

2.3.3 Velocity Profile around Bubbles

When the UVP is used for the measurement of bubbly flow, ultrasonic pulses are reflected either on a gas-liquid interface or micro particles suspended in the liquid, and then the velocity profiles in the channel is obtained. Therefore a measured velocity profile contains not only liquid phase velocity information but also the bubble-rising velocity information, which is obtained from pulses reflected on the bubble's surface. In the measuring of bubbly flow, an instantaneous velocity profile has a typical peak if a bubble crosses the measuring line. The maximum velocity in the instantaneous velocity profile including bubble is much larger than the one excluding bubbles. By introducing an appropriate threshold velocity, the recorded instantaneous velocity profile can be divided into two groups, that is, profiles either including bubbles or not.

Figure 11 shows a flow chart of data processing. The first step in the determination of the threshold velocity is to obtain the probability density function of all the measured 27,648 instantaneous velocities at each measuring position. This is called "PDF_{all}" (Fig. 12(a)). Velocity information of both phases is mixed up in this PDF_{all}. When the void fraction is very low, PDF_{all} have usually two peaks; one represents the liquid velocity and the other stands for the velocity concerning the gas-rising velocity. However in some experimental conditions, only one peak is seen, which corresponds to the liquid velocity. Since the PDF_{all} also contains liquid velocity accelerated by the gas phase, the PDF_{all} monotonously decreases from the peak of liquid phase toward the velocity of gas phase. The mixture of these liquid velocities makes the phase discrimination difficult.

As the second step, liquid main flow velocity is separated from PDF_{all}. The peak velocity of the liquid phase in the PDF_{all} is chosen as the representative velocity of the liquid phase, u_{Lm}. By assuming that the ideal shape of PDF for the liquid main flow velocity is symmetrical because of the symmetric nature of the random error, PDF of the liquid phase can be estimated by turning up the left-hand side of the PDF for the liquid phase at the u_{Lm}. From the obtained PDF, called the ideal PDF for the liquid main flow, standard deviation σ_L is calculated. By taking into account the fluctuation of liquid velocity, the threshold velocity for separation of the liquid main flow, u_{temp}, is obtained as $u_{temp} = u_{Lm} + 2\sigma_L$

At this time another PDF, PDF_{max}, is defined representing the gas velocity (Fig. 12(b)). PDF_{max} at each measuring position is obtained by collecting only the largest velocity in each instantaneous velocity profile. Most of the velocity information included in PDF_{max} is either the bubble's velocity or the maximum velocity of the liquid phase in the case not including bubbles. Therefore if the liquid phase velocity

is separated from PDF_{max}, PDF corresponding to the bubble's velocity can be obtained. For the separation of liquid velocities, u_{temp} at the same measuring point is used and data smaller than u_{temp} is eliminated from the PDF_{max}.

From the remaining PDF, the average velocity u_{Gm} and the standard deviation σ_G is calculated. By using these values, finally the threshold velocity for the phase separation u_{thresh} is obtained as $u_{thresh} = u_{Gm} - 2\sigma_G$ (Fig. 12(b)). The calculation of the u_{thresh} is made at each measuring point in the channel according to the above procedure and the threshold velocity profile $u_{thresh}(x)$ is obtained as a result. Using this threshold velocity profile, phase discrimination is made for each instantaneous velocity profile.

The measured instantaneous velocity profile including only velocities lower than u_{thresh} means the liquid velocity one affected by bubble rising motion and is classified into Group A. By averaging velocities in Group A, the time-averaged velocity profile of liquid main flow can be obtained. On the other hand, the measured instantaneous velocity profile whose maximum velocity higher than u_{thresh} has bubble motion information and is classified into Group B. In Group B, the relative coordinate is adopted and its origin is set on the bubble surface for the selected instantaneous velocity profiles. In order to examine the flow structure surrounding a bubble, the selected velocity profiles are statistically treated by converting their data as a function of the distance from a bubble surface, and thus the probability density function of liquid velocity fluctuation is calculated at each distance from a bubble surface.

After splitting all instantaneous velocity profiles into two groups, probability density functions of instantaneous velocities are calculated at every measuring point in the channel. From the obtained shape of the probability density function, statistical moments were calculated for the liquid phase velocity as follows:

$$M = \int_{-\infty}^{\infty} (u - c)^n P_u(x) du \tag{19}$$

where u means a measured velocity, $P_u(x)$ a probability density and

$c = 0$ for the first order moment,
$= U$ for higher order moments.

where U is the first order moment that means the average velocity. The second order moment means the standard deviation of velocity fluctuation, σ_2, called variance, the third dimensionless one, M_3/σ_3, is called the skewness and the fourth dimensionless one, M_4/σ_4, is the kurtosis.

3. EXPERIMENTAL RESULTS

3.1 Velocity Profile in the Channel

The developed measurement system was applied to bubbly countercurrent flows in a vertical rectangular channel. Figure 13(a) and (b) shows typical measurements of velocity profiles in both phases, u_G and u_L, and a probability profile of bubble data

existence, $\kappa(y)$. The velocities of both phases are not zero at the wall because the ultrasonic pulse is emitted at an angle with respect to the channel wall and its beam diameter is 5mm, the combined effect of which induces an error in the velocity measurements near the wall. However, this uncertainty is not a feature of two-phase flow measurement, but also appears for the velocity profiles measured in a single-phase flow by the UVP.

3.2 Void Fraction Profile

Let us consider another procedure in order to estimate the conversion factor between the probability of bubble data existence and the void fraction using the average void fraction measured by the image data processing unit. Assuming that an entire bubble exists in the path of the ultrasound beam when the pulse is emitted, the measurement volume, V_1, is expressed by

$$V_1 = \frac{1}{4}\pi D_u^2 L \tag{20}$$

where D_U is the ultrasound pulse diameter and L is the UVP measurement length. The bubble volume is

$$V_b = \frac{1}{6}\pi D_b^3 \tag{21}$$

where D_b is the average bubble diameter. The conversion factor, k_1, can be given by

$$k_1 = \frac{V_b}{V_1} = \frac{2D_b^3}{3D_u^2 L} \tag{22}$$

If a vertical portion of the bubble's surface encounters the path of the pulse, the ultrasonic transducer may receive the reflection wave of this pulse. Hence, we consider the case where a half of a bubble exists in the pulse path. In this case, the UVP measurement volume, V_2, can be expressed by

$$V_2 = \frac{1}{4}\pi(D_u + D_b)^2 L \tag{23}$$

The conversion factor k_2 is

$$k_2 = \frac{V_b}{V_2} = \frac{2D_b^3}{3(D_u + D_b)^2 L} \tag{24}$$

The conversion factors obtained from experiments are shown in Fig.14 in reference to average bubble diameters. k_1 and k_2 are shown in the figure. It is seen from the figure that k_v, is located in the region of $k_2 < k_v < k_1$. Although the conversion factor cannot be evaluated exactly because of a wide range between k_1 and k_2, it is apparent that the factor depends on the average bubble diameter. Since the bubble is not spherical, the factor may also be influenced by the bubble shape. However, its empirical correlation can be established by analyzing numerous data. Moreover, it seems that the conversion factor can be established from the UVP data if each data profile is analyzed in detail and for instance, pattern recognition of the echo signal is established. These are topics of future studies.

The conversion factor can also be calculated by the average void fraction obtained from the hydrostatic head measurement and by the average probability of bubble data existence. Figure 15 shows a typical void fraction profile converted from the probability profile of bubble data existence in this way. As mentioned above, the average void fraction in the flow cross section is estimated as ±5%. Regarding the local void fraction, although the error introduced by the assuming uniformity in the conversion factor between the local void fraction and the local probability of bubble data existence in the cross section of the flow cannot be evaluated exactly, the error in the local void fraction may be estimated as ±10%.

3.3 Turbulent Intensity Profile

In general, turbulence intensity in a bubbly flow is larger than that in liquid single phase flow because bubbles agitate the flow. In this work, turbulence intensity is defined in terms of the standard deviation of water velocity fluctuation in the continuous phase, σ_L. The standard deviation profile in the channel can be calculated from the equation of the probability density function of mixture velocity defined by Eq.(11). Typical results from single-phase water flow and bubbly countercurrent flow are shown in Fig.16. Since the local velocities were not measured at a point but over an area because of the size of the ultrasonic beam diameter (5mm), the absolute value of the standard deviation in the water phase is not significant. Hence, the standard deviation ratio of a bubbly countercurrent flow to a single phase water flow is selected as the two-phase multiplier of turbulence intensity, $\sigma_{LTPF}/\sigma_{LSPF}$.

3.4 Velocity Profile around Bubbles

Figure 17 shows typical profiles of the probability density function of relative velocity in reference to the distance from a bubble surface. In the figure, x=0 means a bubble surface and x=1 is the position 0.74mm away from the bubble surface.

The probability density function near a bubble surface (x=0-1) has a one peak which means the rising velocity of the bubble motion. In the region of x=2-10, two peaks appear, which correspond to the bubble surface velocity and main flow. The peak corresponding to the bubble surface velocity becomes lower and the other peak does larger with going way from the bubble. In the region far from the bubble (x=11-14), the probability density function has one peak again which is the main flow.

Figure 18 (a) shows a typical a velocity profile normalized by the average bubble surface and liquid main velocities. Moreover, profiles of typical valiance, skewness and kurtosis are shown in Fig.18 (b), (c) and (d). It can be seen from different gradients shown in these figures that the liquid flow structure can be classified into three regions; (1) viscous sublayer region near a bubble where the liquid flow is greatly influenced only by the bubble motion, (2) turbulence region far from a bubble where it is not affected by the bubble motion and (3) buffer region located between viscous sublayer and turbulence region where it is influenced by the bubble motion and the main flow.

Some velocity profiles of Group B have the second peak between the position the maximum velocity and the channel wall as shown in Fig.19. The second peak velocity means the effect of a bubble flowing near the measurement volume. For the purpose to investigate the effect of another bubble motion on the liquid flow structure surrounding bubbles, the measured instantaneous velocity profiles in Group B are classified into two groups: the profiles having two peaks (Group B1) and those having only one peak (Group B2). Figure 20 (a) shows velocity fields surrounding bubbles which belongs to Group B1 and is affected by the wake of another bubble. In contrast with this, velocity fields surrounding bubbles in Group B2, which are not influenced by the wake of another bubble, are shown in Fig.20 (b).

4. FUTURE WORKS

The proposed measurement system has never developed perfectly and some improvements remain as our future works. Void fraction profile cannot be measured directly and its measurement accuracy has never exactly understood. In addition, the conversion factor, k, cannot be evaluated analytically. Hence, it will be attempted to apply the electrode-mesh tomography method [10] together with the UVP monitor in order to measure void fraction profiles and clarify the measurement accuracy of the UVP monitor for void fraction profiles.

Since the ultrasonic pulse diameter of 5mm is too large to measure liquid flow structure surrounding bubbles as compared with the bubble diameter of 2 to 5mm, the liquid flow structure cannot be quantitatively clarified from the measured data. It will be, therefore, attempted that UVP transducer having the narrower measurement volume should be developed and be applied to measure the liquid flow structure surrounding bubbles.

5. CONCLUSIONS

A measurement system incorporating an UVP monitor has been developed and proposed for use in measuring multi-dimensional bubbly flow characteristics. The system has been applied to bubbly counter-current and co-current flows with void fraction less than 7% in a vertical rectangular channel to assess its capability.

(1) The proposed system can measure instantaneous mixture velocity profiles in the channel.
(2) By treating statistically the measured instantaneous mixture velocity profiles, the velocity profiles of both phases, the void fraction profile and turbulence intensity of the liquid phase in the channel can be obtained.
(3) The phase discrimination method of the measured instantaneous mixture velocity profile was proposed using the probability density function of the mixed velocities. The position of the bubble surface was decided and the data was rearranged according to the distance from the bubble surface. From the results, it can be seen that the liquid velocity field surrounding bubbles can be classified into the following three region; viscous sublayer, buffer region and turbulence region.

(4) In laminar sublayer, the liquid velocity profile has a large gradient, and is greatly affected by the bubble motion but hardly affected by the liquid main flow.
(5) The buffer region plays a role as a transition zone between the laminar sublayer and the main flow region. The motion of both phases influences the flow structure in this region.
(6) The main flow region is far away from bubbles, so that bubble motion does not affect the continuous liquid phase.

REFERENCE

[1] Liu, T.J., Int. Journal of Multiphase Flow, 219-1 (1993), 99.
[2] Serizawa, A., Kataoka, I., and Michiyoshi, I., Int. Journal of Multiphase Flow, 2 (1975), 235.
[3] Herringe, R.A., and Davis, M.R., Journal of Fluid Mechanics, 73 (1976), 97.
[4] Martin, W.W. et al., Int. Journal of Multiphase Flow, 7 (1981) 439.
[5] Monji, H., and Matsui, G., Two-Phase Flow Modelling and Experimentation 1995, (1995), 367.
[6] Katz, J., and Meneveau, C., Int. Journal of Multiphase Flow, 22-2 (1996), 239.
[7] Tokuhiro, A., et al., Int. Journal of Multiphase Flow, 24 (1998), 1383.
[8] Takeda, Y., Development of Ultrasound Velocity Profile Monitor, Nucl. Engrg. Des., 126 (1990) 277.
[9] Takeda, Y., Velocity Profile Measurement by Ultrasonic Doppler Method, Experimental Thermal and Fluid Science, 10 (1995) 444.
[10] Richter, S. and Aritomi, M., A New Electrode-Mesh Tomograph for Advanced Studies on Bubbly Flow Characteristics, Rossendorf (2000.11) to be published.

Table 1 Experimental condition

System pressure	Atmospheric pressure
Water superficial velocity (co-current flow)	0.12 - 0.18 (m/s)
Water superficial velocity (counter-current flow)	-0.06 - -0.12 (m/s)
Air superficial velocity (co-current flow)	0.00235 - 0.00384 (m/s)
Air superficial velocity (counter-current flow)	0.00195 - 0.00418 (m/s)

Table 2 Specification of the UVP (X-1)

Basic ultrasonic frequency	4 (MHz)
Maximum measurable depth	91- 758 (mm)
Velocity resolution	5.6 - 0.75 (mm/s)
Time resolution	16.4 - 131 (msec)
Spatial resolution in water	0.74 (mm)
Measurement points	128
Number of profiles	1024×9

1. Overflow tank
2. Pressure tap
3. Test section
4. Pressure sensor
5. Oscilloscope
6. UVP monitor
7. US transducer
8. Compressor
9. Storage tank
10. Air water mixer
11. Flowmeter
12. Orifice flowmeter
13. PC
14. Heat exchanger
15. Centrifugal Pump

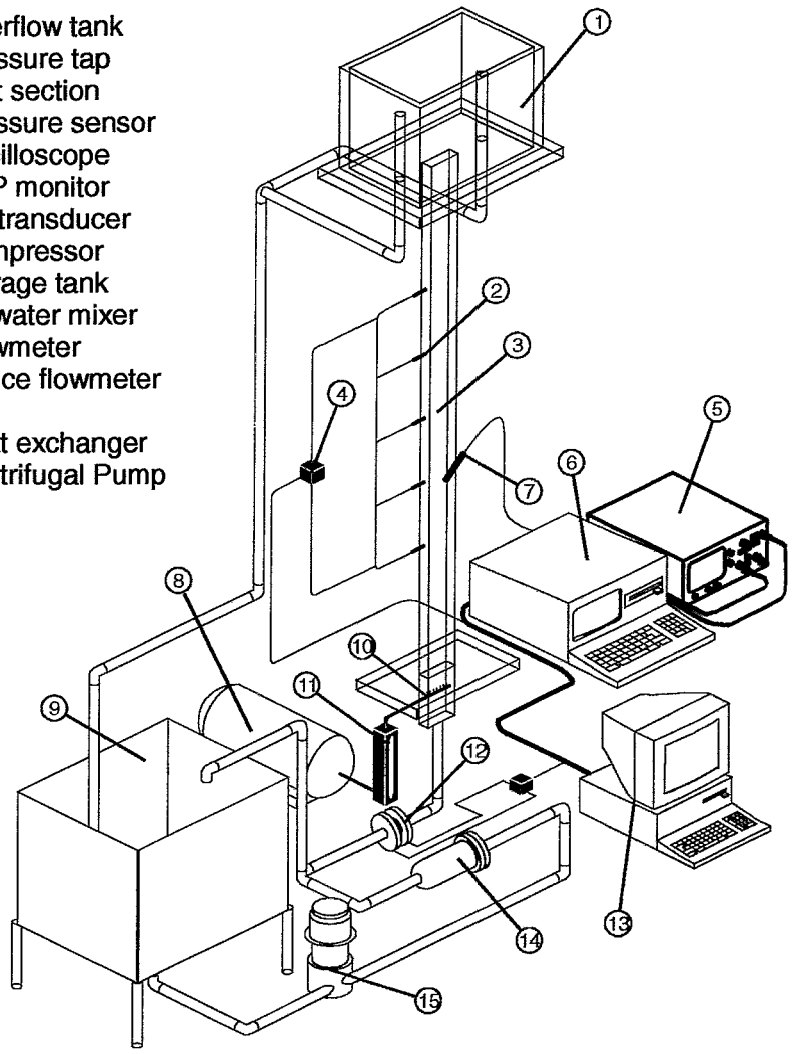

Fig.1 Experimental apparatus

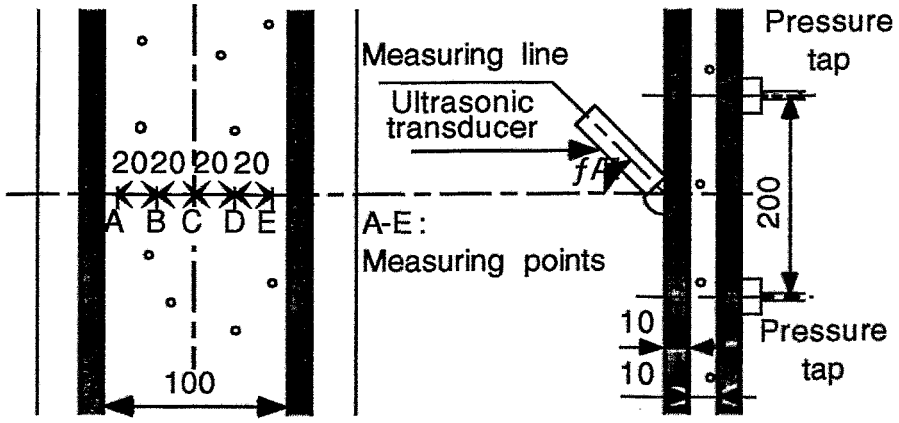

Fig.2 Test section

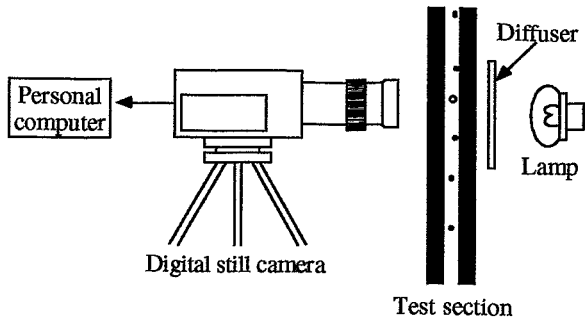

Fig.3 An outline of video camera equipment

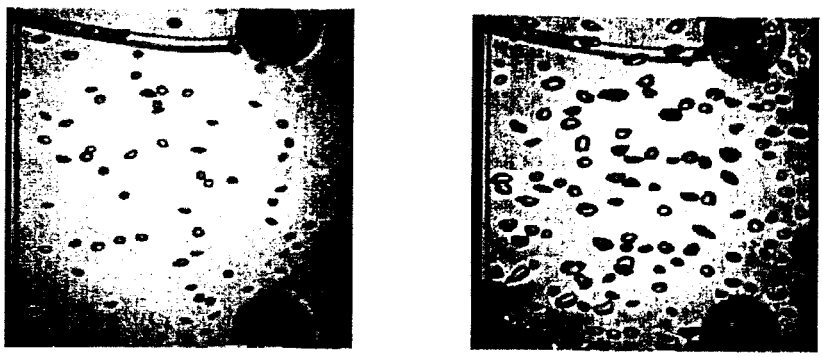

(a) J_L=-0.06m/s,J_G=0.00195m/s, α=1.1%

(b) J_L=-0.12m/s,J_G=0.00418m/s α=5.7%

Fig.4 Typical pictures taken with a video camera

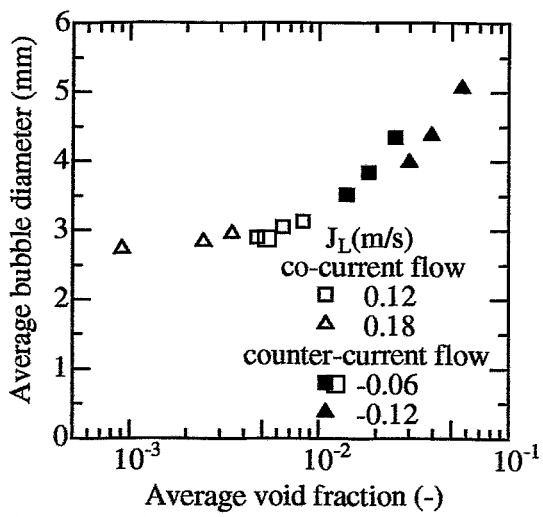

Fig.5 Void fraction and average bubble diameter

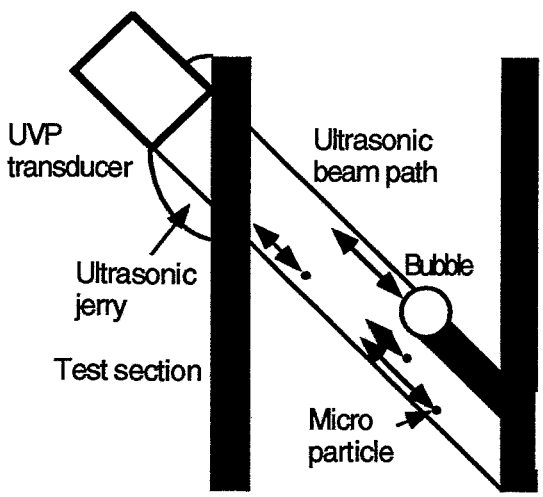

Fig. 6 Blind zone behind bubbles

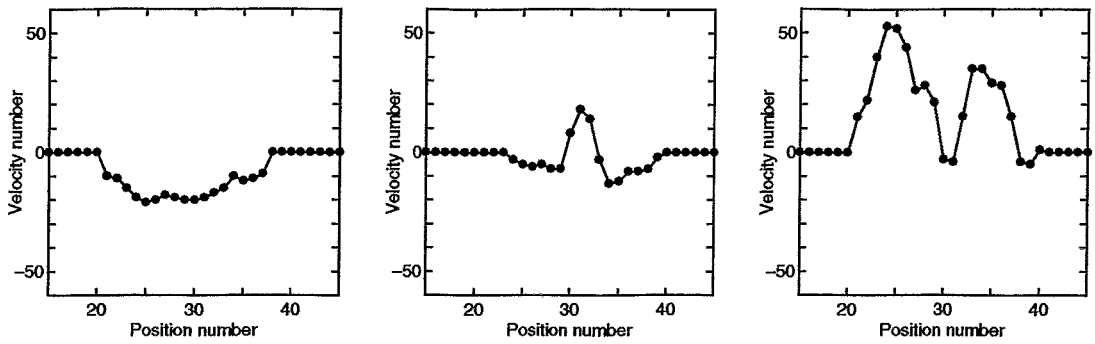

(a) Without bubbles (b) With single bubble (c) Multiple reflection

Fig.7 Typical patterns of velocity profiles

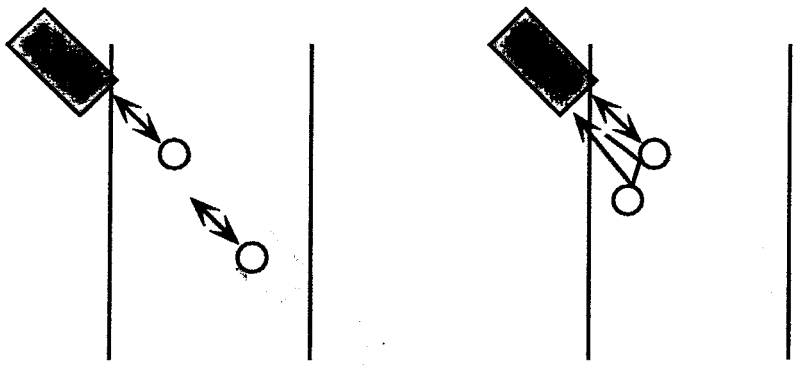

(a) Without multiple-reflection (b) With multiple-reflection

Fig.8 Multiple reflection pattern

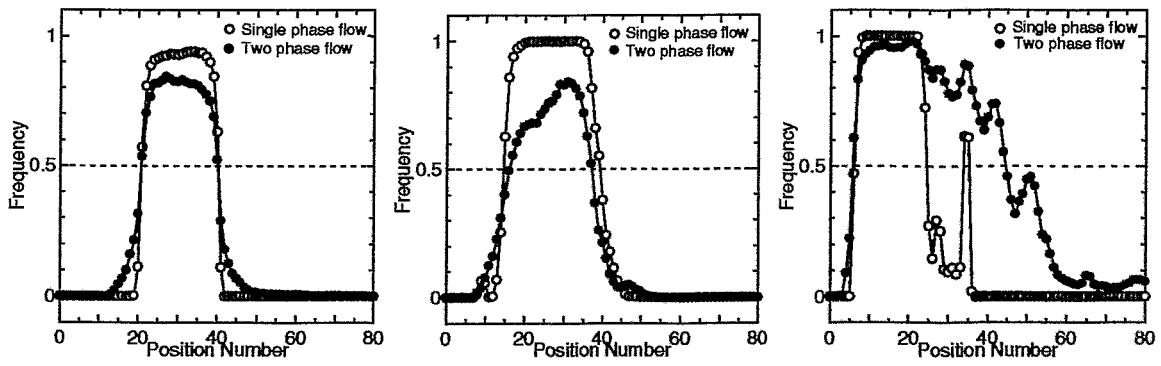

(a) θ= 45ß (b) θ=60ß (c) θ=75ß

Fig.9 Definition of the wall position

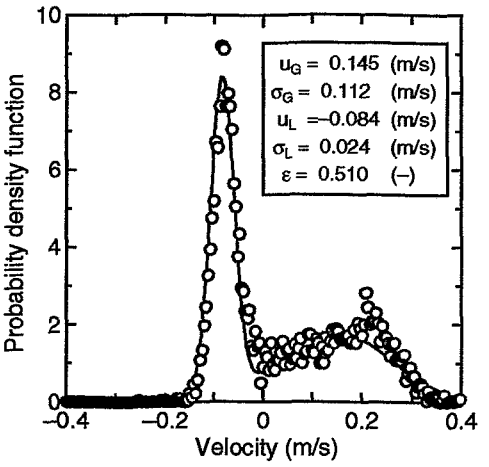

Fig.10 Comparison of the analytical probability density function with the measured one

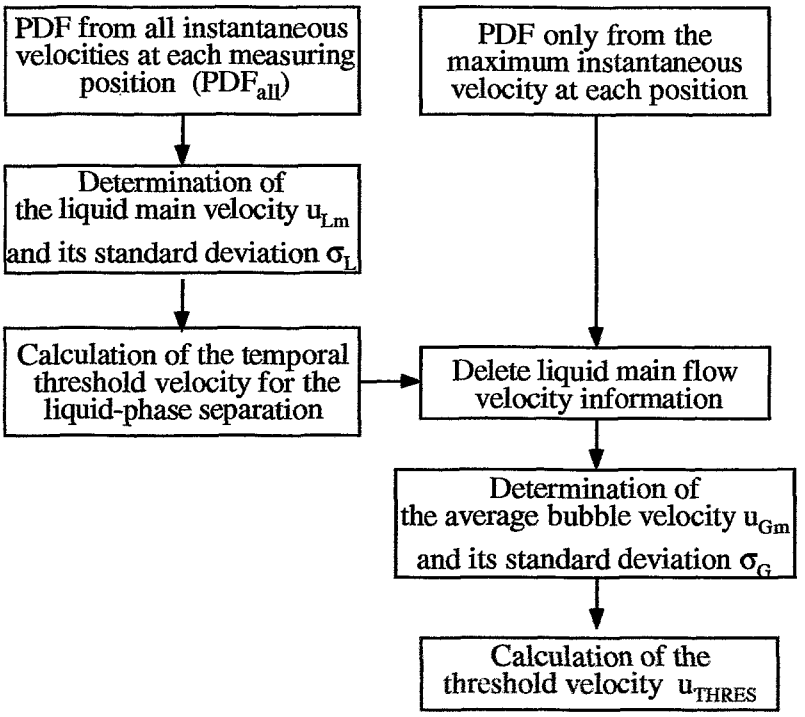

Fig.11 A flow chart of data processing

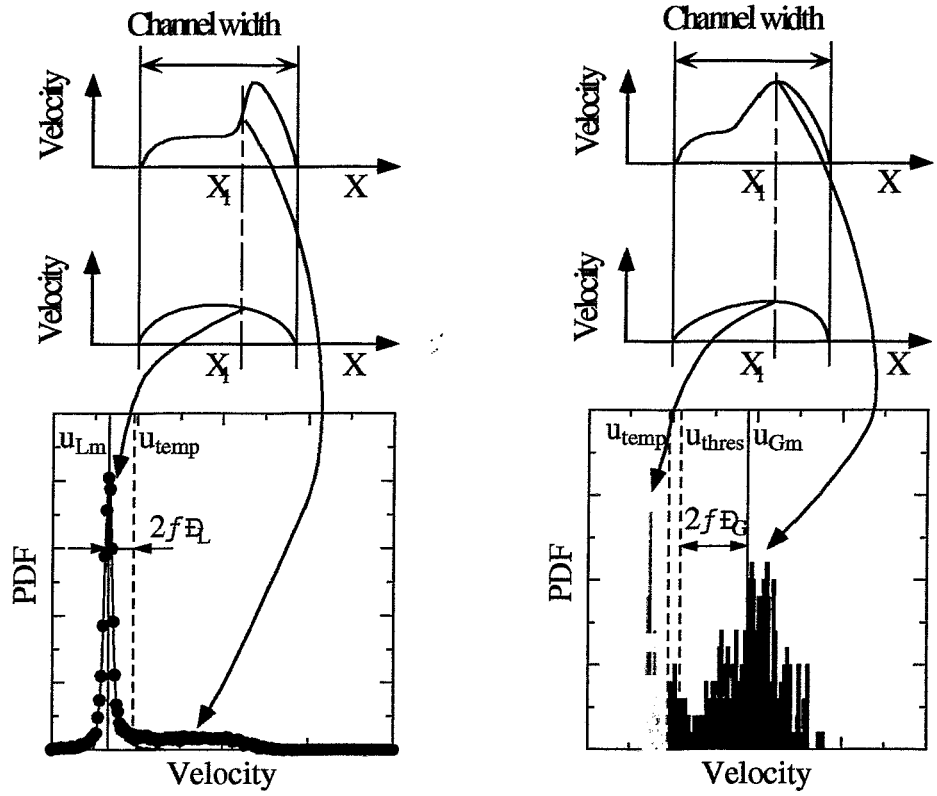

(a)Obtain PDF using all velocity at each measuring point

(b) Obtain PDF using maximum velocity in the channel

Fig. 12 Data processing of phase discrimination

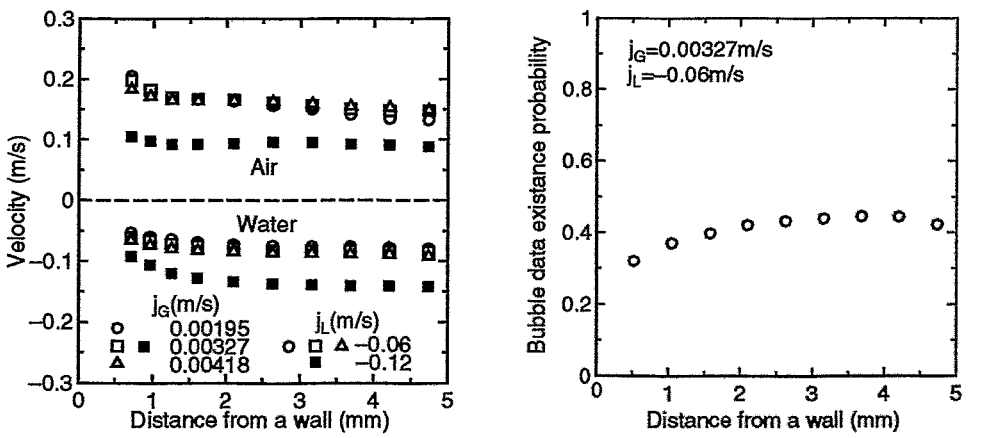

(a) Velocities of both phases

(b) Bubble data existence probability

Fig.13 Typical measured profiles of mixture velocities and bubble data existence probability

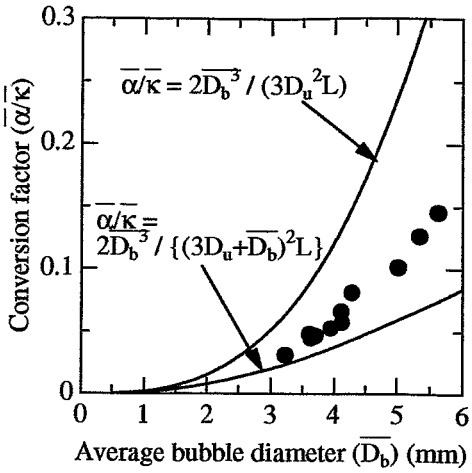

Fig.14 The conversion factor from bubble data existence probability to void fraction

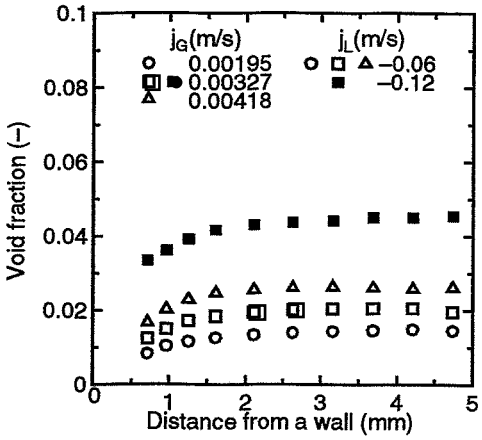

Fig.15 Typical profiles of void fraction

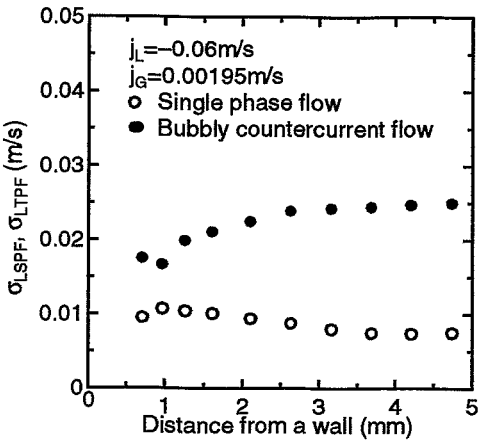

Fig.16 Typical standard deviation profiles of velocity fluctuation

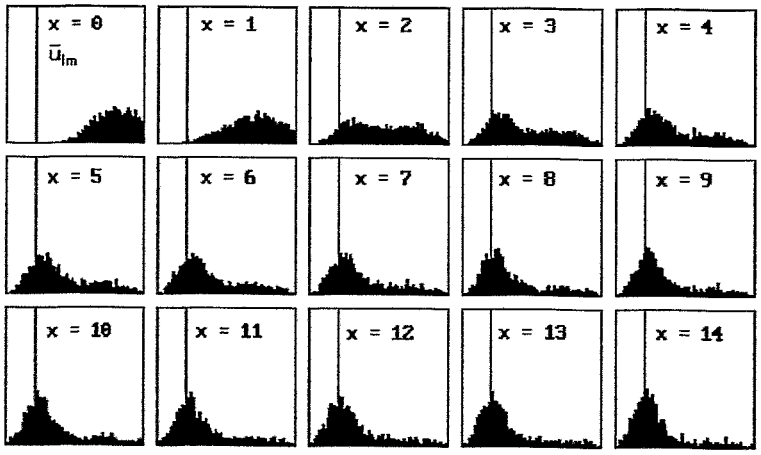

Fig.17 Typical profiles of the probability density function around a bubble

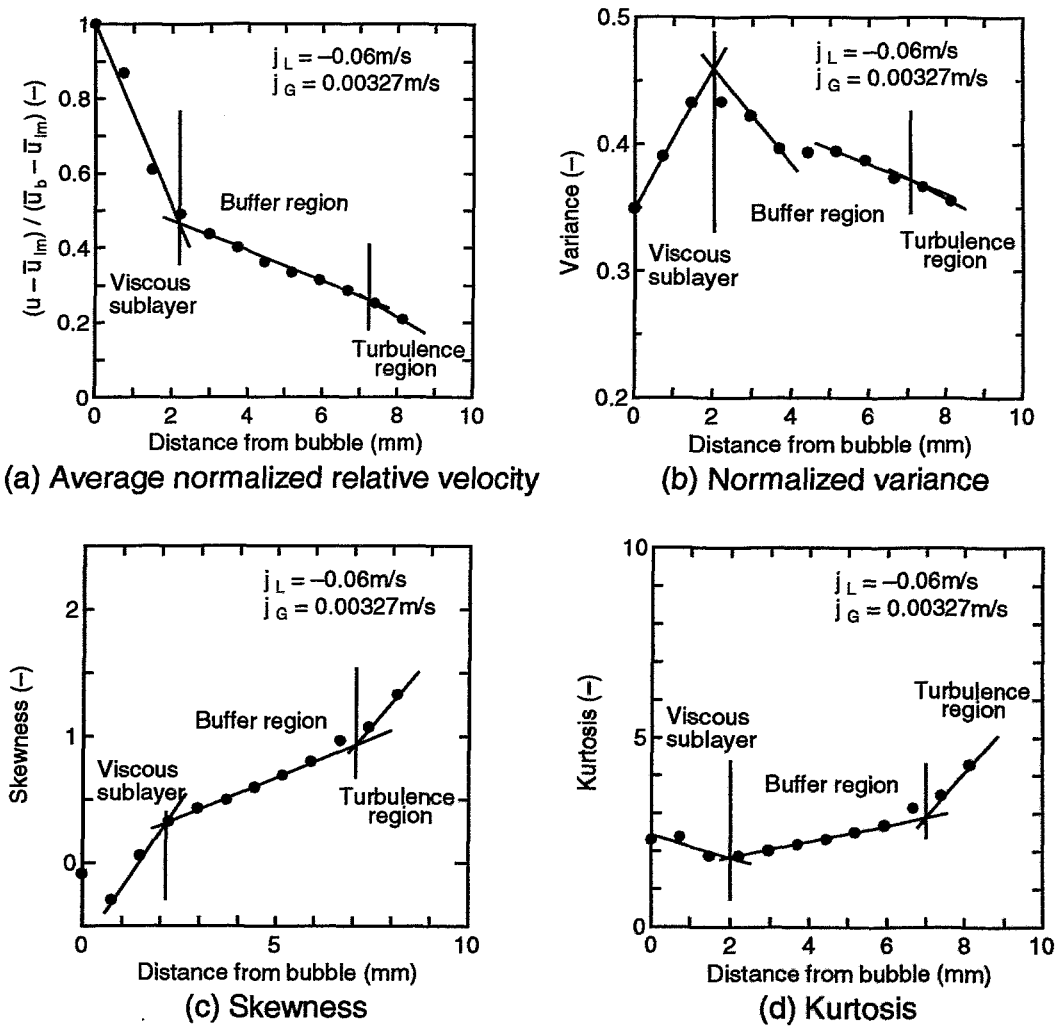

Fig.18 Typical profiles of statistical moments of liquid velocity surrounding bubbles

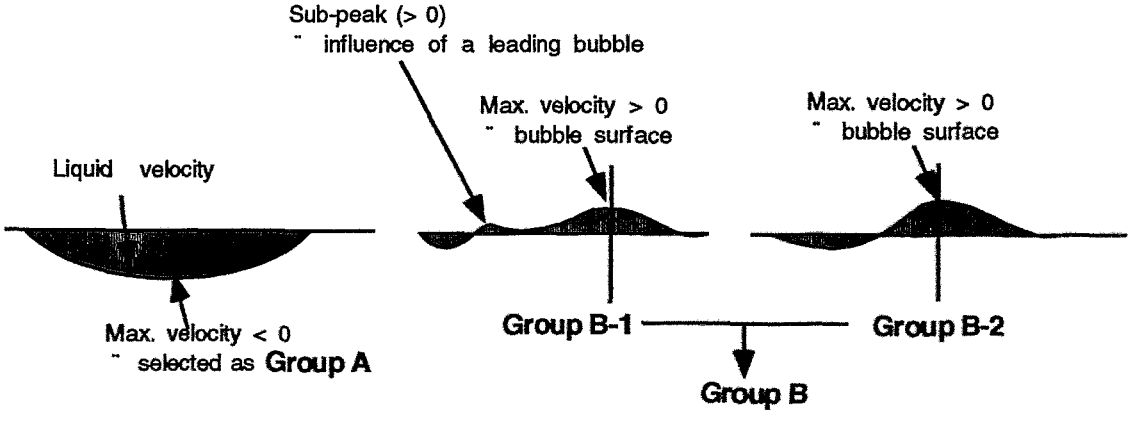

Fig.19 Typical data patterns and their classification

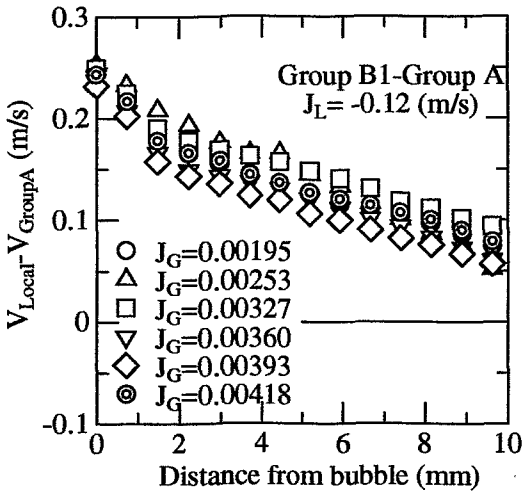

(a)With effect of another bubble wake (Group B1)

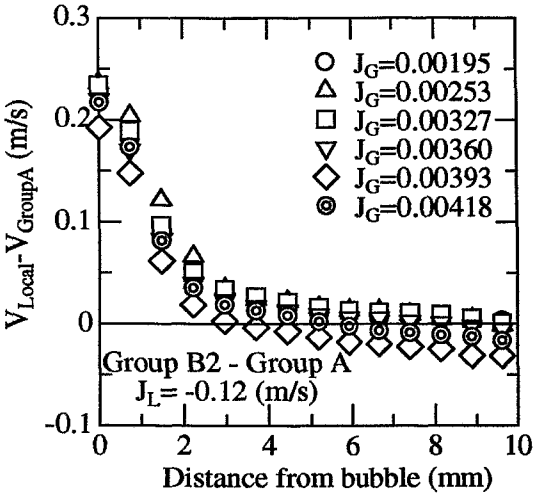

(b) Without effect of another bubble wake (Group B2)

Fig.20 Typical average normalized relative velocity surrounding bubbles

AN ULTRASONIC MESH SENSOR FOR TWO-PHASE FLOW VISUALISATION

V. V. Kontelev, V. I. Melnikov

Technical State University of Nishny Novgorod, Russian Federation

1. Introduction

This paper presents an ultrasonic mesh sensor for two-phase flow visualisation. Working principle of the ultrasonic mesh sensor is described. Special emphasis is given to the sensor design and operating conditions of the device. The results of experimental test of the ultrasound system are shown. Advantages and disadvantages of the ultrasonic device are outlined.

2. Working principle of ultrasonic mesh sensor

Working principle of ultrasonic mesh sensor is based on the measurement of the acoustic conductivity of the two-phase mixture in local points, which are equally distributed over the cross section of the flow [1,2]. The simplified scheme of the ultrasonic mesh sensor is shown in Fig. 1. The sensor consists of two groups of ultrasound wave-guides. The wave-guides of the first group are used to irradiate acoustic waves into the two-phase mixture. The wave-guides of the second group are used to receive the acoustic waves transmitted through the measuring fluid in the control volumes. If there is liquid (e.g. water) in the measuring volume, the attenuation of the ultrasound propagating through the measuring volume, is insignificant, and the ultrasonic waves reach the receiver wave-guides. After transformation into the electric signals by a piezocrystal, the amplitude of the received waves is registered by the electronic block. If the control volume is filled with gas or vapour the ultrasound is not irradiated, and the signal does not appear at the receiver wave-guides. Schematic view of the ultrasonic wave-guide system is shown in Fig. 2.

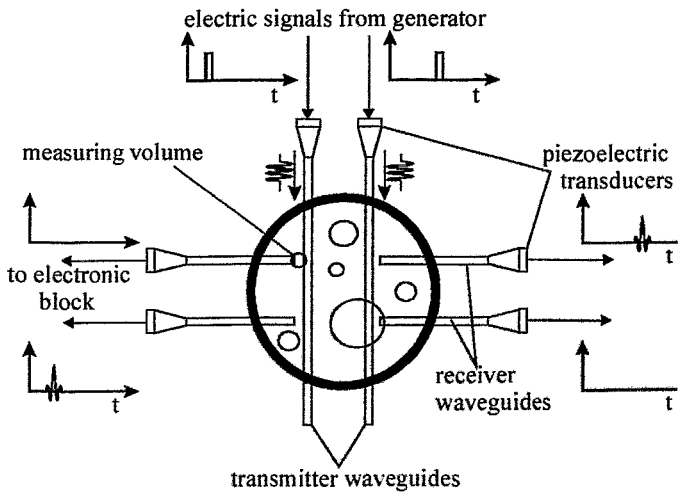

Fig. 1. Simplified scheme of an ultrasonic mesh sensor with six wave-guides

The ultrasonic mesh sensor is connected to an electronic block. The operating of the device is controlled out by means of a personal computer, which is connected to the electronic block.

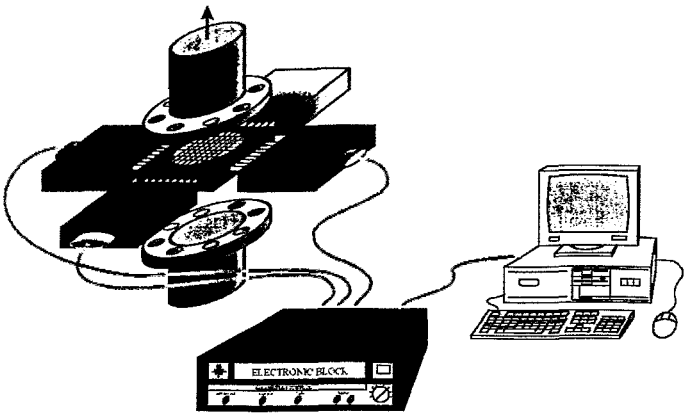

Fig. 2. Schematic view of the ultrasonic wave-guide system

3. Sensor design

Basic element of the ultrasonic wave-guide system is the ultrasonic mesh sensor. Two types of sensors have been developed (Fig. 3.). The first sensor consists of a metallic frame where transmitter and receiver wave-guides are fixed. Design and layout of the wave-guides are such, that 48 sensitive points are formed, which are equally distributed over the cross section of the pipeline with nominal diameter of 50 mm. The second sensor consists of two planes of wire grids with 7 wires in each. This results 37 sensitive points over the cross section. In the first sensor the control volumes are formed between cylindrical transmitter wave-guides and perpendicularly located receivers. The main advantage of this prototype is a high sensitivity of the sensor. The control volumes in the second sensor are formed between transmitter and receiver wave-guides, which have special concavities to increase the sensitivity of the sensor. The main advantage of this prototype compared to the first one is the simplicity of the construction.

Both types of sensor are manufactured from corrosion proof steel. It allows to use the sensors for two-phase flow measurements even under hostile condition, which are met in industrial facilities.

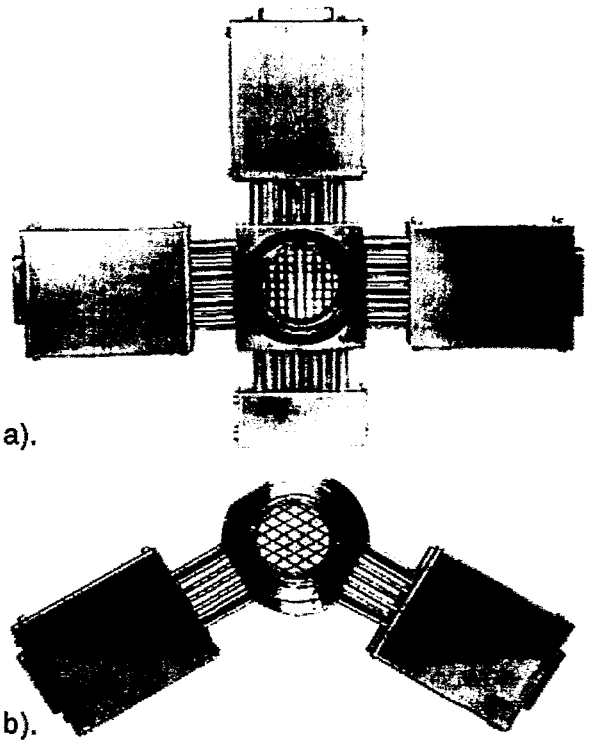

Fig. 3. Two types of ultrasonic mesch sensors
a) Prototype-1 (48 sensitive points)
b) Prototype-2 (37 sensitive points)

4. The peculiarities of the electronic hardware

The electronic block contains an electronic circuit for the control of the device. The basic control and measuring signals are shown in Fig. 4.

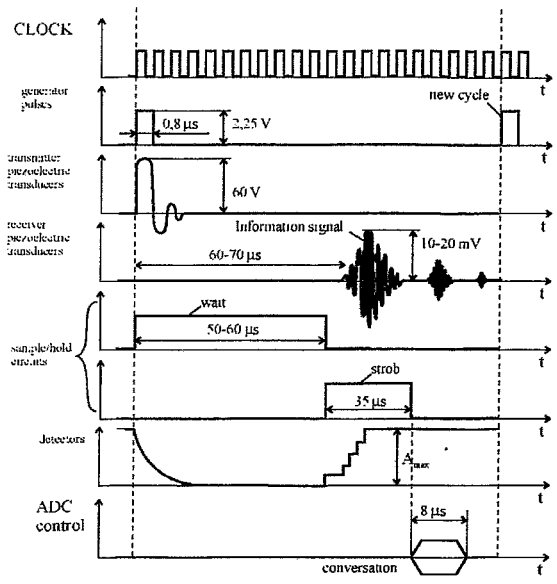

Fig. 4. Diagram of the control signals and the signal acquisition

5. Experimental tests in an air-water flow

Both types of ultrasonic mesh sensors were tested at the two-phase flow loop of Research Centre Rossendorf. First experiments were carried out under carefully controlled conditions, at atmospheric pressure and room temperature. The measurements were carried out in a wide range of water and air velocities.

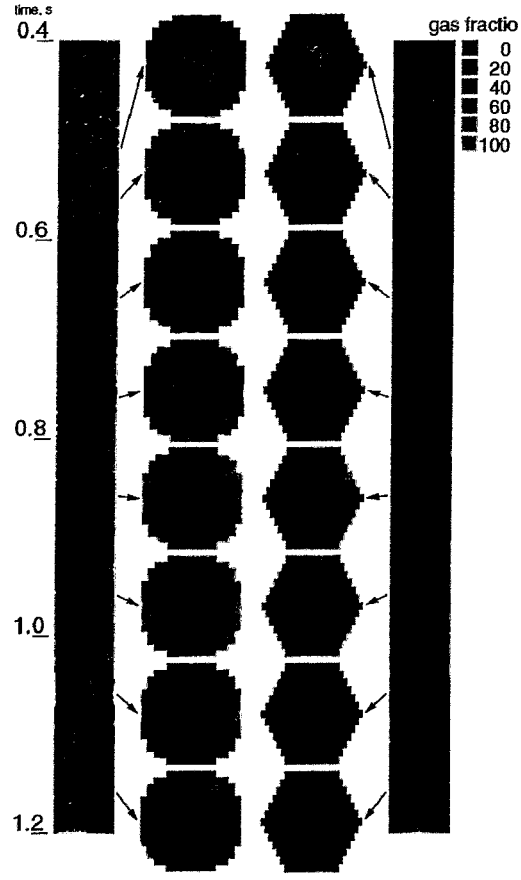

Fig. 5. Comparison of sequences of frames and virtual sectional views originating from a vertical plug flow
left: electrical wire-mesh sensor
rihgt: ultrasonic mesh sensor

Fig. 5 shows the qualitative comparison of sequences of individual frames and virtual sectional views recorded in a vertical plug flow with the ultrasonic mesh sensor and electrical wire-mesh sensor [3].

Fig. 6 shows the qualitative comparison of the virtual sectional views for bubble, plug and annular flows. The pictures obtained by the electrical wire mesh and the ultrasonic mesh sensor are slightly different. It is visible, that the ultrasonic device often indicates too much water in the cross section.

The main reason of the disagreement between the results is the lower spatial and time resolution of the ultrasonic device. To increase the quality of the imaging, a linear interpolation within the cross-sectional images for ultrasonic mesh sensor was applied.

For the quantitative comparison between wire mesh sensor and ultrasound wave-guide sensor, the average volumetric gas fractions of time and diameter were used. The measured average volumetric gas fraction for the superficial velocities of 1 m/s for water and 0-12 m/s for air is shown on Fig. 7. The ultrasound wave-guide sensor produced a negative systematic error in the range of big bubble and plug flows and a positive systematic error in the range of small bubble and annular flows. The basic systematic errors are due to low spatial and time resolution of the wave-guide sensors. Except for these errors, there are errors due to influence of the sensor on the flow. At a low superficial velocity of air, droplets accommodate between transmitter and receiver wave-guides. They have a significant effect on the reading of the ultrasound device. At a high superficial velocity of air artefacts are observed, because acoustic emission takes place in the ultrasound wave-guides.

The effect of acoustic emission on the readings of the ultrasonic sensors was estimated. The results are shown in Fig. 8. In order to minimised the effect of acoustic emission a protecting grid of metallic rods can be mounted just in front of wave-guides.

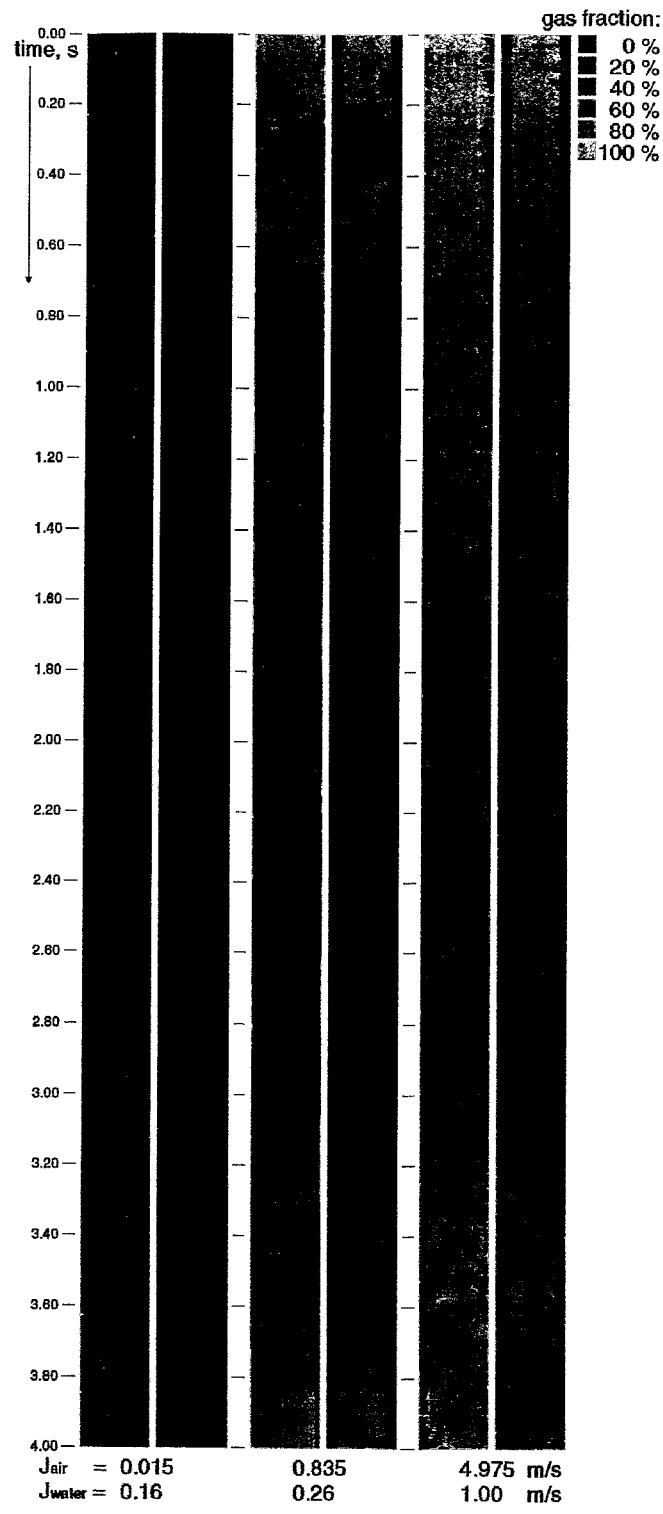

Fig. 6. Virtual sectional views for different flow regims
left column: electrical wire-mesh sensor
rihgt column: ultrasonic mesh sensor

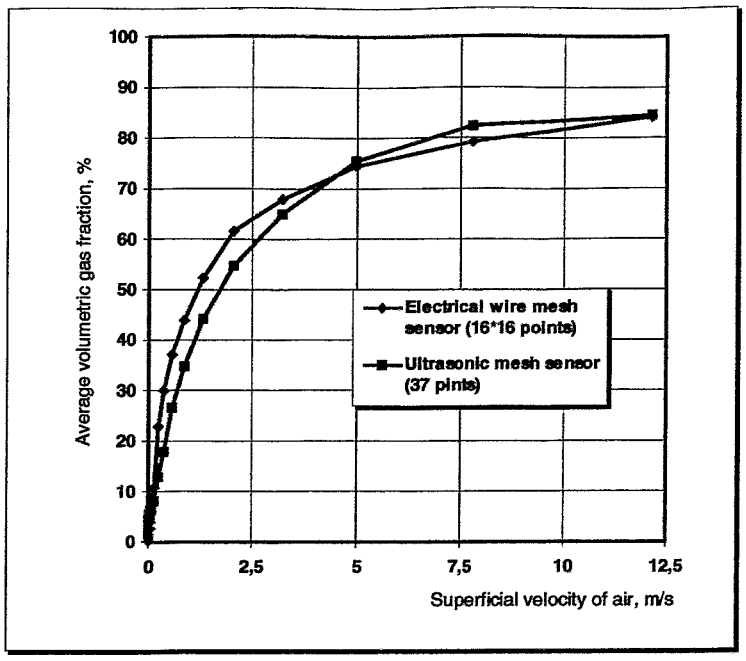

Fig. 7. Comparison of average volumetric gas fractions measured by the electrical wire-mesh sensor and the ultrasonic mesh sensor

Diameter of the pipe: 51.2 mm; superficial velocity, water: 1m/s; sensors: electrical wire-mesh (256 sensitive points) ultrasonic mesh (37 sensitive points)

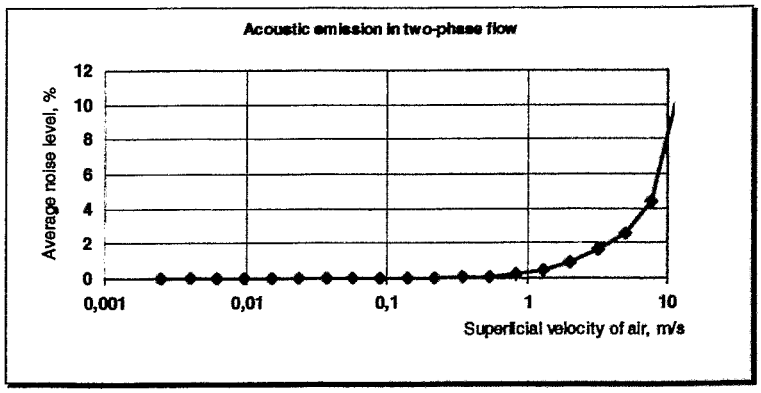

Fig. 8. Effect of acoustic emission on the readings of the ultrasonic device

5. Experimental tests in a steam-water flow

The ultrasonic mesh sensor was also tested in a steam-water flow. Measuring points were recorded in the range from 6 to 25 bar. A quantitative comparison of the measurement results obtained by the ultrasonic mesh sensor was carried out with the readings of the needle shaped conductivity probes. The results of comparison are shown in Fig. 9.

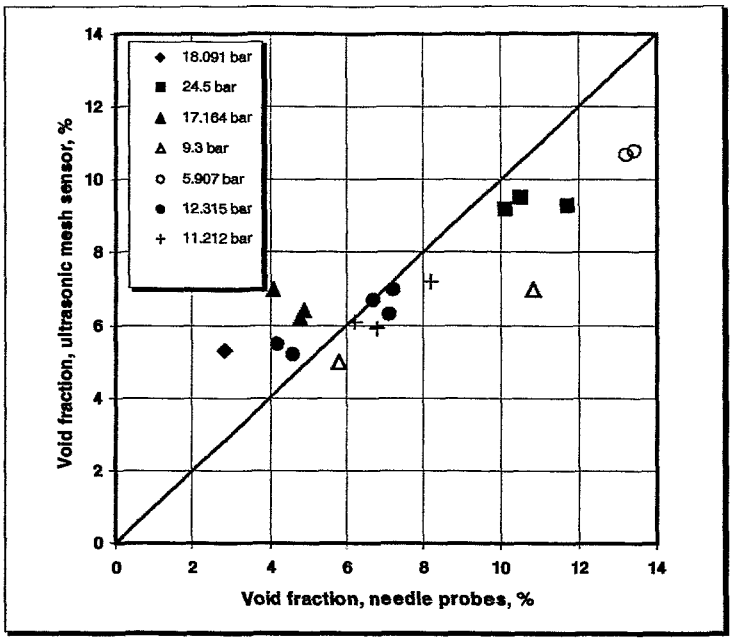

Fig. 9. Comparison between average void fractions measured by needle-shaped conductivity probes and the ultrasonic mesh sebsor in a steam-water flow

6. Conclusions

The inexpensive device for high-speed two-phase flows visualisation is developed and tested. The spatial and time resolution of the ultrasonic mesh sensor is adequate for qualitative diagnostic of the different two-phase flows. The device can be used in experimental equipment under hostile conditions. The ultrasonic mesh sensor can be used in electrically non-conductivity fluids. The ultrasonic mesh sensor is also employed in investigations of the high pressure and high temperature flows. The test results show that additional work is needed to improve the precision of the ultrasonic wave-guide device.

7. References

[1] V. V. Kontelev: "Development and investigation of an ultrasonic wave-guide system for the visualisation of a two-phase flow" (in Russian), PhD thesis work, Nishny Novgorod, June 1999.

[2] V. I. Melnikov, B. I. Nigmatulin: The newest two-phase control devices in LWR equipment based on ultrasonic and WAT-technology. Nuclear Engineering and Design, 1994, N149, P. 349-355.

[3] H.-M. Prasser, A. Böttger, J. Zschau: "A new electrode-mesh tomograph for gas-liquid flows", Flow measurement and investigation, N9 1998, P. 111-119.

WAVEGUIDE ULTRASONIC LIQUID LEVEL TRANSDUCER FOR POWER-GENERATING EQUIPMENT

Dountzev, Andrei

Niznzy Novgorod State Technical University, Russia
E-mail: melnikov@nntu.sci-nnov.ru

Fleischer, Sebastian
HS Zittau/ Gorlitz IPM, Germany
E-mail: S.fleischer@hs-zigr.de

1 INTRODUCTION

One of the most important operational parameters in power-generating equipment is the level of coolant (mass and physical). The level measurement is a part of system of operative control for equipment. The most well-known types of level measurement and in particular the float level, capacity inductometric, piezometric, radioisotope and optical gauges are exposed to the action of corrosion and thermic destruction. The thickening of the gauges to protect against high pressure damage and radiation cause problems when using the above mentioned types. That is why these types of level measurement are not used in practice.

In modern practice control of the level of two-phase coolant in the steam generator are carried out by using hydrostatic level measurement. The hydrostatic level gauges contain the sensor for measuring differential pressure and are placed in regions having normal conditions and have long joint tubes. Such a disposition of the gauges guarantees its furnace life and its reliability. However, using long connecting tubes significantly reduces the quick response of the gauge, causing errors of measurement and reduced safety of the unit. The progressive level gauges for steam generators, in our opinion, are acoustic level gauges based on the waveguide transducer. The reasons of such a conclusion are:

- the sensor is produced from austenite steel and does not contain insulators or other elements made from nonmetallic materials;
- the sensor is thickened by using welding or solder;
- high temperature, pressure and irradiation do not have a significant effect on convection of ultrasound in the waveguide;
- the waveguide lines can be crooked;
- the acoustic transformer is placed in normal conditions.

2 PHYSICAL BASIS

The basic principle of ultrasonic coolant level transducers is a local acoustic sounding method [1]. This method is based on indication of the gaseous phase in control point, between the end of two waveguides (so-called sensing elements). When in control point the liquid phase, ultrasound is gone from radiator to receiver, when gas-

ultrasound is no gone. The radiation of acoustic waves occurs only in the liquid because the gas phase has low wave impedance. It is possible to calculate the local volumetric steam fraction by relating the total time of steam detection to the measuring period:

$$\varphi = \Sigma\tau_i / T$$

where τ_i is the time of steam detection during an individual big bubble contact (contact time).

The statistical distribution of contact time can be transformed into a big bubble size distribution (length of steam cork), when the velocity of the bubbles is known. The several control points are located on line, one after another. In this case it is possible to measure the velocity for big single bubble (spreading time between two points) and height of foam of boiling water. The minimum size of a bubble mast be greater then the distance between the end of two waveguides.

The transducer operates as follows (Fig. 1,2). Acoustic impulses, created by the first converter, spread along the communication waveguide to the first sensing element and are radiated in the water. Then the acoustic impulses are received by the second sensing element and are reflected to the second converter. The indication of steam phase in the control point is carried out by discriminating the pulses received.

3 DESIGN AND EXPERIMENTAL TESTING OF AN ACOUSTIC TRANSDUCER

For the realization of the described acoustic methods the waveguide ultrasonic transducer was produced by NNTU N. Novgorod with the participation of IPM Zittau (Fig. 3,4). The basic elements of the transducer are pairs of parallel waveguides with diameter of 0,8 mm, the top ends of them are connected to conic concentrators, and the bottom ends, put into the coolant are form the control volume. The waveguide communication lines are placed inside a two protective tubes, each has a diameter 10 mm. The minimum length of waveguide is 255 mm, maximal length of waveguide is 850 mm. The transducer was made of chromium- nickel steel. The converters are made of crystal-ceramic. The radiators are connected to the output cascades of generator. The receiver are connected to input cascades of amplifiers. Operating frequency of transducer is 500 kHz, impulse frequency is 200 Hz . The working parameters are : pressure up to 16 MPa; temperature up to 400 °C. The amplifiers of the transducer can operate in an environmental temperature of up to 100 °C. The maximal length of waveguide can be up to 5 m. The seven control volumes are located on line one after another.

The personal computer acts as a signal acquisition unit. The primary probe signal is displayed graphically. The computer program allows the setting of the working parameters, such as period of measuring, position of strobe, amplitude of signal, it is possible to store and to accumulate results as digital files for the next processing of experimental data.

Experimental tests of transducer and measurement methods were carried out at the test facility of IPM Zittau. The transducer was installed in the vertical gauging tube with the diameter of 45 mm and length of 1m.

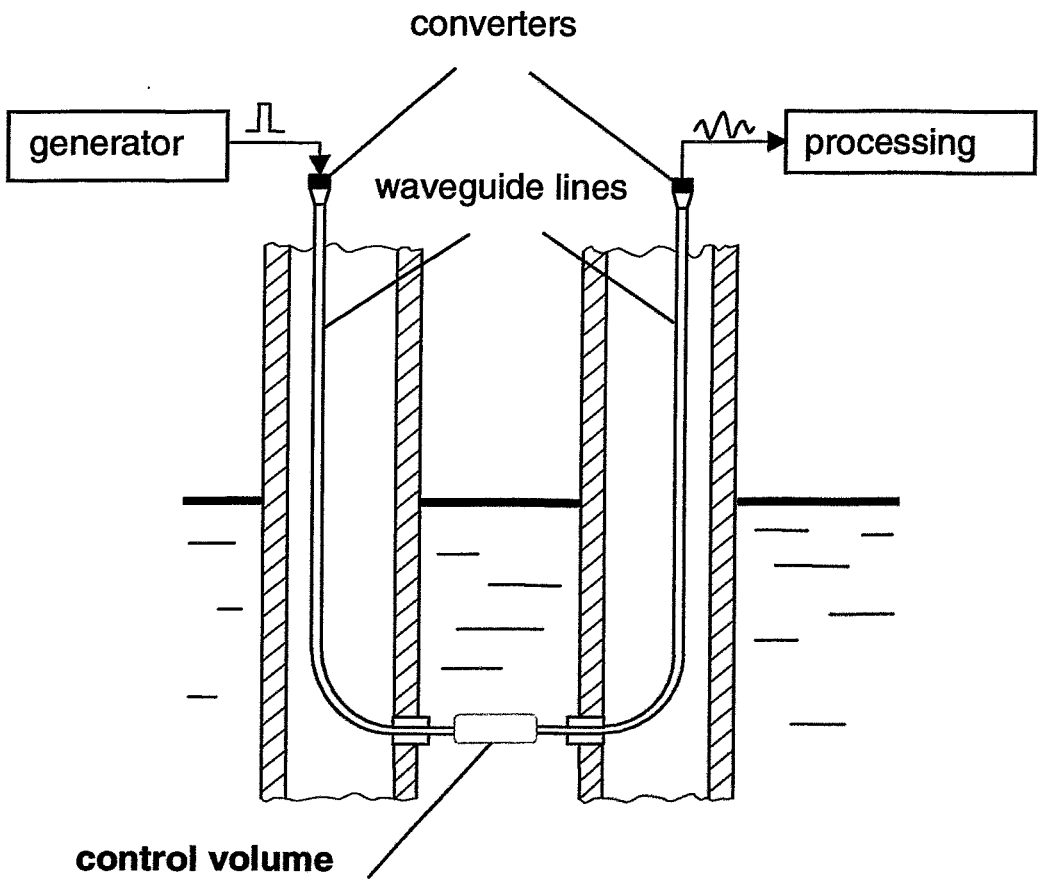

Fig. 1 Diagram of operation of the transducer

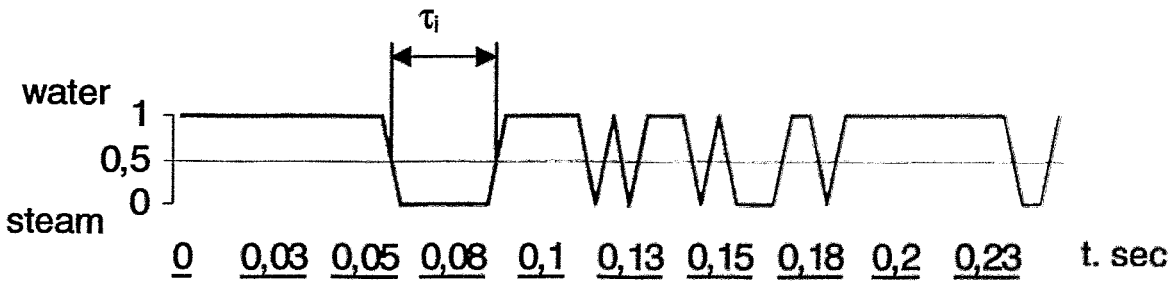

Fig. 2 Typical output signal

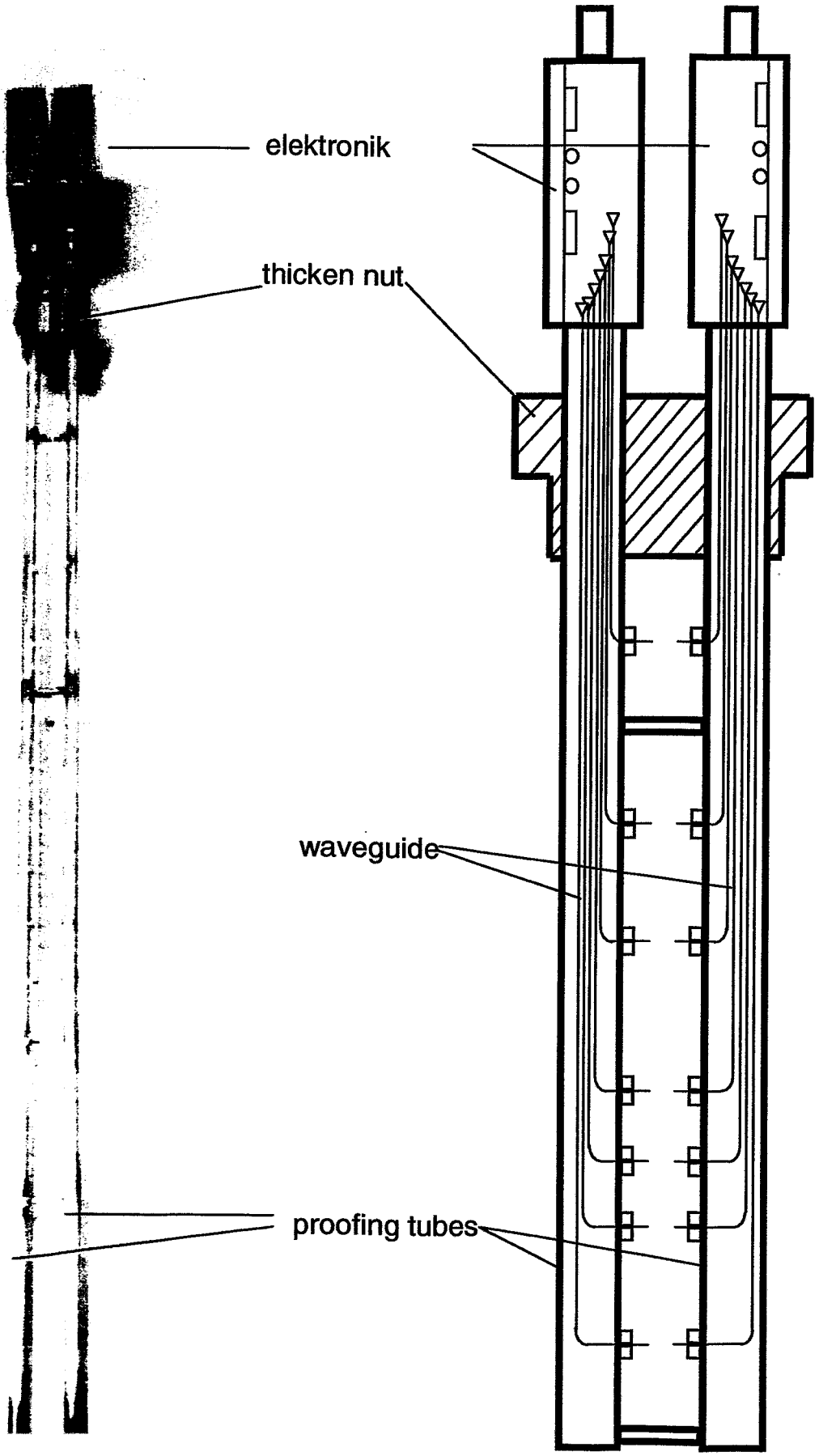

Fig.3 Design of the waveguide ultrasonic transducer

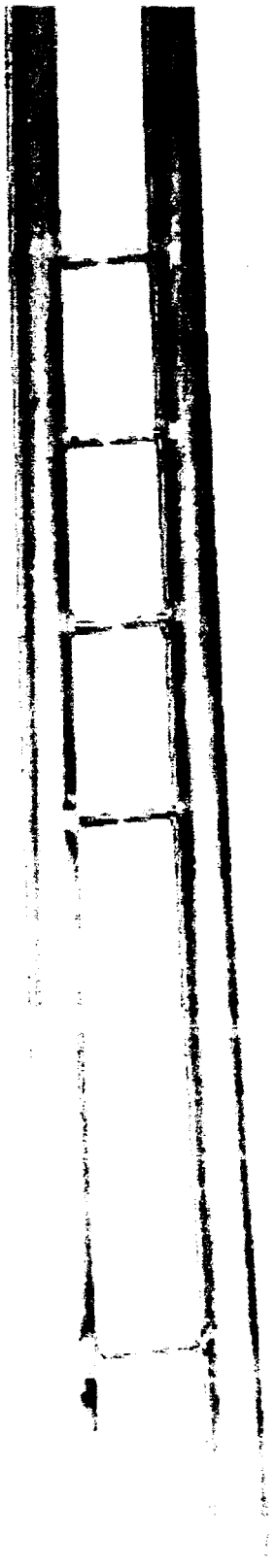

Fig. 4 The control volumes

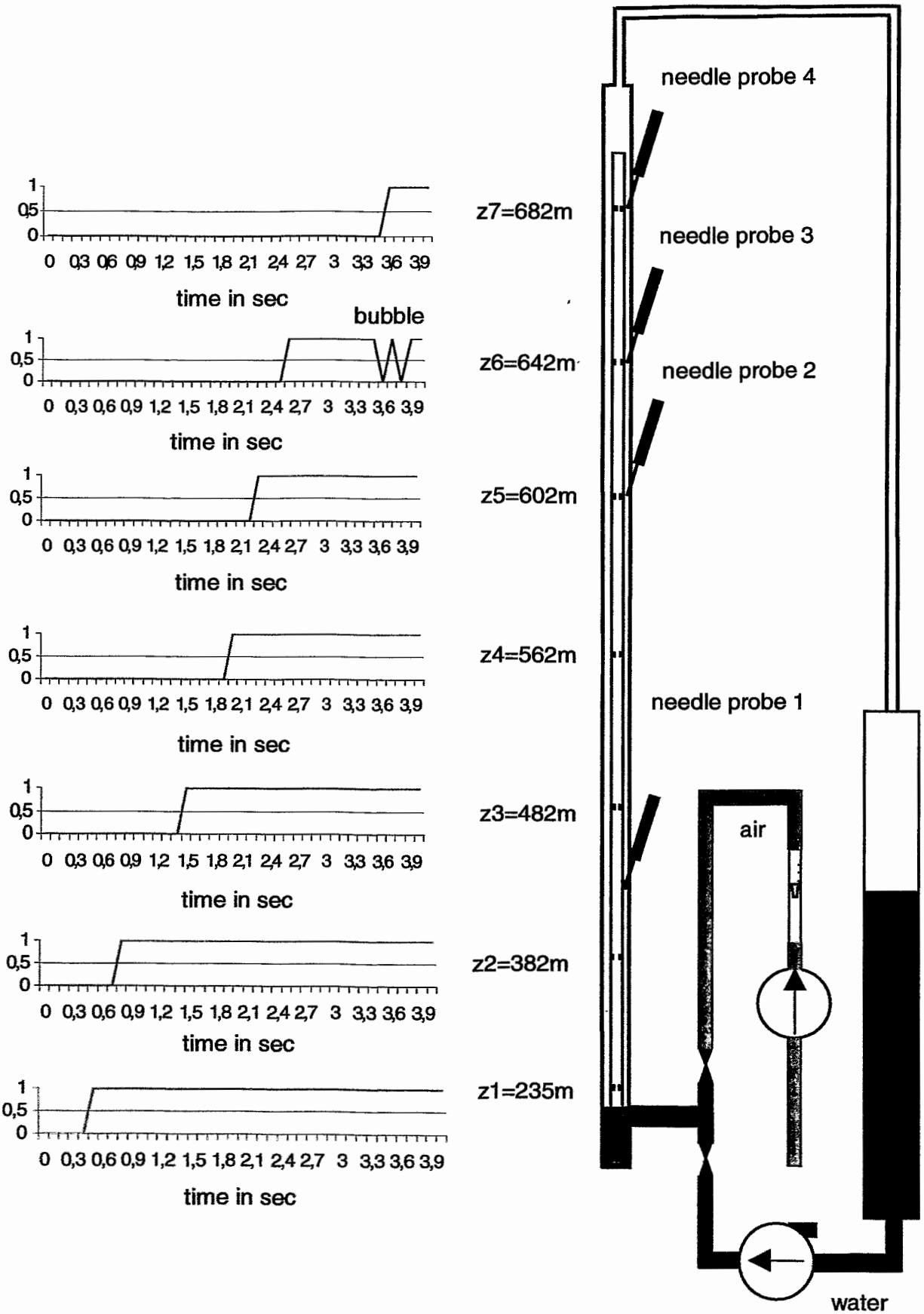

Fig. 5 Test facility and transducer signals for a fill-in experiment

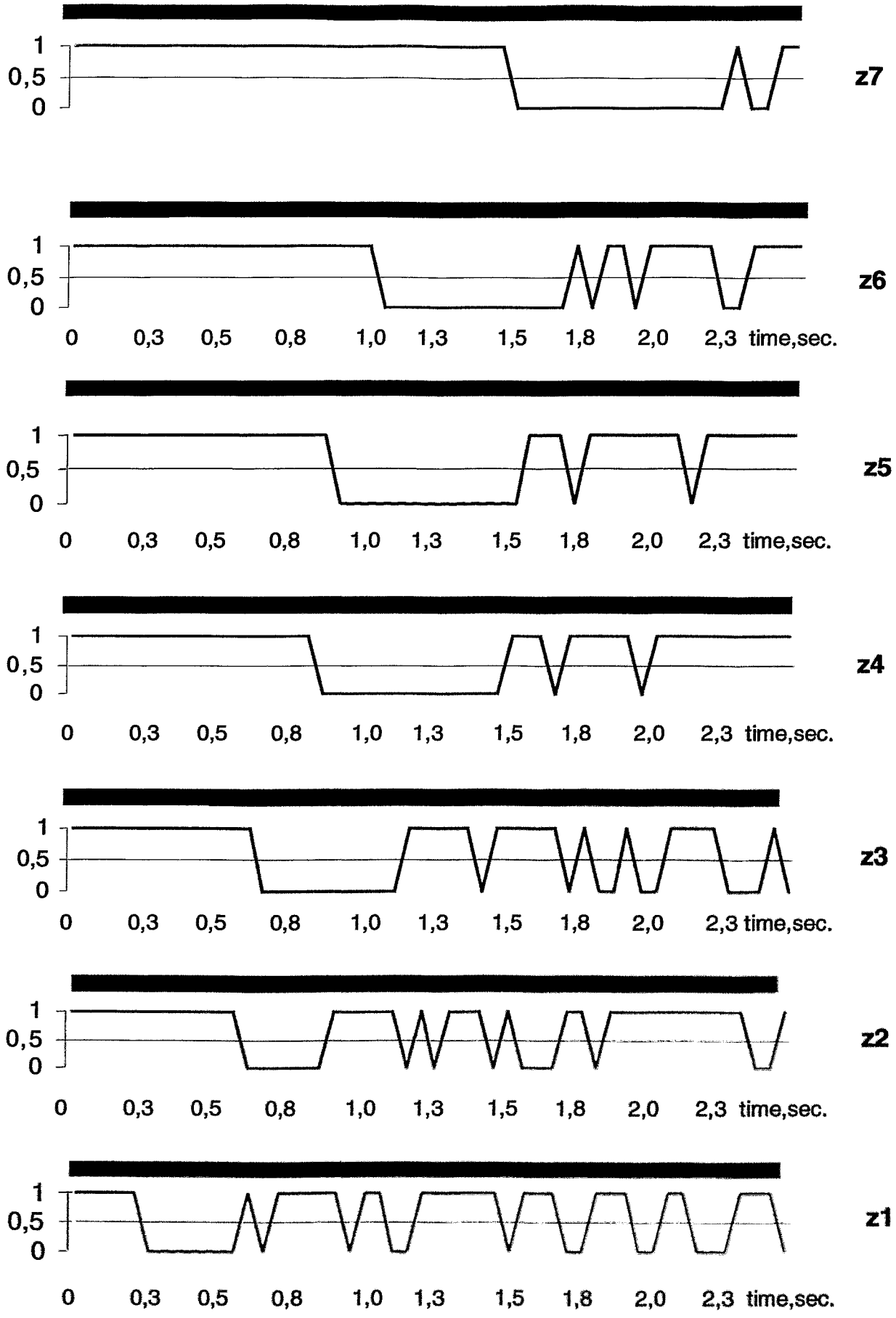

Fig. 6 Output signals for rising of the big bubble

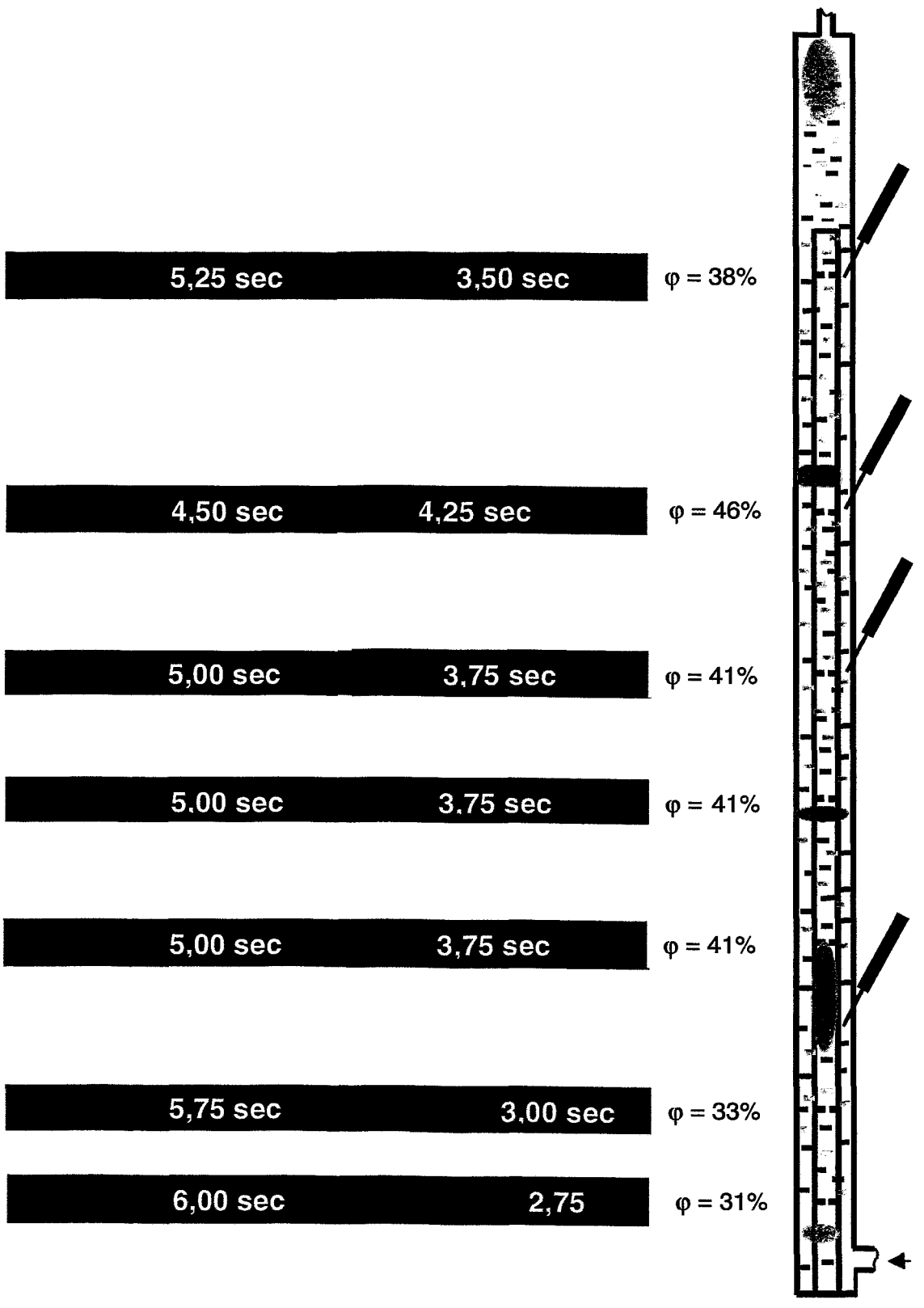

Fig.7 Distribution of gas content at the measuring tube

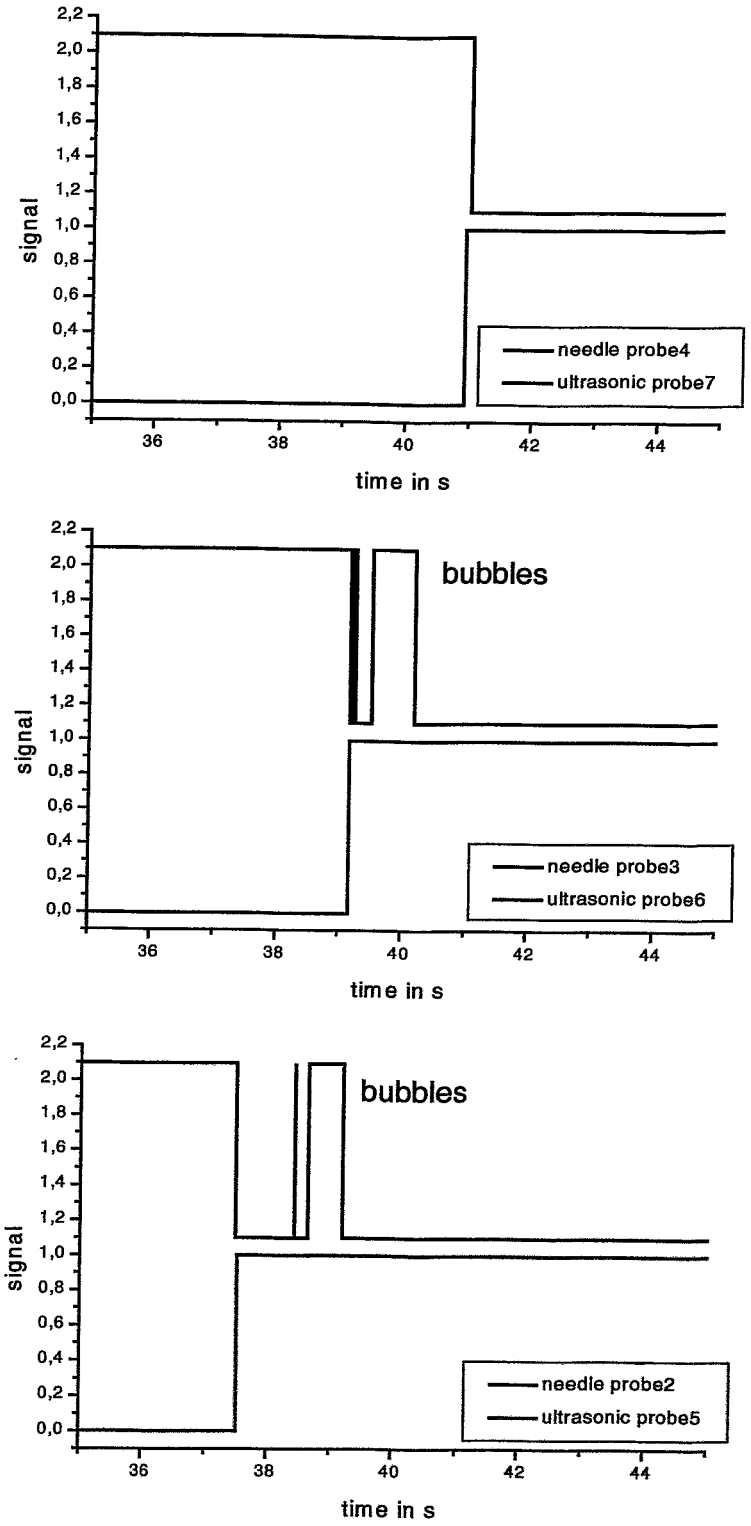

Fig.8 Output signals of ultrasonic transducer and needle probes for a fill-in experiment.

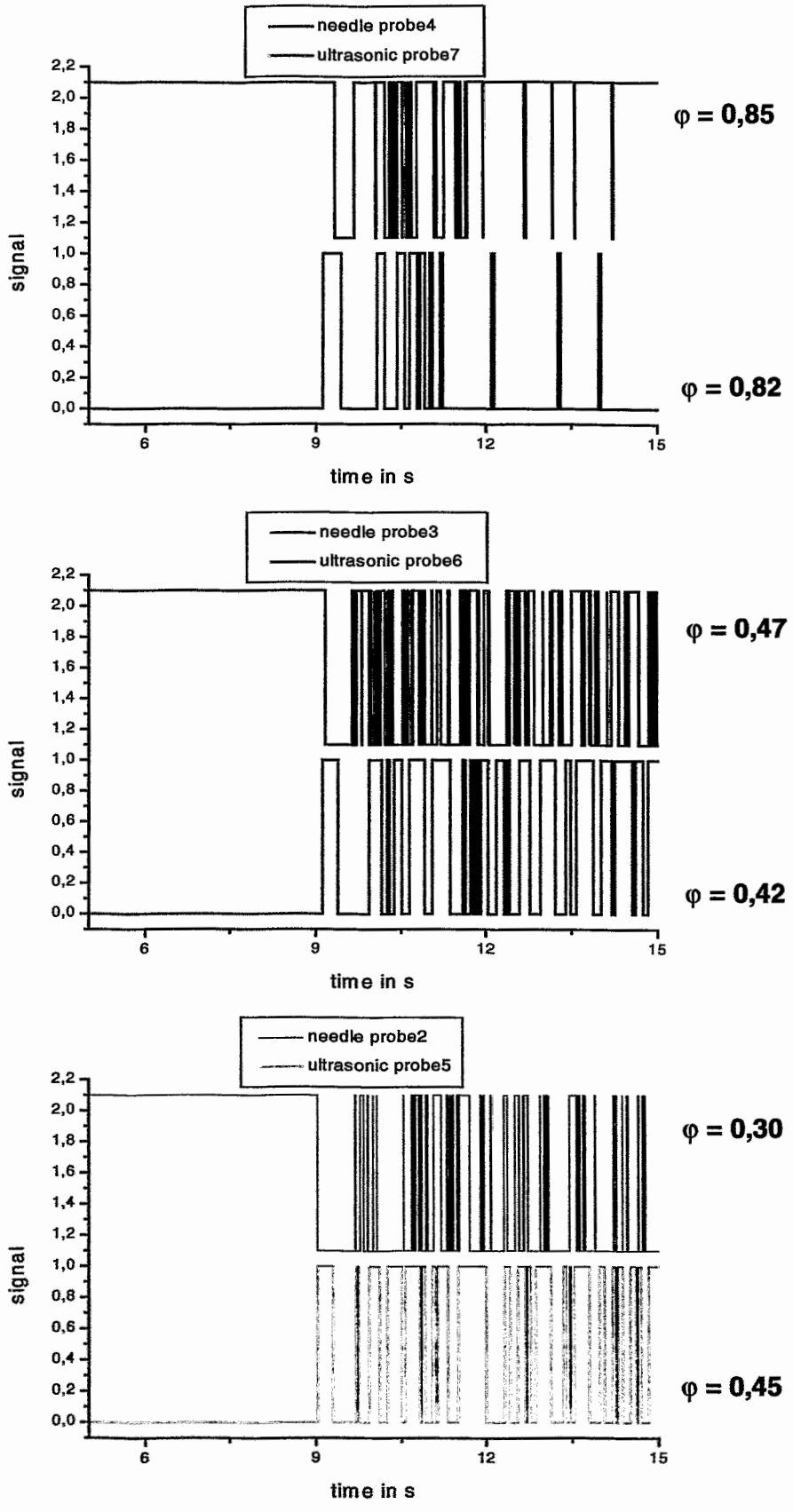

Fig.9 Output signals of ultrasonic transducer and needle probes for a pressure decreasing experiment

Control measurements were carried out by using a bubbling device simulating a two-phase flow under normal condition. The processing models of leveling change (Fig. 5) and different regimes of two-phase flow (Fig.6) were made. For big gas contents and mixture level is possible to determining the distribution of gas content at the measuring tube (Fig. 7). The results of comparative experiments with needle shaped conductivity probes are represented on Fig. 8 and Fig. 9. Some difference between signals are caused by difference position of sensors and hydrodynamic phenomenon's.

4 CONCLUSIONS

The new waveguide ultrasonic transducer has successfully been used for liquid level measurement at two-phase flow experiments. The application of the acoustic waveguide provides high stability and reliability for the transducer, as the acoustic converter is placed outside the high-temperature zone and is not subjected to extreme effects.

REFERENCE

1. Melnikov V.I., Usinin G.B. Acoustic methods of diagnostics of two-phase coolants in NPP. Moscow. Energoatomizdat,1987.

2. Isakovish I.P. Common acoustics. Moscow. Science. 1973.

FAST WIRE-MESH SENSORS FOR GAS-LIQUID FLOWS AND DECOMPOSITION OF GAS FRACTION PROFILES ACCORDING TO BUBBLE SIZE CLASSES

H.-M. Prasser, E. Krepper, D. Lucas, J. Zschau[1)], D. Peters, G. Pietzsch, W. Taubert, M. Trepte[2)]

[1)] Forschungszentrum Rossendorf e.V., P.O.Box 510119, D-01314 Dresden, Germany
e-mail: prasser@fz-rossendorf.de

[2)] Teletronic Ingenieurbüro GmbH, Bautzner Landstraße 45, D-01454 Großerkmannsdorf
e-mail: ttronic@teletronic.tz-rotech.de

1 Introduction

The described electrode-mesh sensor is based on a measurement of the local instantaneous conductivity of the two-phase mixture. Wire-mesh sensors were introduced by Johnson [1], who used them to measure the integral gas fraction in the cross section. Reinecke et al. [2] presented a device visualising sequences of gas fraction distributions with a rate of about 100 frames per second for the first time. It consists of three layers of electrode grids. Three independent projections of the gas fraction distribution in the sensor cross section are obtained by measuring the impedance between two adjacent parallel wires. The imaging is carried out applying tomographic reconstruction algorithms. Our own development was aimed at a direct conductivity measurement between pairs of crossing wires to avoid tomographic reconstruction algorithms [3] and to increase time resolution. The first generation of signal acquisition units worked at a framing rate of 1200 Hz. Recently, the second generation has achieved a time resolution of 10 000 frames per second [4].

Both types were used to study a vertical upwards air-water flow in a pipe of 51.2 mm diameter. The high resolution allows to derive bubble size distributions and gas fraction profiles decomposed according to bubble size classes. The processes of lateral movement of the bubbles due to the non-drag forces, the bubble coalescence and fragmentation were investigated by studying the evolution of these partial profiles along the pipe. The effect of lift force inverse at some critical diameter of the bubbles, predicted by [5], was clearly detected in a realistic, polydisperse two-phase flow. Especially with the second generation device, the structure of the two-phase flow in case of air and water velocities in the range of 10 m/s was visualised in detail for the first time.

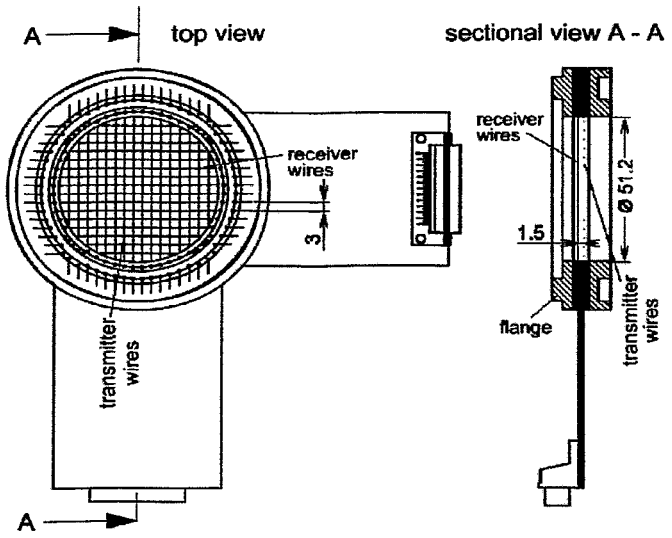

Fig. 1: Wire-mesh sensor with 2 x 16 electrodes

2 Function of the wire-mesh sensor

Our wire-mesh sensor consists of two electrode grids with 16 electrode wires (diameter 120 µm) each, placed at an axial distance of 1.5 mm behind each other (Fig. 1). The electrode pitch is 3 mm, which is determining the spatial resolution.

In order to explain the function, a simplified scheme of the sensor together with its electronic circuitry is shown in Fig. 2. Here, for simplicity, the number of electrodes is reduced to four in each plane. During the signal acquisition, one plane of electrode wires is used as transmitter, the other as receiver plane. The transmitter electrodes are activated by supplying them with voltage pulses in a successive order. This is done by closing one of the semiconductor switches S1 - S4 for the duration of the excitation pulse.

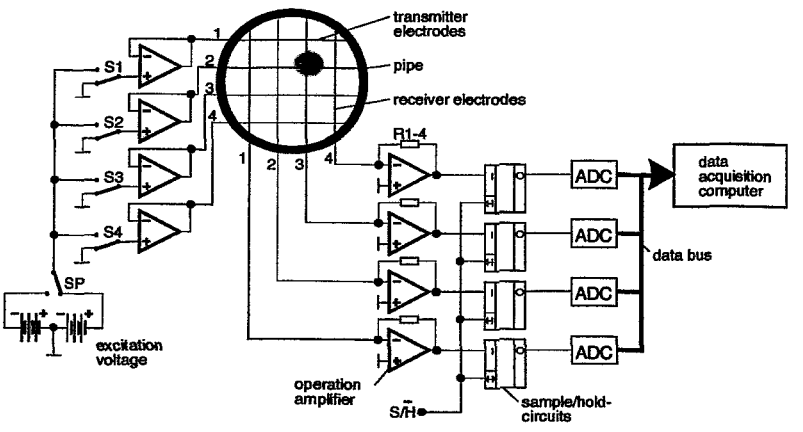

Fig. 2 Simplified scheme of wire-mesh sensor and signal acquisition electronics

To suppress electrode polarisation and electrolysis at the electrode, the excitation is carried out by putting a DC free symmetrical bipolar square-wave pulse on the transmitter electrode to be activated (signal U_{T2} in Fig. 3). For this purpose, the polarity is altered by changing switch SP after the first half period of the excitation pulse. The corresponding binary signals to control the switches are shown in Fig. 3.

Due to the imaginary component of the impedance of the ion layer at the electrodes, the sensor and the cable, the resulting currents arriving at the receiver wires show a transient behaviour (see signal I_{R2} in Fig. 3). These signals are pre-amplified and sampled by activating sample & hold circuits (S/H) at the end of the first half-period of the excitation pulse (signal S/H in Fig. 3). At this moment, the transient has settled and the output voltage of the S/H circuits is proportional to the real component of the received current. This

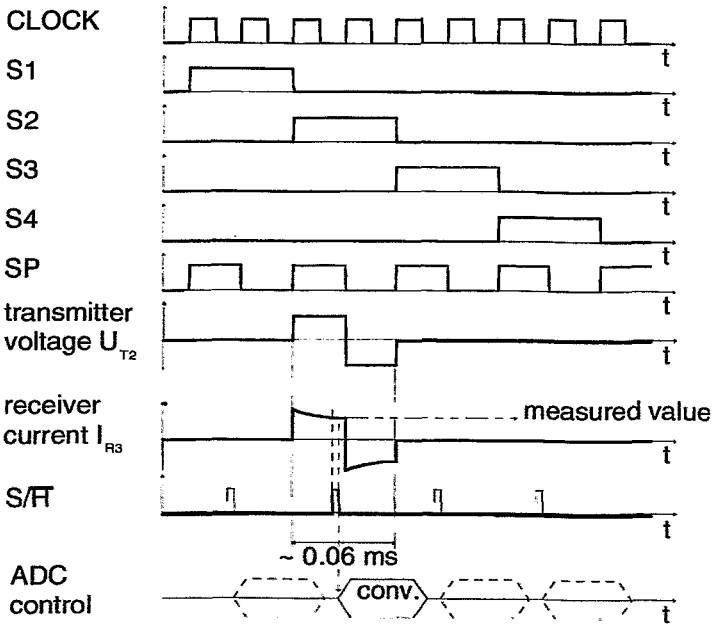

Fig. 3 Pulse diagram of the most important control signals of the signal acquisition electronics

has several advantages compared to a traditional AC excitation with a sinusoidal voltage, requiring a demodulation of the received alternating currents with a subsequent low-passing to remove the carrier frequency. The low-passing makes it necessary to apply a carrier frequency that is higher than the measuring rate by an order of magnitude, while in case of the square-wave excitation the excitation frequency and measuring rate can be equal. This helps to increase the measuring frequency to achieve high framing rates.

After the pre-amplification, the analogue signals are captured by the S/H circuits, digitalised by analogue/digital converters and stored in a data acquisition computer. This procedure is repeated for all transmitter electrodes. After activating the last transmitter wire, a complete matrix of measured values is stored in the computer (4 x 4 =16 values in case of the simplified sensor in Fig. 2, 16 x 16 = 256 values in case of 2 x 16 electrode wires), which represents the complete two-dimensional conductivity distribution in the sensor cross section. The local instantaneous conductivity is measured at each crossing point of a transmitter and a receiver wire independently. In case of the sensor shown in Fig. 1 there are 242 useful crossing points within the cross section of the sensor, the rest is located outside the circular measuring area.

The time sequence control of the measurement is carried out a device-specific FPGA (Freely Programmable Gate Array). For the data communication a parallel interface to the ISA bus of the PC with a bus width of 16 bit is used. A special interface card was developed, which has to be placed into the PC. The time sequence of the successive activation of the transmitter wires and the data transfer is controlled from the side of the PC. The interface card is linked with the signal acquisition unit of the wire-mesh sensor over an approximately 3 m long cable. The time sequence of the successive activation of the transmitter wires is controlled from the side of the PC. Before the measurement is started, a set of control words is transferred to the signal acquisition unit and stored in the FPGA. In these control words, the amplifying stages of the pre- and post-amplifier cascades are set, the number of electrodes in the wire mesh sensor and the excitation pulse width must be specified.

The length of the excitation pulse is programmable in the range from 3 to 19 µs. When a period of less than 0.06 ms is set, the total measuring cycle in case of 16 transmitter electrodes takes less than 1 ms. In the result, the time resolution achieved by the signal processing unit of the first generation is 1200 frames per second. This limit is also given by the capacity of the parallel interface used to transfer the data to the data acquisition PC.

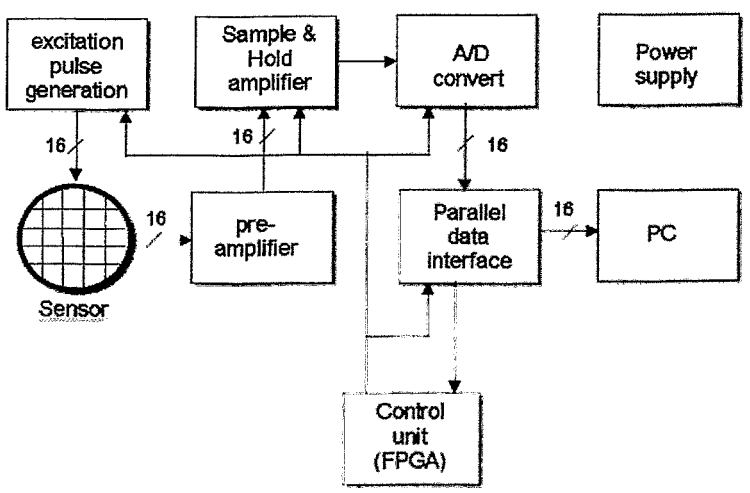

Fig. 4 Structural scheme of the signal acquisition unit for 1200 frames per second

An important feature is the suppression of cross-talk. A large part of the excitation current is flowing from the activated transmitter wire to the adjacent parallel non-activated transmitter wires. Cross talk may happen, if the potential of the non-activated electrodes departs from zero due to these parasitic currents, because the appearing potential difference causes currents from the non-activated transmitter electrodes to the receiver wires. This results in a loss of resolution (blurring) in the direction perpendicular to the transmitter wires. The similar may happen, if the currents arriving at the receiver wires are able to create a non-zero potential on the receivers. In this case, parasitic currents between adjacent parallel receiver wires occur and the image loses sharpness in the direction perpendicular to the receiver wires.

The cross-talk is sufficiently suppressed by applying driver circuits and pre-amplifiers with low output respectively input impedance to generate the excitation pulses and to measure the currents. In order to drive the transmission electrodes with an impedance as low as possible, an individual operational amplifier is foreseen for each electrode. The current entries at the receiver electrodes are converted in a voltage signal by operation amplifier (OPV) with small input bias current, switched as impedance converters. By the help of the low-impedance the potential of all transmitter and receiver wires except the currently activated one is kept on zero potential, so that parasitic currents cannot occur.

For a sufficient cross-talk suppression the impedance of the input and output cascades must be significantly less than the impedance of the sensor immersed into the measuring fluid. This leads to limitations concerning the maximum conductivity of the liquid phase. Without additional measures, the device can work at liquid conductivities up to approximately 1000 µS/cm (tap water quality), the lower limit is given by the sensitivity of the input cascades (0.1 µS/cm, distilled water). Only due to the cross-talk suppression it is possible to obtain instantaneous gas fraction distributions with a spatial resolution equal to the electrode pitch.

3 Second generation signal acquisition unit with 10 000 frames per second

For an increase of the measuring rate from 1200 frames/s to the desired 10 kHz it was necessary to decrease the build-up time of the preamplifiers and to speed-up the data transfer from the signal acquisition unit to the data acquisition PC. It turned out, that the high quantity of data produced at the 10 000 frames per second cannot be transferred on-line. In the consequence, the data acquisition module was equipped with an own memory unit. Furthermore, it was decided to modify the signal sampling by using both half-periods of the bipolar excitation pulse. For this purpose, the Sample & Hold circuits are activated at the end of both the positive and the negative half-periods. The results of both samplings are subtracted digitally after the A/D conversion. This technique allows to suppress low-frequency noise, such as 50 Hz mains disturbances.

These specifications led to a completely new conception with the following modifications in relation to the first device version. Main difference is the introduction of a DSP (digital signal processor) for the control of the measurement. The new structure is shown in the block diagram (Fig. 5). The new features are:

1. The entire signal acquisition procedure is operated autonomously, controlled by a DSP.

2. The measured data (up to 170.000 frames) are stored in a buffer memory controlled by the DSP.

3. The data transfer is between signal acquisition unit and data acquisition PC is carried out via an Ethernet interface.

4. The sixteen output cascades driving the transmitter electrodes and the current-to-voltage converter cascades of the preamplifiers were put into separate functional units, which are directly plugged to the connectors of the sensor. The cables carry pre-amplified signals, which helps to reduce noise.

5. The receiver signals are sampled during the positive and the negative half-period (see explanation above).

6. The signal processing after the A/D conversion, including the subtraction of the half-periods, is fully digital, it is carried out by a programmable FPGA.

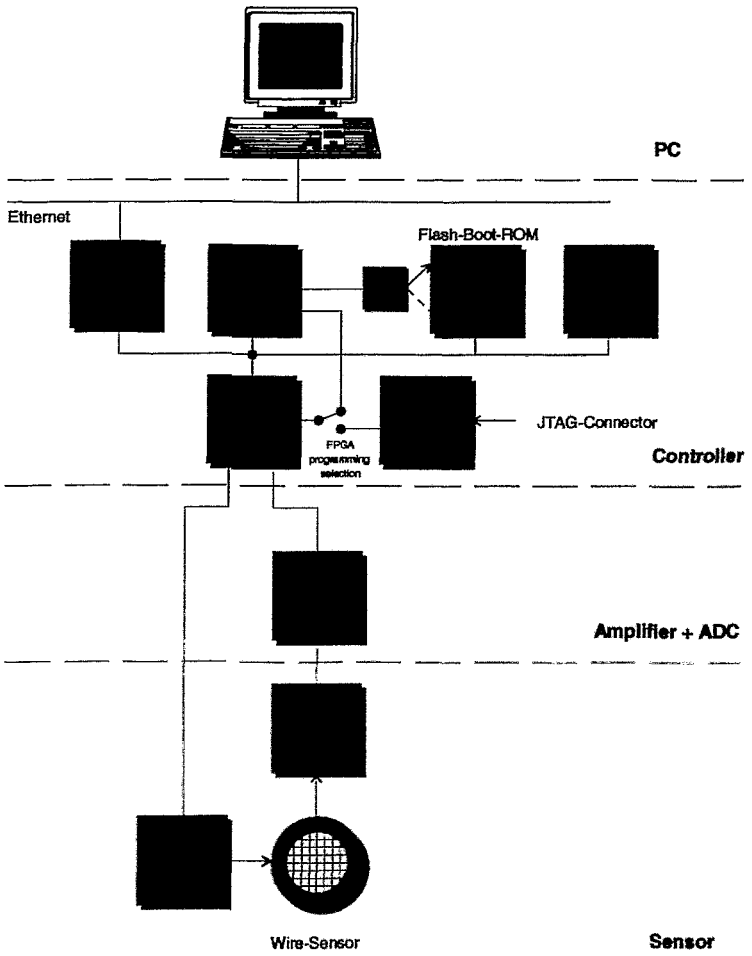

Fig 5: Structure of the second generation device with an imaging rate of 10 000 frames per second

While the measures 1 to 3 are necessary for a fast data transfer, measure 4 reduces the capacitive loads of the transmitter output cascades, the build-up time of the current-to-voltage cascades of the receiver amplifiers due to cable capacitance reduction and the amplitude of external disturbances. It furthermore eliminates the cable resistance between the transmitter and receiver cascades and the sensor electrodes, which results in a better suppression of cross-talk. Together with measure 5, a significant improvement of the properties of the system sensor excitation - sensor / pre-amplifier and of the signal quality, especially an increase of the signal-to-noise ratio was achieved. By measure 6, a reduction of the signal processing efforts were achieved.

For the preamplifiers the same operation amplifier circuits are used, as with the version for 1200 frames per second. By the arrangement of the sixteen output cascades for the control of the transmission electrodes and the sixteen current-to-voltage converters in separate, well screened housings directly plugged to the sensor and protected against electromagnetic disturbances, the necessary reduction in build-up time was achieved. The logic control of these remote functional units was implemented by a bus-system, which allows a simultaneous control of several of these units. In this way, the device is prepared for an operation with sensors of up to 64 x 64 measuring points.

The positive and negative amplitude of the excitation voltage for the transmitter electrodes is programmable, the pulse time can be set up to 3 µs for each half-period. The current-to-voltage converters dispose of an identical, binary amplification control in eight steps of a factor of two each. This is also identical with the 1200 Hz version of the signal acquisition unit. The connection between the output cascades of the transmitter electrodes and the current-to-voltage converters is realised through cables, the length of which is less critical than in case of the 1200 Hz version of the device, because the cables are driven by low-impedance cascades.

4 Evaluation of the measured data

4.1 Local instantaneous gas fractions and visualisation

The sensor delivers a sequence of two-dimensional distributions of the local instantaneous conductivity, measured in each mesh formed by two crossing wires. Local instantaneous gas fractions are calculated assuming a linear dependence between gas fraction and conductivity. For this, the measured conductivity values are related to calibration values obtained for plain liquid in the measuring plane. The result is a three-dimensional data array $\varepsilon_{i,j,k}$ where k is the number of the instantaneous gas fraction distribution in the time sequence. The indices correspond to co-ordinates x,y of the local measurement in the cross section and the current time t in the following way:

$$x = i \cdot \Delta x + x_0;\ y = j \cdot \Delta y + y_0;\ t = k \cdot \Delta t = \frac{k}{f_m} \qquad (1)$$

Δx and Δy are electrode pitches ($\Delta x = \Delta y = 3$ mm), f_m is the measuring frequency, $\Delta t = 1/f_m$ is the time step, x_0 and y_0 define the origin of the co-ordinate system. Any single value of $\varepsilon_{i,j,k}$ denotes, to which extend the corresponding fluid element is filled

with the gaseous phase. A visualisation can be carried out by assigning different colours to the local instantaneous gas fractions and plotting them in a grid that reflects the position of each individual control volume formed by crossing wires (Fig. 6, right side).

If the image is produced on the computer screen and refreshed with increasing time, a digital video sequence is generated.

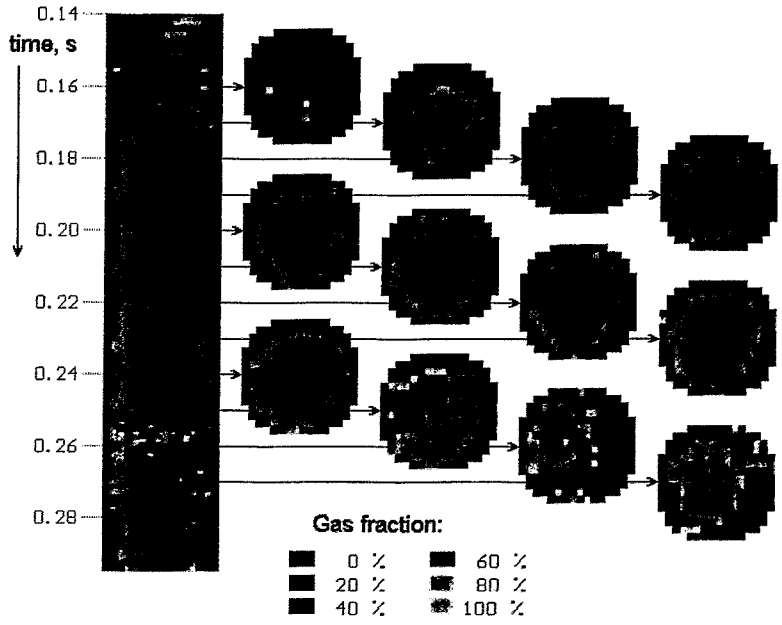

Fig. 6 Sequences of local instantaneous gas fractions obtained by the wire-mesh sensor in a vertical slug flow

A good inside into the flow structure is given by virtual sectional side-views. They are obtained by extracting the gas fraction distribution along the pipe diameter from the two-dimensional distribution and by stacking time series of these radial distributions as coloured bars in a vertical sequence (Fig. 6, left side). Additionally, in case of steady flow conditions, the time axis can be transformed into a virtual z*-axis by scaling it with the average phase velocity of the gaseous phase (see, for example, Fig. 11):

$$z^* = \overline{w_G} \cdot t \cong t \cdot J_G / \bar{\varepsilon} \tag{2}$$

The result is a virtual side-view of the flow structure. Characteristic structures, like bubbles and slugs are represented very illustratively.

4.2 Gas fraction profiles

A time-averaged two-dimensional gas fraction distribution is calculated as follows:

$$\bar{\varepsilon}_{i,j} = \frac{1}{k_{max}} \cdot \sum_{k=1}^{k_{max}} \varepsilon_{i,j,k} \tag{3}$$

where k_{max} is the number of instantaneous gas fraction distributions in the measuring sequence. A total average (void fraction) is obtained, when we average over the cross section:

$$\bar{\varepsilon} = \frac{1}{k_{max}} \cdot \sum_{i=1}^{i_{max}} \sum_{j=1}^{j_{max}} \sum_{k=1}^{k_{max}} a_{i,j} \cdot \varepsilon_{i,j,k} = \sum_{i=1}^{i_{max}} \sum_{j=1}^{j_{max}} a_{i,j} \cdot \bar{\varepsilon}_{i,j} \tag{4}$$

here i_{max} and j_{max} are the total numbers of electrode wires in both directions, $a_{i,j}$ are weight coefficients that express to which extend the given mesh [i,j] contributes to the total cross section of the sensor A_{sensor}. In the central region of the sensor holds $a_{i,j} = \Delta x \cdot \Delta y / A_{Sensor}$, while at the periphery the weight coefficients are less, they have to be calculated according to which extend the given mesh is partially covered by the circular border of the sensor (Fig. 7). Elements located outside the border of the sensor obtain weight coefficients equal zero.

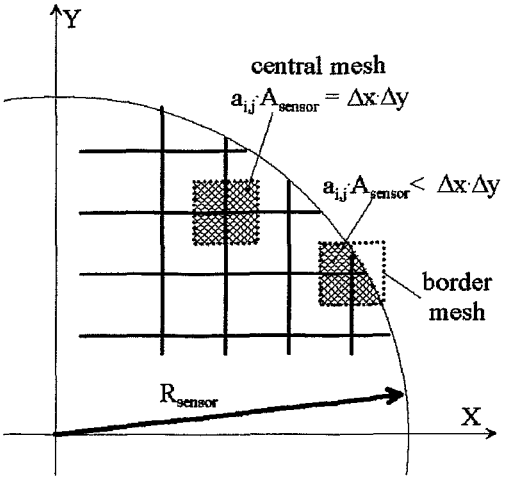

Fig. 7 Weight coefficients for averaging the gas fraction in the measuring cross section

Radial profiles can be calculated by dividing the radius into m intervals and introducing a radial step width $\Delta r = R_{sensor}/m$ and averaging $\bar{\varepsilon}_{i,j}$ over a ring-shaped domain, covering the radial interval $(m-1/2)\cdot\Delta r \le r \le (m+1/2)\cdot\Delta r$, see Fig. 8.

This is done using weight coefficients $a_{i,j,m}$, which characterise the common area of the mesh with the indices [i,j] and the ring with the number m and the central radius $m \cdot \Delta r$, related to the total cross section of the sensor A_{sensor}. The averaging can then be written as follows:

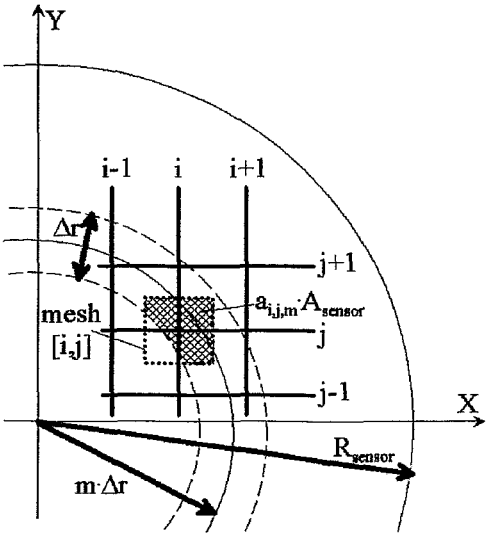

Fig. 8: Weight coefficients for calculating radial gas fraction profiles

$$\bar{\varepsilon}_m = \frac{1}{k_{max}} \cdot \sum_{i=1}^{i_{max}} \sum_{j=1}^{j_{max}} \sum_{k=1}^{k_{max}} a_{i,j,m} \cdot \varepsilon_{i,j,k} = \sum_{i=1}^{i_{max}} \sum_{j=1}^{j_{max}} a_{i,j,m} \cdot \bar{\varepsilon}_{i,j} \qquad (5)$$

The determination of the weight coefficients is based on simple geometric calculations, which does not require more detailed description.

4.3 Bubble size distributions

At moderate flow velocities, the high time resolution allows to perform a bubble size measurement, because individual bubbles are mapped in several successive frames. Furthermore, gas fraction portions belonging to bubbles the dimensions of

which exceed the electrode pitch are found in more than one mesh of the sensor. A detailed description of the method can be found in [6].

The bubble volume can therefore be derived by integrating over elements of the gas fraction distribution $\varepsilon_{i,j,k}$ belonging to the given bubble. The time necessary for the fluid element to travel through the sensor is inverse proportional to the velocity. The total gas volume flowing through one mesh of the sensor during the measuring period Δt equals $V_{G,x,y,t} = \varepsilon_{x,y,t} \cdot w_{G,x,y,t} \Delta x \Delta y \Delta t$. Here, $w_{G,x,y,t}$ is the axial component of the instantaneous local gas phase velocity. The volume can be written as:

$$V_{BL} = \Delta x \cdot \Delta y \cdot \Delta t \cdot \sum \varepsilon_{i,j,k} \cdot w_{G,i,j,k} \quad \forall [i,j,k] \in BL \tag{6}$$

From the bubble volume, an equivalent bubble diameters can be calculated:

$$D_{BL} = \sqrt[3]{\frac{6}{\pi} \cdot V_{BL}} \tag{7}$$

Before the volume can be calculated, it must be managed to identify, which elements [i,j,k] of the three-dimensional gas fraction distribution $\varepsilon_{i,j,k}$ belong to the bubble. A bubble is defined as a set of gas containing elements being in contact with each other, and which are surrounded by the liquid phase, i.e. by other elements, where the gas fraction equals zero. The task to obtain bubble size distributions can therefore be subdivided into the following steps:

- Identification of bubbles, i.e. assigning each element [i,j,k] to one of N bubbles or to the area of the solid liquid phase, which is done by a recursive fill algorithm.
- integrating the local instantaneous gas fraction over the elements belonging to the given bubble to obtain the bubble volume according to eq. (2) and transfer to an equivalent diameter, eq. (3),
- calculation of a statistical distribution with D_{BL} as variable by summing-up partial gas fractions $d\varepsilon/dD_{BL}$ carried by certain classes of bubbles.

It is still not possible to measure neither the local instantaneous gas velocity $w_{G,i,j,k}$ as a distribution over the cross section nor the velocity of each individual bubble. For this reason, the velocity was approximated by the average gas phase velocity: $w_{G,x,y,t} \cong \overline{w_G} = J_G/\bar{\varepsilon}$, i.e. non-uniformity over the cross section and fluctuations in time are neglected. This is a satisfying approximation for a rising turbulent two-phase flow in a vertical tube, in case of forced convection.

The method was tested by comparing the wire-mesh sensor data with high-speed video observations [6]. Based on a bubble size measurement using image processing techniques, the accuracy of the bubble size measurement was studied. Although the electrodes of the sensor cause significant bubble fragmentation, the recorded signal still represents the undisturbed shape and size of the bubbles.

4.4 Decomposition of gas fraction profiles according to bubble size classes

The bubble identification algorithm described in the previous chapter allows to identify, which elements [i,j,k] of the three-dimensional gas fraction distribution $\varepsilon_{i,j,k}$ belong to a given bubble.

Since the bubble diameter is known after carrying out the summation according eq. (6), it is possible to perform a decomposition of the distribution $\varepsilon_{i,j,k}$, a procedure which is illustrated in Fig. 9 (see also [7]). Here, a bubble diameter of 5.5 mm was chosen as threshold. If the resulting partial distributions are averaged applying eq. (4), partial radial gas fraction profiles can be obtained, which consider only bubbles from a given range of diameters.

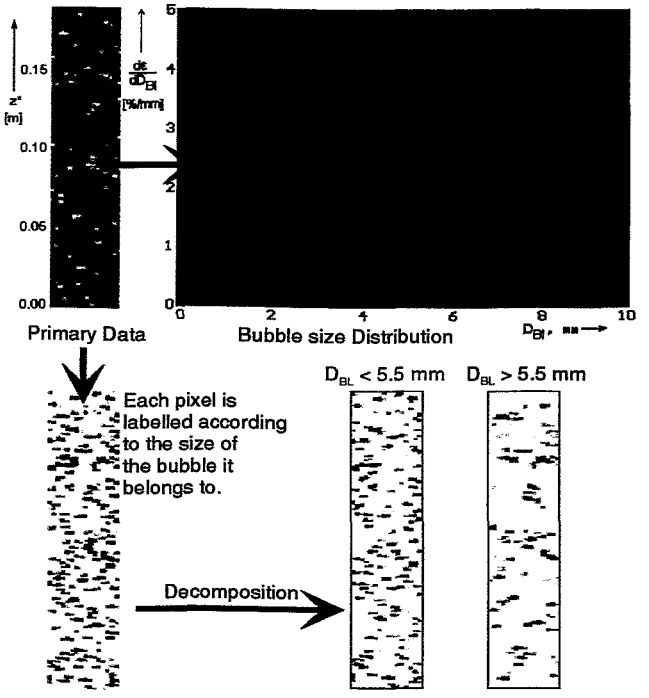

Fig. 9 Decomposition of sequences of instantaneous gas fraction distributions according to bubble size classes

(Flow conditions: J_{Water} = 0.4 m/s, J_{Air} = 0.06 m/s, L/D ≅ 60)

The left column represents a virtual sectional side view of the sequence of gas fraction distributions measured by the sensor. On the right side the bubble size distribution is plotted. The column below the virtual sectional view of the primary data is the result of colouring the bubbles according to their diameter: if the diameter is less than 5.5 mm, they were painted green, in the opposite case red. Now, the initial sequence can be divided in sequences of gas fraction distributions considering only bubbles with $D_{BL} < 5.5$ mm (column with only green bubbles) and $D_{BL} > 5.5$ mm (column with only red bubbles).These decomposed data sets are taken to calculate time averaged gas fraction distributions using eq. (4). Results of this kind are shown in section 5.

5 Bubble flow in a vertical tube

5.1 Experimental mock-up

The sensor was used to study the evolution of the bubble size distribution in a vertical tube of 51.2 mm diameter. A sketch of the test section is shown in Fig. 10. Experiments were carried out with an air-water flow at room temperature.

The superficial velocities were varied in the range of $0 < J_{Air} < 4$ m/s and $0 < J_{Water} < 12$ m/s. The distance between sensor and air injection was varied from 0.03 m to 3.5 m. This corresponds to related inlet lengths of $0.6 \leq L/D \leq 70$.

Three different types of air injecting devices were used: (A) an array of 19 capillaries of 0.8 mm inner diameter, the ends of which were bent into the flow direction and equally distributed over the cross section, (B) 36 orifices in the tube side wall with 1 mm inner diameter and (C) 8 orifices in the side wall of 4 mm diameter.

5.2 Evolution of the flow pattern in case of a bubble-slug transition

An example of the results obtained with the large (4 mm) orifices is presented in Fig. 11. The superficial velocities of water and air corresponded to the region of slug flow. Virtual sectional views of the flow were constructed by extracting sequences of instantaneous gas fraction distributions over the diameter from the measuring cross section. These distributions were plotted in a stack of horizontal bars, beginning from the top of the image and moving downwards with increasing time. Using the known fluid velocity, the vertical axis was transformed from a time axis into a virtual height axis (z*). In the constructed image, the relation between width and height of the resulting column is kept equal to the relation between real tube diameter and scale of the z* axis.

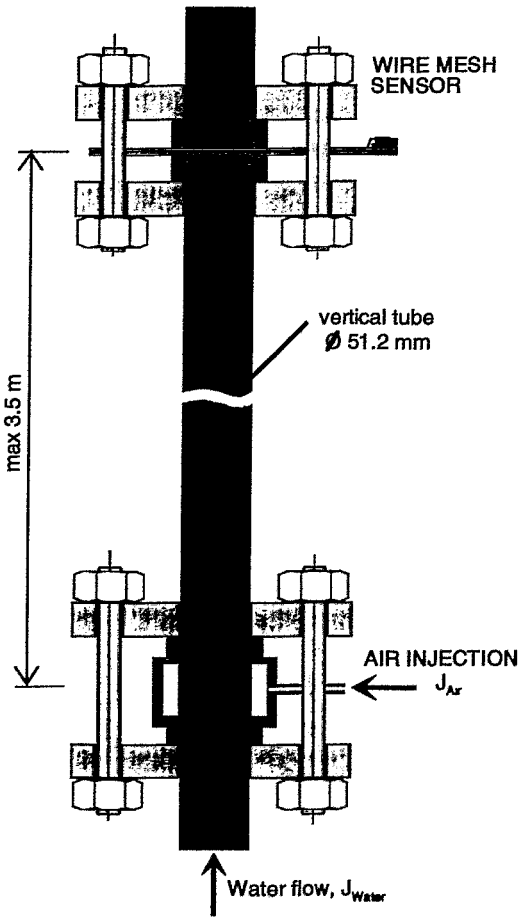

Fig. 10: Vertical test section with air injection and wire-mesh sensor (injection device A)

It is clearly visible that the transient process of slug formation continues over the entire length of the test section. Only at H=3033 mm (L/D ≅ 60) the expected slug flow has fully established. At the air injecting orifices, large bubbles are formed, which are still found close to the wall an a distance of H=30 mm above the injection. With growing distance, both coalescence and fragmentation occur and the bubbles start to move towards the center of the tube. In the end, a slug flow is established.

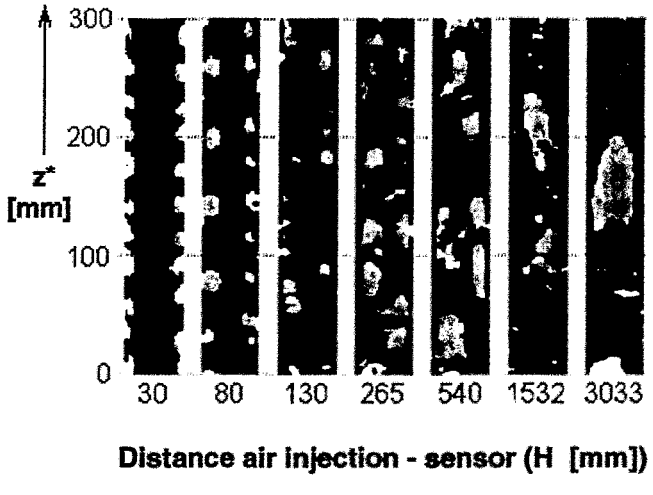

Fig. 11: Evolution of the flow pattern along a vertical tube, (J_{water}=1 m/s, J_{air}=0.5 m/s, H - distance air injection - sensor)

This is very well reflected by the bubble size distributions determined by the described method (Fig. 12). At the distance of 30 mm, an almost monomodal bubble size distribution with a peak at a bubble diameter of approximately 18 mm is found. With growing distance, both coalescence and fragmentation is observed. At H = 540 mm there is a bimodal bubble size distribution for the first time. The further growth of the slug bubbles leads to effective bubble diameters of over 50 mm, i.e. the bubbles take the shape of long plug bubbles at H = 3033 mm. At the same time, fragmentation is also continuing, leading to a growth of the quantity of small bubbles.

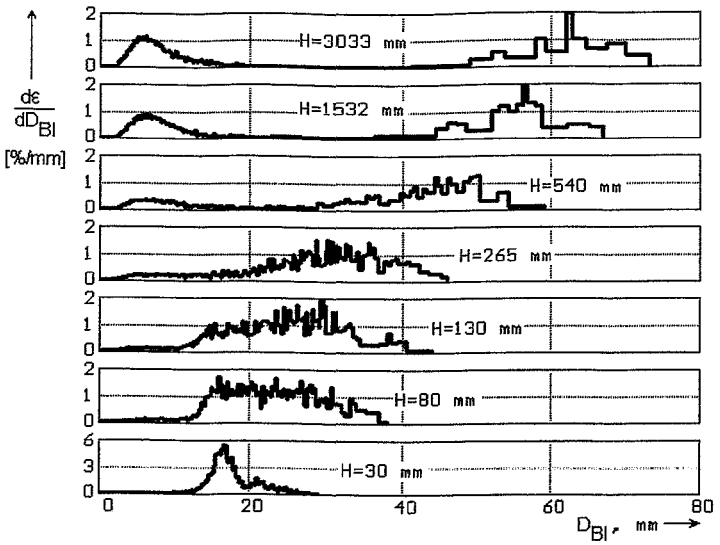

Fig. 12: Evolution of the bubble size distribution for the experiment in Fig. 5

It should be mentioned that the wire-mesh sensor is a very effective instrument to obtain the kind of information presented in Figs. 5 and 6. The measuring period to get one bubble size distribution with the shown quality is only 10 s. The application of needle probes, for example, would cause much more efforts, because longer integration periods and traversing of the probe would be necessary.

5.3 Result of the decomposition of gas fraction profiles according to bubble size classes

The decomposition of radial gas fraction profiles described in section 4.4 was applied to data obtained in an experiment with an air injection through the equally distributed capillaries (injection device A) and a variation of the inlet length from L/D ≅ 0.6 (H = 30 mm) to L/D ≅ 60 (H = 3133 mm). At the combination of superficial velocities of J_{Water} = 0.4 m/s and J_{Air} = 0.06 m/s, the measured bubble size distribution at H = 30 mm indicates, that all primary bubbles have an equivalent diameter smaller than 0.55 mm (Fig. 13, right side).

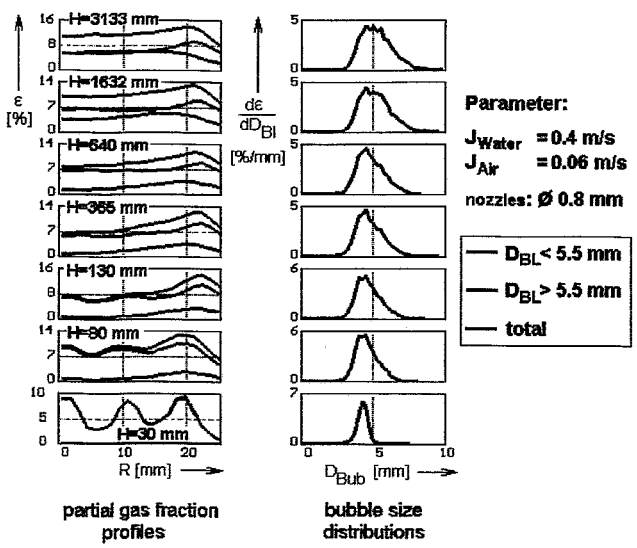

Fig. 13 Evolution of partial gas fraction profiles and bubble size distributions along the pipe

With increasing distance between air injection and sensor, the progressing bubble coalescence leads to the generation of bubbles greater than 5.5 mm.

When we look at the decomposed radial gas fraction profiles, the tendency of the small bubble fraction to move towards the wall is clearly visible. At H = 30 mm, the profile is still strongly determined by the gas fraction maxima found at the places where the capillaries are located. With growing distance, the gas fraction represented by the small bubble fraction shifts towards the wall. The increase of gas fraction near the wall leads to an intensification of coalescence, which leads to a generation of bubbles with $D_{Bl} > 5.5$ mm in this region. These bubbles experience an inverse lift force, pushing them towards the center of the pipe. At H = 3133 mm the equilibrium is nearly established. Here, we observe a pronounced wall peaking of the total gas fraction profile, caused by the peak of the partial gas fraction of the small bubble class. The large bubbles (D>5.5 mm) tend to form a central maximum. The mentioned processes are illustrated in Fig. 14.

A similar experiment at identical superficial velocities was carried out with the injection of air through the injecting device C (8 orifices of 4 mm diameter in the side wall). In this case, the primary bubbles are larger than 5.5 mm. Close above the injection they are found at the periphery of the pipe (Fig. 15), since they have been generated at the wall. With growing distance, a generation of both bubbles smaller than 5.5 mm and larger that 12.5 mm is observed.

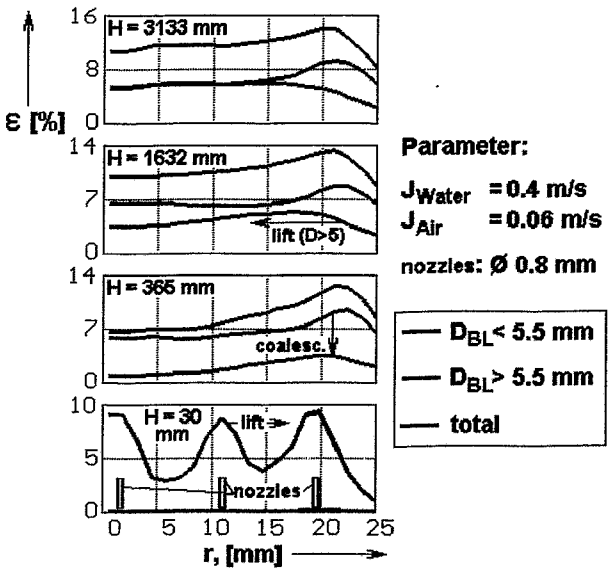

Fig. 14 Effect of coalescence and lift force to the evolution of gas fraction profiles

Since bubbles with a diameter less than 5.5 mm are not generated at the gas injection orifices, they must be the result of fragmentation events. In the same time bubble coalescence leads to the appearance of bubbles larger than 12.5 mm. The bubbles of both classes of large bubbles (5.5 mm ≤ D_{Bl} ≤ 12.5 mm and 12.5 mm ≤ D_{Bl}) are quickly shifted to the center of the pipe. At the end of the test section, the class of small bubbles does not show the expected wall peaking just because the fragmentation process is generating a large number of small bubbles in the center of the pipe, where the gas fractions are high. The more equal distribution of the small bubbles in comparison to the large bubble fractions is a hint to the tendency of the small bubble to move towards the wall.

A bimodal bubble size distribution characteristic for the transition from bubble to slug flow is established at the end of the test section. The inverse lift force transports the large bubbles to the centre of the pipe. The effect of coalescence, fragmentation and lift force is marked in Fig. 16.

It is worth a remark that the flow structure in the two examples shown in Figs. 13 - 16 is not identical at the end of the test section, despite of the identical superficial velocities of gas and liquid. Obviously, an inlet length of L/D ≅ 60 is still not sufficient to establish an equilibrium between bubble fragmentation and coalescence as well as with regard to the lateral movement of the bubbles. The flow pattern is still influenced by the kind of gas injection. We found that at higher superficial gas velocities the inlet length necessary to establish an equilibrium flow structure decreases [7].

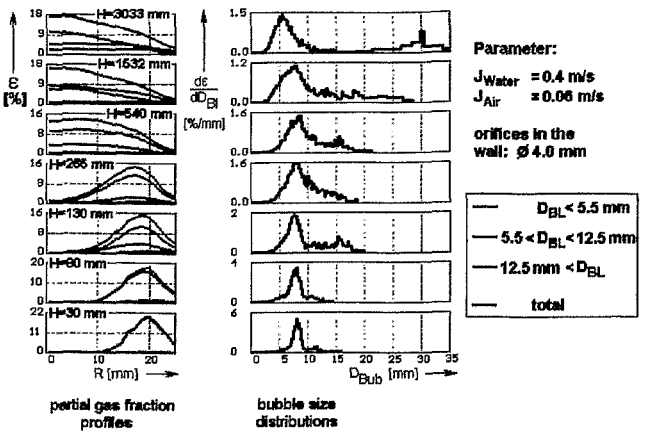

Fig. 15 Evolution of partial gas fraction profiles and bubble size distributions along the pipe, injection device C

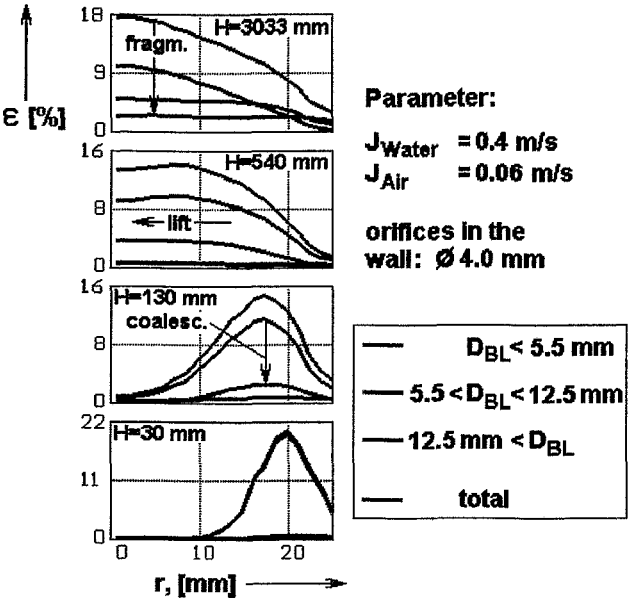

Fig. 16 Illustration of the main effects determining the evolution of gas fraction profiles

5.4 Flow pattern visualisation at high water and gas velocities

Up to now, the presented results in this paper were achieved by using the first generation of signal acquisition unit with a measuring rate of 1200 frames per second. The new capability of measuring 10 000 gas fraction distributions per second was recently used to visualise the transition from bubble to annular flow at a liquid velocity of 4 m/s. Fig. 17 illustrates the gained increase in resolution. For this purpose, a measurement taken at 10 000 frames per second was treated in a way that a resolution was reduced to that of the first generation of signal acquisition device. This was done by averaging 8 successive frames at the high resolution to obtain one of the low resolution. The corresponding virtual sectional view is shown on the left side of Fig. 17. In the middle, the same resolution is shown, but with a time axis enhanced to that of the right part of the figure, where the signal is plotted in the maximum available resolution. This kind of signal treatment allows to get a direct visual impression of the achieved increase in resolution.

To study the effect of transition from bubble to annular flow, the vertical test section in Fig, 10 was used. The measurements were carried out with a distance between air injection and sensor of H = 3033 m (L/D ≅ 60). The results of an increase of the superficial air velocity from 1 m/s to 10 m/s at a constant superficial water velocity of J_{Water} = 4 m/s are presented in form of virtual sectional side views in Fig 18.

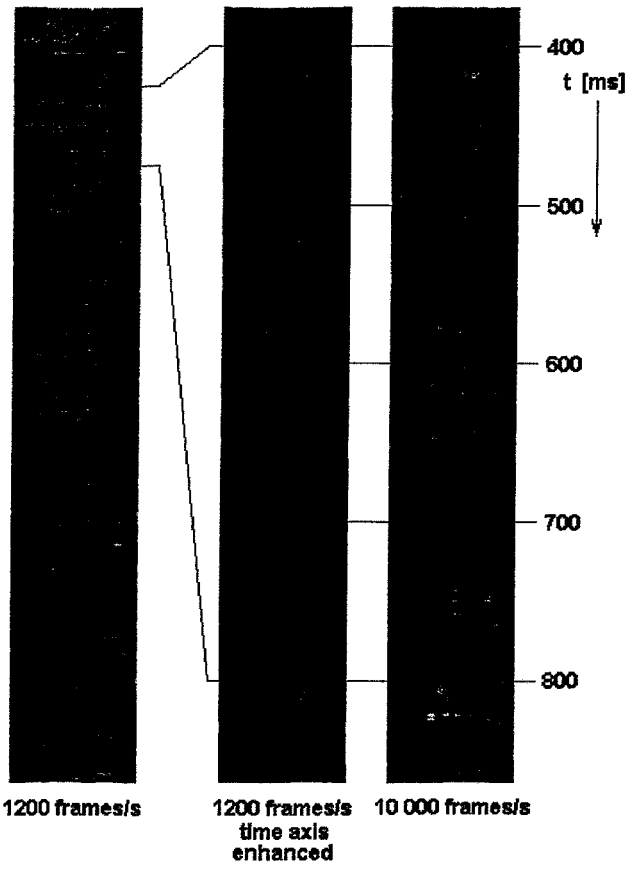

Fig. 17: Virtual side views of a fast slug flow obtained at different measuring rates, resolution increase gained by the 10 000 Hz device

At J_{Air} = 1 m/s the flow regime is still bubble flow. At J_{Air} = 2 m/s the generation of large bubbles due to coalescence is clearly visible. In the range of about 4 m/s superficial air velocity, periodic structures are observed, which remind gas plugs found under slug flow conditions. Compared to plugs at lower water velocities (see Fig. 11, H = 3033 m), these structures are strongly deformed by the action of the turbulent velocity field. When the gas flow rate is further increased to J_{Air} = 10 m/s, the flow pattern becomes really churn-turbulent. In detail, we observed, that the periodic structures dissolve, and an gas path is formed, which oscillates around the axis of the tube. This gas channel is interrupted from time to time by a region of higher water content. If can be stable for periods of about 20 - 50 ms.

According to classical flow maps, all the regimes shown in the Figs. 18 belong to the so-called "churn-turbulent" region. By the help of the high resolution of the wire-mesh sensor, we were able to identify plug-like periodic structures in the transition region between bubble and annular flow.

The air supply of the test facility does not allow a further increase of the air flow rate. In order to further approach the annular flow pattern, the water flow rate was decreased at a constant superficial air velocity of 10 m/s. The result is shown in Fig. 19.

The decrease of the superficial water velocity leads to a continuous extension of the gas channel in the center of the pipe within the cross section as well as in length. At a superficial water velocity of 1 m/s, a wispy-annular flow is observed. The wisps appear with a frequency of approximately 3 Hz, the sections of annular flow between the wisps is therefor approximately 3 m long ("Eulerian" length). On the right side of Fig. 19, the structure of one of such a wisp is shown.

6 Conclusion

The wire-mesh sensor provides detailed information about the structure of the two-phase flow. It is successfully used to visualise the air-water flow in a vertical pipeline. From the primary measuring data it is possible to obtain void fraction profiles as well as bubble size distributions. Experiments were carried out to study the evolution of the flow structure with growing distance from the gas injection. The bubble size distributions clearly show the effect of coalescence and fragmentation.

The decomposition of radial gas fraction profiles according to bubble-size classes allows to study lift force effects. The difference in the behaviour of small and large bubbles in connection with the change in sign of the lift force, which was predicted by Tomiyama [5], was observed by he new measuring method in a realistic multi-disperse two-phase flow.

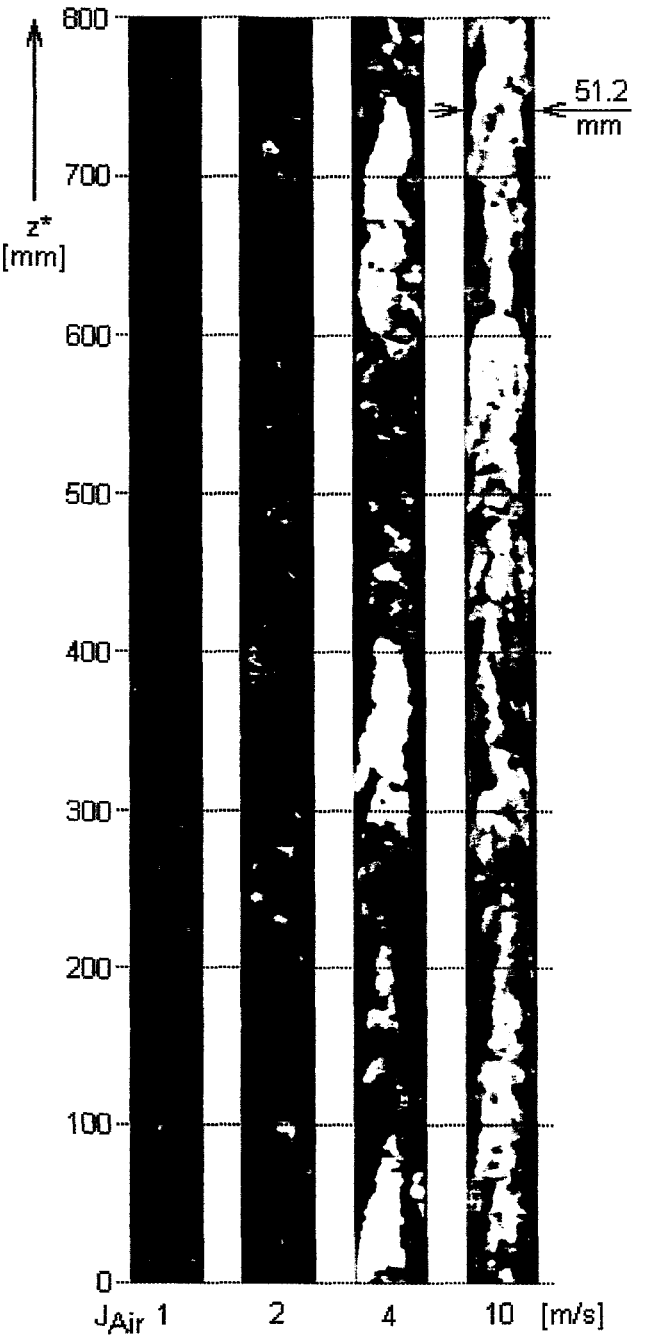

Fig. 18: Virtual sectional views obtained from a vertical air-water flow at J_{Water} = 4 m/s, recorded with the wire-mesh sensor at 10 000 frames per second

The results have furthermore shown, that the coalescence intensity depends from the local gas fraction. In case of the injection of bubbles small enough to be driven towards the wall, the formation of large bubbles starts in the layer close to the pipe wall, where the gas fraction distribution develops the well-known wall peak. The generated large bubbles experience an inverse lift force and are travelling towards

the centre. In case of a high enough gas fraction in the center, there can be a source of small bubbles in the central region, which afterwards start to move in direction towards the wall.

A new generation of wire-mesh sensor signal acquisition unit was applied to visualise the air-water flow in the vertical pipe for the first time. The achieved time resolution of 10 000 frames per second allows unique insights into the flow structure at higher superficial velocities. It was found that even in the region of so-called churn-turbulent flow, the transition from bubble to annular flow covers an intermediate state with periodic structures, similar to gas plugs found in the vertical slug flow. These plugs are strongly deformed by the turbulent velocity field.

7 Nomenclature

sign	unit	denomination
BL	(index)	bubble
D	m	diameter
f_m	Hz	meas. frequency
H	m	height
i,j,k	-	indices
J	m/s	superficial velocity
L	m	length
t	s	time
V	m^3	volume
w	m/s	velocity
x,y,z	m	co-ordinates
Δ	-	difference
ε	1	gas fraction
*	-	virtual

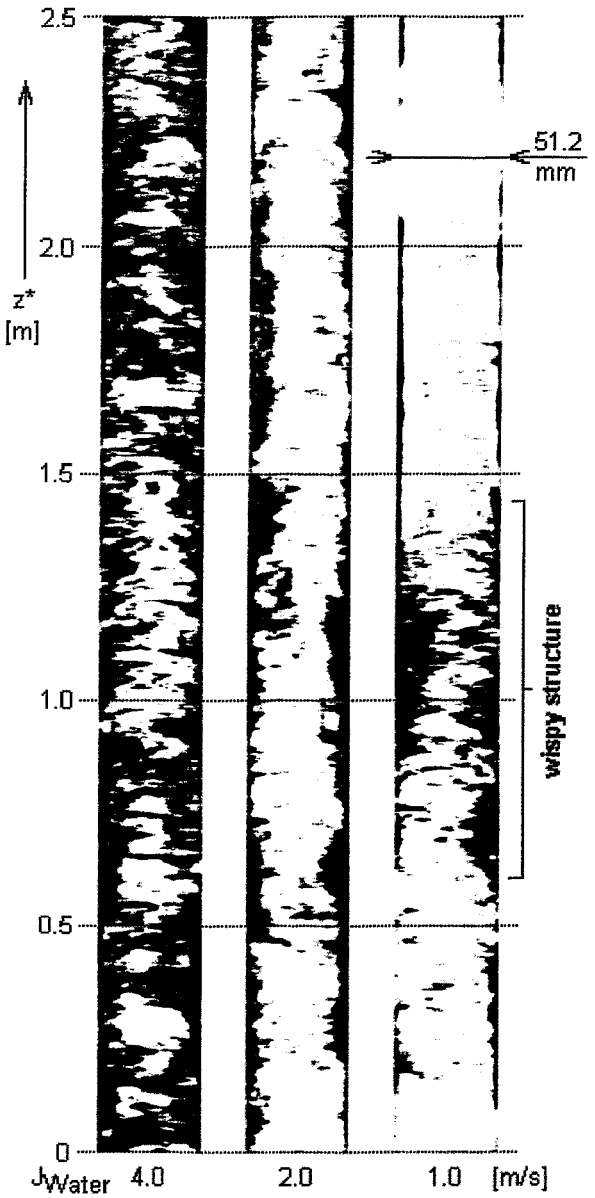

Fig. 19: Transition to a wispy-annular flow by decreasing the superficial water velocity at a constant superficial air velocity of J_{Air} = 10 m/s

8 References

[1] I. D. Johnson: Method and Apparatus for Measuring Water in Crude Oil, United States Patent, No 4,644,263, Date of Patent: Feb. 17, 1987.

[2] N. Reinecke, M. Boddem, G. Petritsch, D. Mewes: Tomographisches Messen der relativen Phasenanteile in zweiphasigen Strömungen fluider Phasen, Chem. Ing. Tech. 68 (1996) 11, S. 1404-1412.

[3] H.-M. Prasser, A. Böttger, J. Zschau (1998), A new electrode-mesh tomograph for gas-liquid flows, Flow Measurement and Instrumentation 9, 111-119

[4] D. Peters, G. Pietzsch, H.-M. Prasser, W. Taubert, M. Trepte, J. Zschau, Wire-Mesh Sensor - now 10,000 Frames per Second, Institute of Safety Research, Annual Report 1999, FZR-284, Feb. 2000, ISSN 1437-322X, pp. 15-18

[5] A. Tomiyama: Struggle with computational bubble dynamics, Third International Conference on Multiphase Flow, ICMF'98, Lyon, France, June 8-12, 1998.

[6] H.-M. Prasser, D. Scholz, C. Zippe: Bubble Size Measurement using Wire-Mesh Sensors, Flow Measurement and Instrumentation (submitted).

[7] H.-M. Prasser, E. Krepper, D. Lucas: Fast wire-mesh sensors for gas-liquid flows and decomposition of gas fraction profiles according to bubble size classes, Second Japanese-European Two-Phase Flow Group Meeting, Tsukuba, Japan, September 25-29, 2000.

VALIDATION OF BUBBLE SIZE MEASUREMENTS WITH WIRE-MESH SENSORS BY HIGH-SPEED VIDEO OBSERVATION

D. Scholz, C. Zippe

Forschungszentrum Rossendorf e.V., P.O.Box 510119, D-01314 Dresden, Germany
e-mail: prasser@fz-rossendorf.de

1 Introduction

In the following presentation, I want to introduce the results, which were obtained by a comparison between values of bubble sizes of the wire-mesh sensor and values obtained by video-observation. The task was an investigation of the accuracy of bubble sizes measured by the wire-mesh sensor. A second task was the determination of the lower limit of bubble sizes, which is resolved by the sensor. For bubbles with a diameter smaller than the distance between the wires of the mesh, this was an important question.

The production of bubbles with a definite volume respectively size is hardly possible. Therefore a direct comparison with the measurement data of sensor is impossible. We decided to use another method for a comparison. It should be based on another measuring technique. We had observed the movement of bubbles with a high-speed video device. The measurement of the sensor and the observation were started simultaneously. So, it was possible to compare both results. An important condition was the use of a transparent test channel.

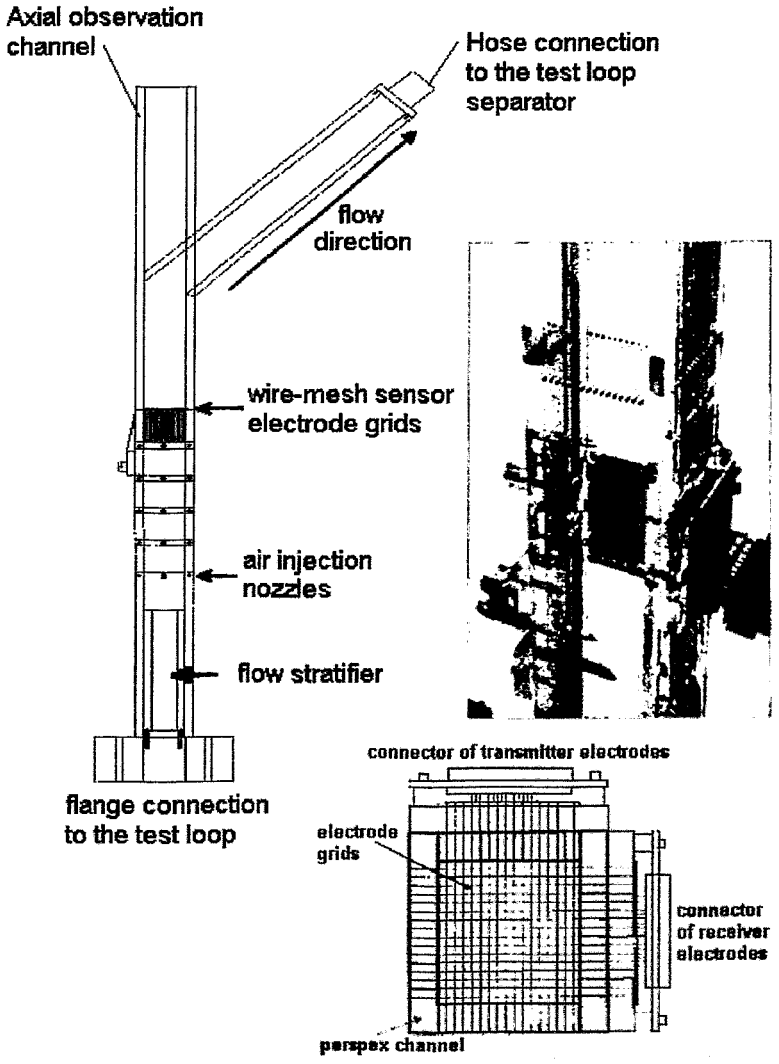

Fig. 1 Perspex channel with wire-mesh sensor

2 Organic glass channel

The electrodes of a wire-mesh sensor were built into a transparent test channel made of organic glass (Fig. 1). This channel has a square cross section with an inner width of 50 mm. The sensor consists of 16 transmitter and 16 receiver electrodes each. The pitch between the individual electrodes is 3.125 mm. The gap between the electrode planes is 1.5 mm. One end of each electrode is going through the channel wall and connected with a plug connector outside.

The wire-mesh sensor was operated with a measuring frequency of 1000 Hz (frames per second). All experiments were performed under identical environmental conditions. For this purpose the test channel was mounted on the two-phase flow test-loop (MTLoop) of the institute. For the experiments, water flows with liquid velocities between 0.05 and 0.8 m/s were produced in the loop. Air bubbles were generated using different injection nozzles. For the investigation it was very important to generate bubbles rising separately in the liquid flow. Three different nozzles were installed one after the other in an orifice below the sensor. The local pressurised air net was used for the air supply. The flow was adjusted to a gas velocity of 0.005 m/s.

3 Test set-up

The test set-up consisted of the wire-mesh sensor and a high-speed video device. With this set up the transition of bubbles through the sensor electrodes was observed. The digital video recorder worked with a speed of 1000 frames per second. This is the same frequency like the measuring frequency of the sensor. The important

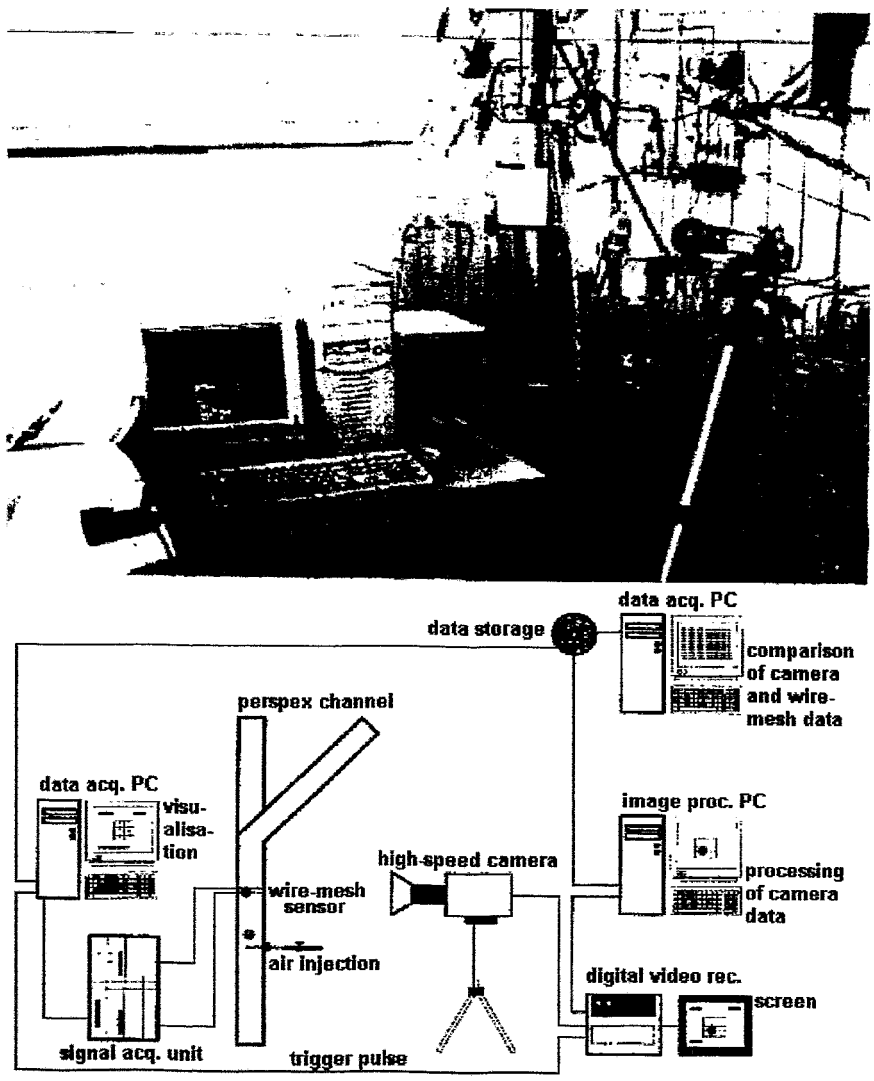

Fig. 2 View of the test channel at the two-phase flow test loop

components are shown in Fig. 2. Apart from sensor and camera, computers for the analysis belong to the set-up.

Wire-mesh sensor and the video device were started simultaneous. That was realised by a trigger signal, which was generated when the start button on the data acquisition computer of the wire-mesh sensor was pressed. The video device was started by this trigger signal. All data of measurement and observation were analysed by a external computer.

Very important is the accurate alignment of the high-speed camera. In the captured frame, just the sensor and his immediate environment should be visible. The width of a frame should be equal to the inner width of the channel. The camera was adjusted in a way that the orientation of the pixel lines was accurately in the horizontal direction of the measuring plane. This were important conditions for a optimum analysis. A video sequence consists altogether of 8738 separate frames of 256 x 240 pixels.

4 Evaluation of camera frames

The main problem was to calculate the volume size respectively the bubble size from the two dimensional view obtained by the camera. For this we used a procedure, which is introduced in Fig 3.

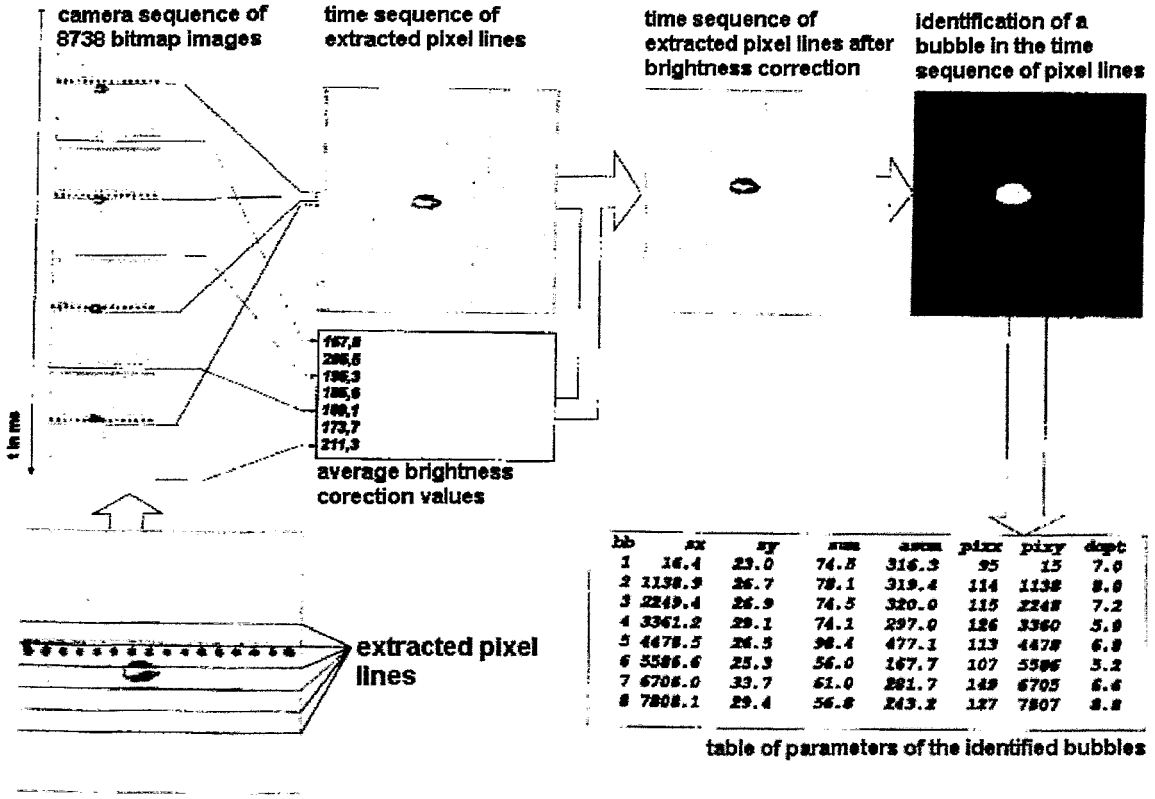

Fig. 3 Extraction of Eulerian sectional side views from camera sequences and optical bubble recognising method

The frames of a video sequence were saved as bitmap files. Every file consists of 256 x 240 picture elements (pixels). A frame corresponds to a time range of 1 ms, which is given by the recording speed of 1000 frames per second. Lines of pixels are taken out of every frame of a sequence from an identical selected axial position. All these lines are merged to create a new bitmap file, where the lines are stacked on top of each other, forming a new image of as many lines as individual frames are in the time sequence. The algorithm starts with the pixel line from the first frame on top of the new image, the successive lines are put in the order from the top to the bottom. This new file has altogether 8738 lines now. It represent a Eulerian pseudo-side view of the flow, where the vertical axis is a time axis. This kind of operation was performed for six different axial positions in the original camera frames: the line exactly located in the gap between the electrode grids, four lines below the measuring plane at different distances and one line above the measuring plane.

The projections extracted in this way were used to determine bubble sizes. For the comparison with the bubble size measured by the wire-mesh sensor the first line below (upstream) the sensors was used. In this place, the bubbles still have their undisturbed shape. The image is processed to correct the 100 Hz oscillations of the illuminating lamps. In the next step, a threshold was applied to binarize the bubble shape. By the help of a recursive fill algorithm, inner pixels, which were not recognised as air due to optical reflections were assigned to the gas phase domain. In the last step, the bubble volume was assessed assuming a rotational symmetry (Fig. 4). The diameter was calculated by taking the cubic root of the volume. These data about size and the position of the bubbles in the flow are stored in a table. The values in the table will be used for the comparison with the values from wire-mesh sensor.

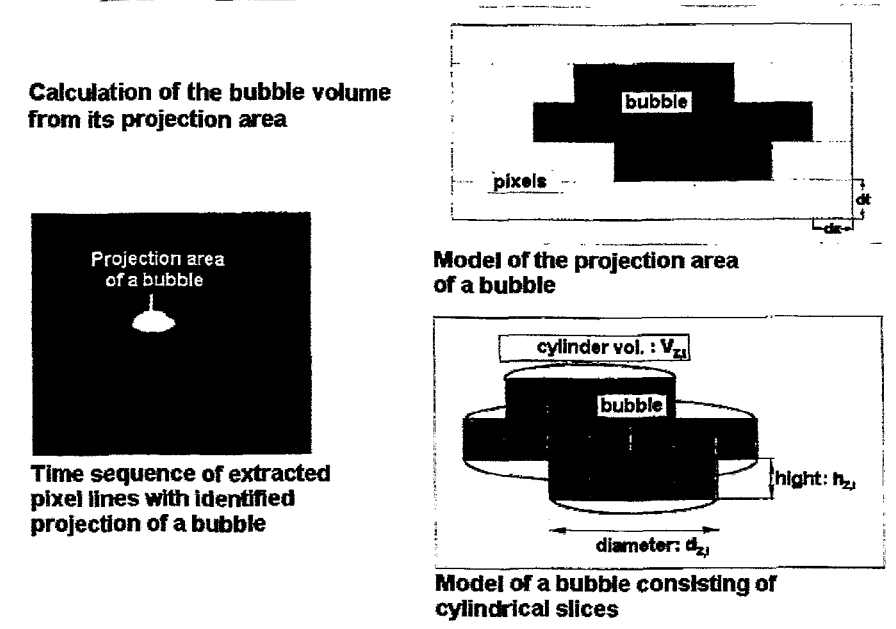

Fig. 4 Optical bubble size estimation

The presence of rotational symmetry was assumed for each horizontal layer of the bubble of the thickness of one pixel (Fig. 4). The visible surface of bubble in the projection consists of a certain number of lines with a certain number of pixels identified to belong to the bubble. Each horizontal line of pixels of the bubble image was treated as the side view of a cylinder. The cylinder diameter can be calculated from the number of pixels and the cylinder height (in units of time) is known, because a line correspond with a time range of one millisecond. So, the cyl-

inder volume will be calculated by adding the results for each line occupied by the bubble.

The visible surface in the projection does not represent the real appearance of the bubble, because the vertical axis is a time axis. The volume is therefore related to the bubble velocity and measured in units of $m^2 \cdot s$, the diameter in units of $(m^2 \cdot s)^{1/3}$. This is not a disadvantage, since the wire-mesh sensor can deliver real volumes only if the bubble velocity is known. Therefore it is better to compare related volumens respectively related diameters. In this case, the additional measuring error caused by the uncertainty of any velocity information is excluded.

Table of bubble parameters obtaind by the wire-mesh sensor

im	jm	km	mi	mj	mk	mr	max	v	r	n	deps
2266.8	28.5	28.3	10.1	4.6	3.3	8.2	81	370	4.45	481	0.0016916
4495.7	29.3	19.5	8.3	3.8	3.3	6.9	75	293	4.12	362	0.0013434
6723.0	22.4	24.9	7.7	4.6	3.5	6.8	74	306	4.18	379	0.0014010
31.2	32.3	25.5	8.7	3.3	4.2	7.2	70	288	4.10	379	0.0013192
3378.5	27.6	24.5	6.6	3.7	3.6	6.0	68	255	3.64	270	0.0009222
5604.7	32.7	24.8	9.6	3.3	4.5	7.8	68	351	4.38	432	0.0016062
1154.6	29.6	26.0	8.8	3.5	3.6	7.2	65	283	4.07	357	0.0012937
7825.0	26.1	20.3	7.7	4.1	3.7	6.7	65	324	4.26	377	0.0014851

Table of bubble parameters obtained from the camera sequences

bb	sx	sy	sum	asum	pixx	pixy	dopt
1	16.4	23.0	74.5	316.3	95	15	7.0
2	1138.9	26.7	78.1	319.4	114	1138	8.0
3	2249.4	26.9	74.5	320.0	115	2248	7.2
4	3361.2	29.1	74.1	297.0	126	3360	5.0
5	4478.5	26.5	98.4	477.1	113	4478	6.8
6	5586.6	25.3	56.0	167.7	107	5586	5.2
7	6706.0	33.7	61.0	281.7	149	6705	6.6
8	7808.1	29.4	56.8	243.2	127	7807	8.8

Table of parameters of corresponding bubbles from both wire-mesh sensor and camera

ds	max	sx	sz	dx	d1	d2	d3	d4	d5
8.9	81	121	2266	8.3	10.2	8.5	8.1	8.2	8.3
8.2	75	115	4494	9.0	9.5	9.7	9.7	9.5	9.9
8.4	74	149	6720	7.8	9.8	8.2	7.7	7.8	8.1
8.2	70	99	31	8.2	8.0	8.5	8.1	9.8	8.9
7.9	68	123	3376	7.6	9.3	8.3	8.2	8.0	8.1
8.8	68	98	5603	8.3	8.1	6.8	8.3	8.1	7.9
8.1	65	112	1154	8.4	8.8	8.5	9.8	9.8	8.9
8.5	65	131	7823	7.1	10.5	7.7	7.4	7.9	9.2

Fig. 5 Comparison between wire-mesh and camera data

5 Comparison of data

The bubble sizes measurement with the wire-mesh sensor was carried out according to the method described in [1]. The sizes and the positions of the bubbles, which were determined by wire-mesh sensor, were saved in a similar table like the data from video observations. Related volumes and respectively related diameters were calculated to make it unnecessary to measure the bubble velocity. The data from the table of camera data and the table of the wire-mesh sensor data were merged by selecting the lines that belong to identical bubbles and putting them into a new table in one line (Fig. 5). This table contains the optically obtained related diameter and the related diameter measured by the wire-mesh sensor of one and the same bubble in one line. These points can be plotted in a co-ordinate system for the two mentioned values (Fig. 6). The different experimental conditions for the points shown in Fig. 6 are summarised in Fig. 7. In this table all fifteen measurements are listed. The experiments were carried out with the three different air nozzles and different liquid velocities ranging from 0.05 to 0.8 m/s. The presence of a code number indicated the availability of the given combination of velocity and injection capillary. The code itself was used as file name and contains the date of the measurement and a successive number.

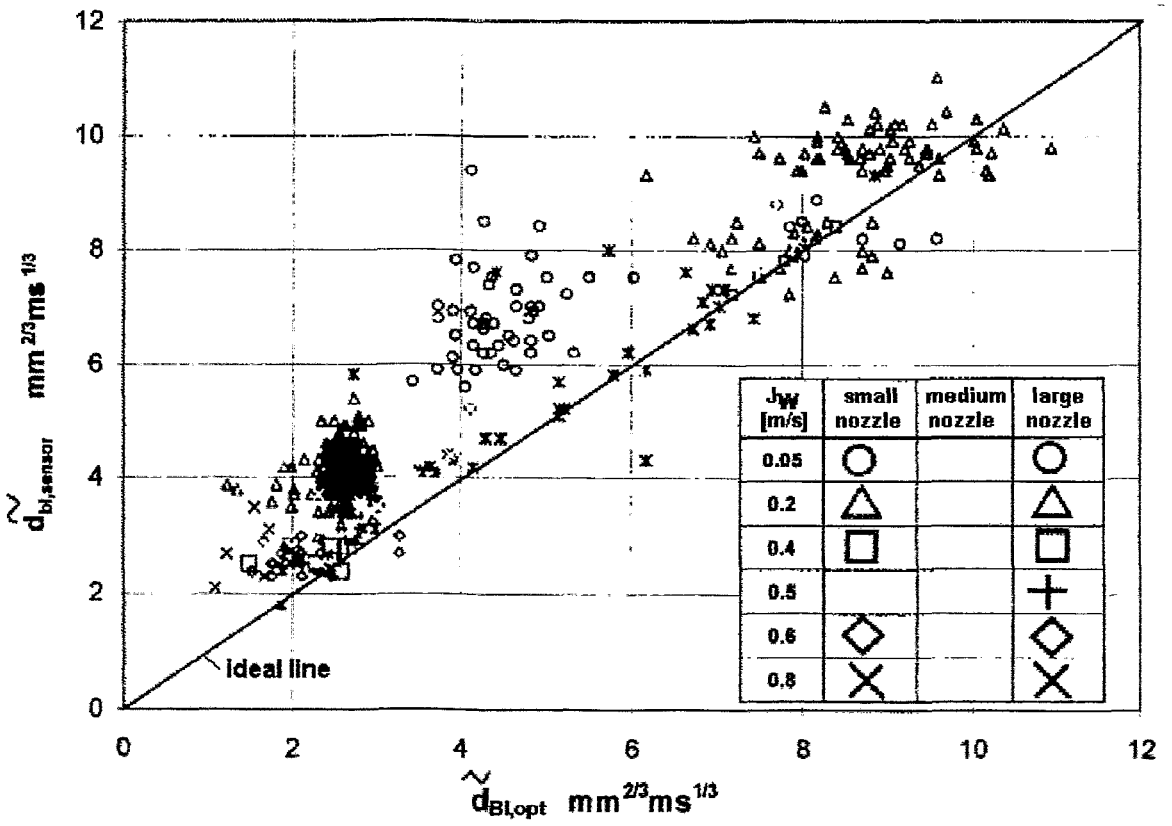

Fig. 6 Comparison of related bubble diameters

As shown in Fig. 6, the agreement between the two methods is satisfying. There is a tendency to overestimate the bubble size by the wire-mesh sensor for low diameters and low liquid velocities. This may be caused by the finite axial extension of the measuring plane of the wire-mesh sensor, which is 1.5 mm high. This leads to the

effect, that each bubble is virtually prolonged in axial direction by a contribution of this order of magnitude. The relative effect of this systematic error is increasing with decreasing bubble size, so that the agreement is better for bigger bubbles.

Flow velocity of water [m/s]	small nozzle	medium nozzle	large nozzle
0,05	19060004	19060001	16060001
0,11			16050001
0,20	19060005	19060002	15060001/16060003
0,33			17050001
0,40	22060003	19060003	16060002
0,50			22060002
0,60	20060001	20060003	22060001
0,67			17050002
0,80	20060002	20060004	

code numbers indicate realised measurements (file names)

Flow velocity of water [m/s]	small nozzle
0,05	13070001
0,40	13070002
0,60	13070003

Measurements carried out with enlarged camera view field (macro zoom)

Fig. 7 Summary of conducted experiments at the transparent test channel

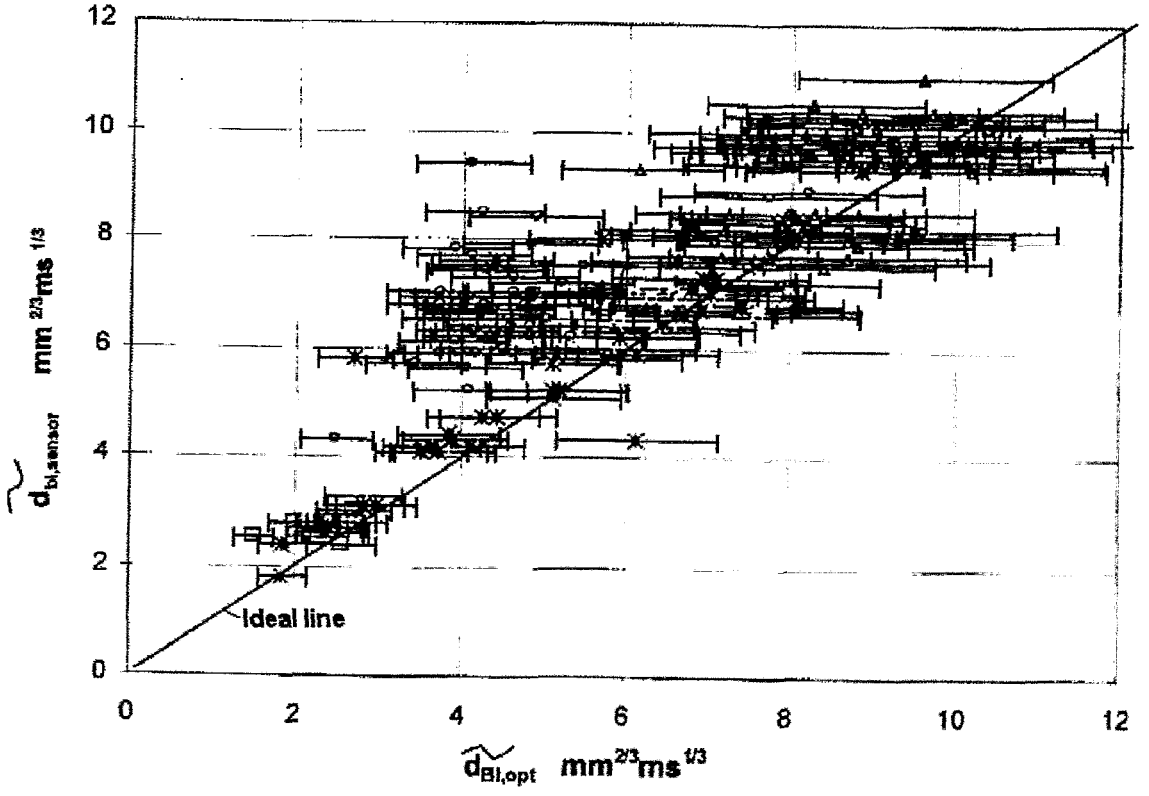

Fig. 8 Assessment of the measuring error of the optical bubble size determination

6 Estimated error

An important question is the assessment of the measuring accuracy of the optical bubble size measurement. A investigation had shown that the influence of this error was high. Therefore the error sources were searched. We found four mainly sources: The largest error contribution is caused by the fluctuation of bubble shape. In reality, the bubbles do not have a rotational symmetry. Their horizontal extension can change depending on the view direction. Other errors arise due to the parallaxes and due to the discretization of the camera frames. The total relative error of the related bubble diameter obtained by the optical method was found to be about 19%. Corresponding error bars are introduced in Fig. 8. Together with the error bars most of the measuring points include the ideal line.

7 Resolving capability of the wire-mesh sensor

A other task was the determination of the lower limit of bubble sizes, which is just resolved by the wire-mesh sensor. It was found, that the relative position of the centre of a bubble in the grid of crossing sensor wires has an influence on the appearance of the bubble in the sensor signal. In general, the relative position of the bubble centre related to the cross points of the wires is arbitrarily changing. In a turbulent two-phase flow an equal statistical distribution

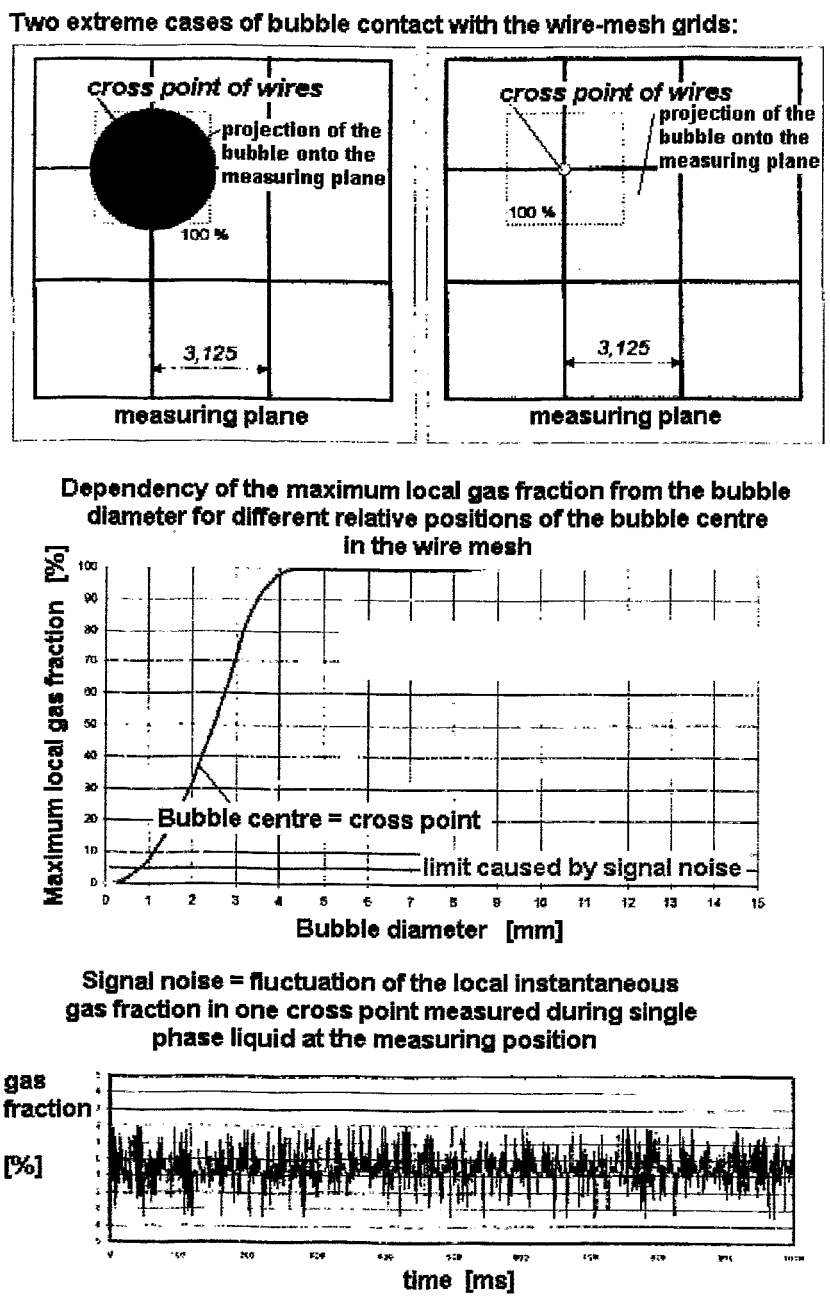

Fig. 9 Model to assess the bubble size resolution limits of the wire-mesh sensor

of the location of the bubble centre can be assumed. If the bubble passes the sensor plane in a way that the centre of the bubble is corresponding to the centre of one mesh (Fig. 9, right side), then the maximum observed local instantaneous gas fraction during the bubble passage is on minimum for a given bubble size, when the centre is located at the cross point of two wires (Fig. 9, left side), then the maximum observed local instantaneous gas fraction is on maximum.

From simple geometrical considerations it can be concluded, that the diameter of the bubble must be greater than the double length of the diagonal of one electrode mesh to ensure that the mesh can be covered by the bubble completely. Bubbles greater than this diameter should always show maximum local instantaneous gas fractions of up to 100 %. If the bubble diameter is equal to one length of the diagonal, it can still produce instantaneous local gas fraction values, but only if it passes through the measuring plane exactly in a way, that the bubble centre goes through the cross point of two wires. This is reflected by the yellow and the blue curves in the lower part of Fig. 9, where theoretical maximum values are presented. They were calculated under the assumption that the maximum of the local instantaneous gas fraction is approximately equal to the shading of the most affected square control volume by the bubble, i.e. the visible surface of the bubble and the sensitive volume by a view from above were put in proportions. The result values were plotted in a diagram, in which the maximum local instantaneous gas fraction is plotted against the real bubble diameter.

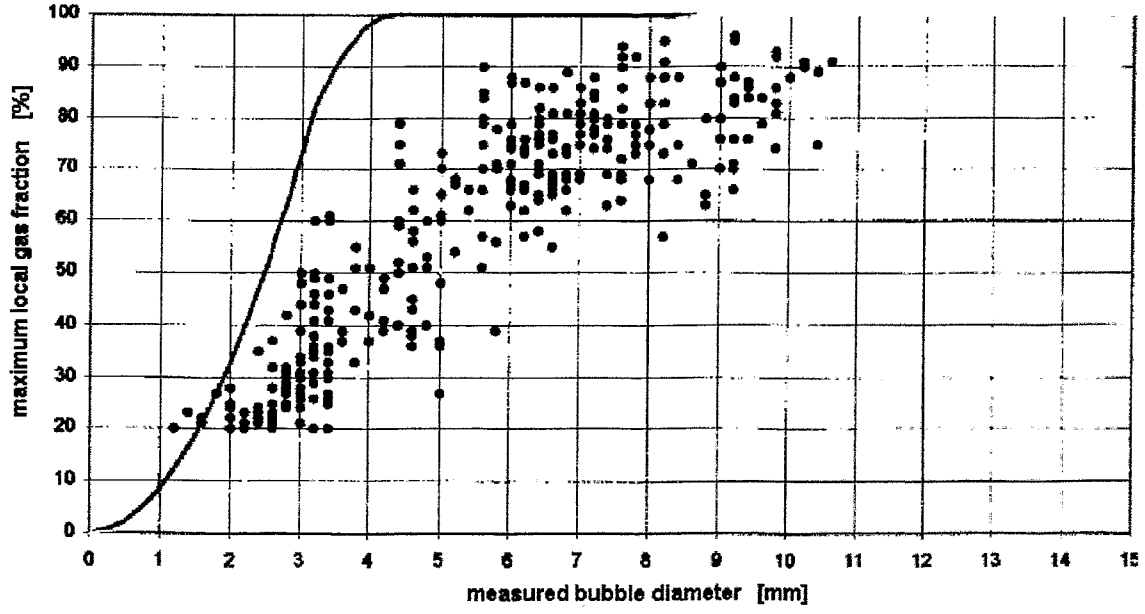

Fig. 10 Measured maximal gas fractions inside of bubbles depending on their diameter

For all fifteen experiments listed in Fig. 7, points characterising the maximum of the local instantaneous gas fraction observed within a bubble and the corresponding measured bubble diameter were put into the diagram developed in Fig. 9 for all registered bubbles. The bubble diameters were determined likewise from the video frames. The result is shown in Fig. 10. We can see, that small bubbles with a di-

ameter smaller than the range of electrodes, are situated between the blue and yellow limits. This means that the simple geometric assumptions leading to the yellow and blue limits are confirmed. If we now consider the noise level of the raw signal, which was found to be around 7 % in the given experimental set-up, then the diameter of the smallest bubble which can still be detected with a probability of 100 % can be found at the point, where the maximum gas fraction for the yellow curve becomes less than the noise level, which is the case for bubbles less than approximately 1.5 mm. Bubbles with diameters less than this value can still be detected if they are greater than about 1 mm, but the probability to detect them is no more 100 %. Smaller bubbles cannot be resolved at all. To increase resolution, the noise level must be decreased, which can be managed to a certain extend by better electrical screening.

Further we can see, that gas fractions of 100 % were not reached in the experiments. This is caused by so-called water bridges, which developed due to the fragmentation and deformation of the bubbles at the sensor wires.

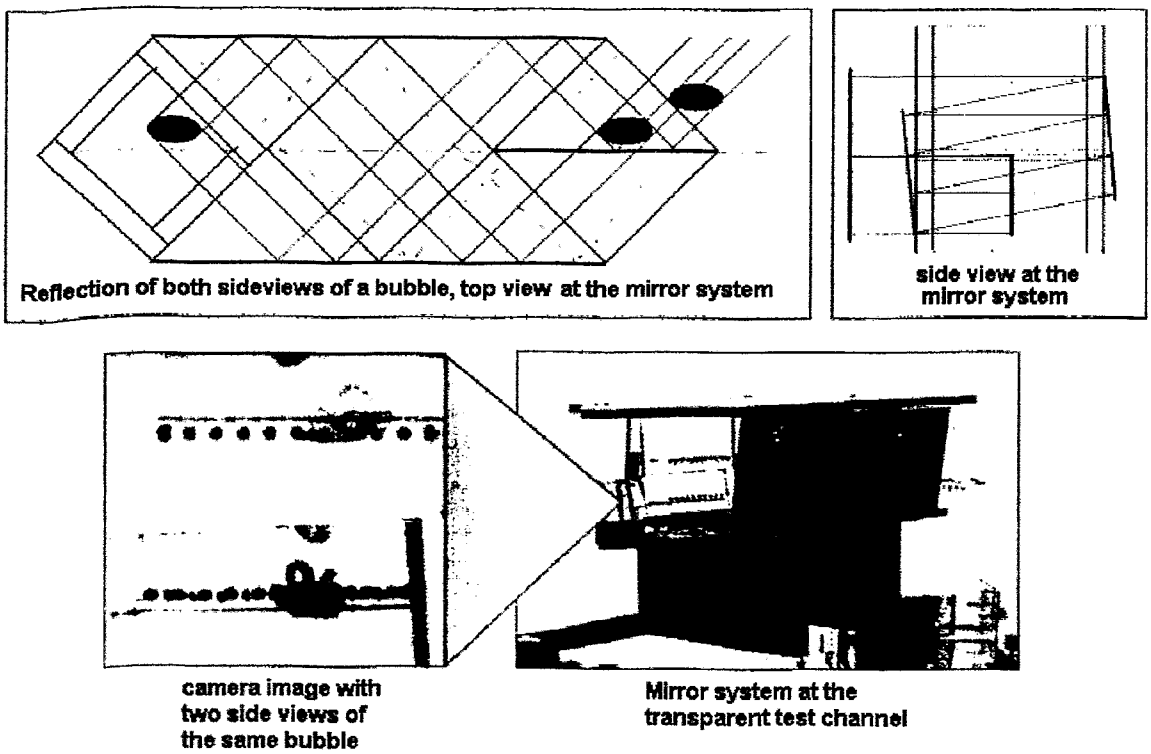

Fig. 11 Mirror system for stereoscopic video observations of bubbles in the wire-mesh sensor

8 Mirror optic for stereoscopic observations

The measuring error of the optical bubble size measurement can be decreased by observing the bubble from two perpendicular directions. For this purpose, a stereoscopic visualisation system was developed (Fig. 11). It consists of a mirror assembly that produces a compound image consisting of an upper part showing the test channel from one direction and a lower part, showing it from the other direction. In this

way, the horizontal resolution of the digital video system can be optimally utilised. Preliminary tests have shown, that the mirror optic is functioning, but has still some deficiencies. In the next time it will be redesigned and afterwards used for new experiments.

9 Conclusions

The investigations have shown that the determination of bubble sizes with the wire-mesh sensor is possible. It is also possible to determine the bubble size of bubbles with diameters smaller than the pitch of the sensor electrodes. The smallest detectable bubble diameter depends on the signal noise level. In the experiments carried out the lowest resolved bubble diameter was around 1.6 mm.

The error of image analysis amounts to approximately 19 %. Therefore, this error has a big influence to the result of the comparison. The goal was set to improve the image processing by using a stereoscopic visualisation of flow.

10 Literature

[1] H.-M.Prasser: Messung von Blasengrössenverteilungen mit Gittersensoren, Workshop „Messtechnik für stationäre und transiente Mehrphasenströmungen", 24.-25.September 1998 in Rossendorf, FZR-241, November 1998, S. 157-164.

[2] H.-M. Prasser, A.Böttger, J.Zschau: A new electrode-mesh tomograph for gas-liquid flows, Flow Measurement and Instrumentation 9, 1998, S.111-119.

[3] H.-M.Prasser: Leitfähigkeitssensoren für die Bestimmung von Parametern in einer Zweiphasenströmung, Workshop „Messtechnik für stationäre und transiente Mehrphasenströmungen", 6.-7. November 1997 in Rossendorf, FZR-204, Dezember 1997, S. 64-71.

[4] D. Scholz: Bewertung der Genauigkeit eines Gittersensors zur Visualisierung einer Zweiphasenströmung durch Vergleich mit optischen Hochgeschwindigkeitsaufnahmen, Diplomarbeit, Rossendorf, September 2000.

Low-pressure dynamics of a natural-circulation two-phase flow loop

A. Manera[1], H. Hartmann[2], W.J.M. de Kruijf[1]
T.H.J.J. van der Hagen[1-2], R.F. Mudde[2]

[1]Interfaculty Reactor Institute, Delft University of Technology, The Netherlands
[2]Kramers Laboratorium voor Fysische Technologie, Delft University of Technology, The Netherlands
E-mail: a.manera@iri.tudelft.nl

Abstract
Flashing induced oscillations in a natural circulation loop are studied as function of heating power and inlet subcooling in symmetrical and asymmetrical power conditions. To unveil the effects of power/velocity asymmetries on the two-phase flow stability at low power and low pressure conditions different signals at several locations in the loop are recorded. In particular a Laser Doppler Anemometry set-up is used to measure the velocity simultaneously in two parallel channels and a wire-mesh sensor is used to measure the 2D void fraction distribution in a section of the ascendant part of the loop.

Introduction

Natural circulation is of importance for several industrial applications such as steam generators, boilers and chemical industrial processes. Passive cooling by means of natural circulation has been recently considered as a challenging principle to be applied to next generation Boiling Water Reactors (BWRs) in order to simplify these systems and improve at the same time their inherent safety. A long adiabatic section is built at the top of the heated section (core) to enhance the buoyancy of the loop and achieve high flow rates. Unfortunately, the presence of a long adiabatic section (riser) makes the system susceptible to so-called flashing-induced instabilities. Flashing-induced instabilities in a natural circulation system occur as soon as the heating power is sufficient to bring the coolant at the exit of the heated section at a temperature equal or larger than the corresponding saturation temperature at the exit of the riser. In fact, at low-pressure conditions the saturation temperatures corresponding to the core exit pressure and to the riser exit pressure respectively can differ by several degrees. Therefore, even if no boiling occurs in the core, void production can take place in the adiabatic section due to a decrease of the local pressure along the axis of the system.

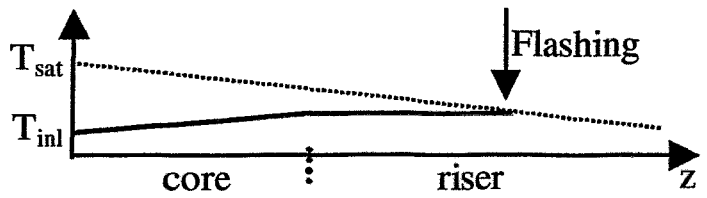

Fig. 1 Flashing in the riser at low power and low pressure conditions

This process is schematically illustrated in Fig. 1: at low pressure the local saturation temperature decreases considerably along the vertical axis of the system, from the inlet of the heated region to the end of the adiabatic section. If the power is low, the coolant that enters the heated section with a given temperature T_{inl} can still be in

subcooled conditions at the exit of the heated section (core), but it can attain saturation conditions in the adiabatic section giving rise to void production due to flashing. The rapid void production due to flashing leads to a sudden imbalance between the coolant density in the downcomer and core/riser sections causing an abrupt increase of the mass flow rate. As a consequence of the increased mass flow rate, the temperature at the outlet of the core will decrease to a value too low to allow flashing in the riser. The buoyancy of the loop will decrease due to the suppression of void production in the riser; consequently the fluid temperature at the core exit will again increase leading again to flashing in the riser. This process can become self-sustained resulting in constant amplitude flow oscillations.
During flashing-induced instabilities the quality at the exit of the core is generally negative (subcooled conditions) or very close to zero and the instability process is directly correlated to the oscillations of the hydrostatic pressure head in the ascendant part of the loop.

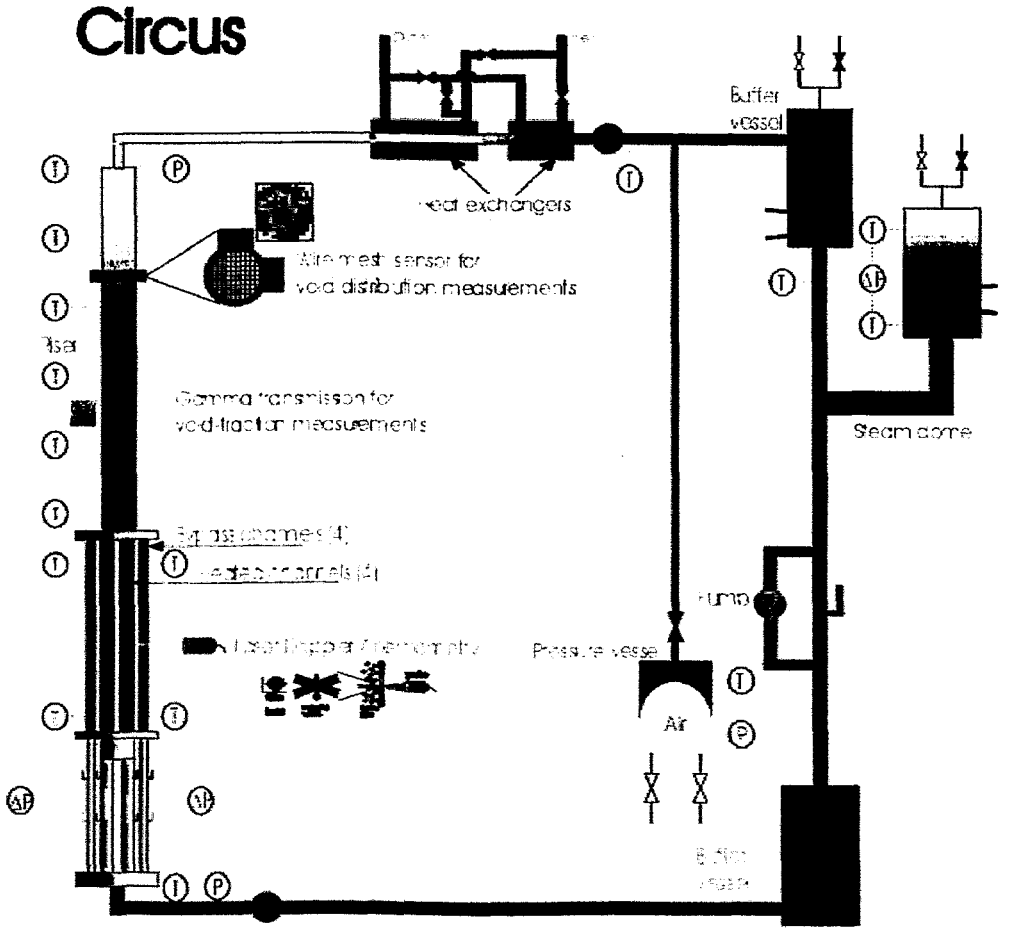

Fig. 2 Schematic view of the CIRCUS facility

To avoid or reduce the effects of flashing during the start-up of a natural circulation BWR suitable procedures need to be defined. In order to gain more physical insight into the phenomena involved during flashing oscillations and to enlarge the experimental database needed to validate analytical models and advanced

thermalhydraulic codes the CIRCUS facility has been built at the Delft University of Technology[1]. A schematic view of the facility is represented in Fig. 2. The facility consists of four parallel separately heated channels and four parallel non-heated bypass channels above which a long adiabatic section (riser) is present. The steam produced in the system is condensed in a heat exchanger. The pressure of the system is regulated by means of a steam dome (see Fig. 2) where a two-phase mixture is kept in equilibrium at saturation conditions. The facility is equipped with several thermocouples, flowmeters, pressure and pressure-drop sensors. Two laser doppler anemometry set-ups are used to measure the local velocity in two parallel channels simultaneously (data rate between 1000 and 5000 Hz) and a wire mesh sensor[2] located in the riser is used to measure the 2D void fraction distribution on a 16x16 grid with a frequency of about 1000 Hz.

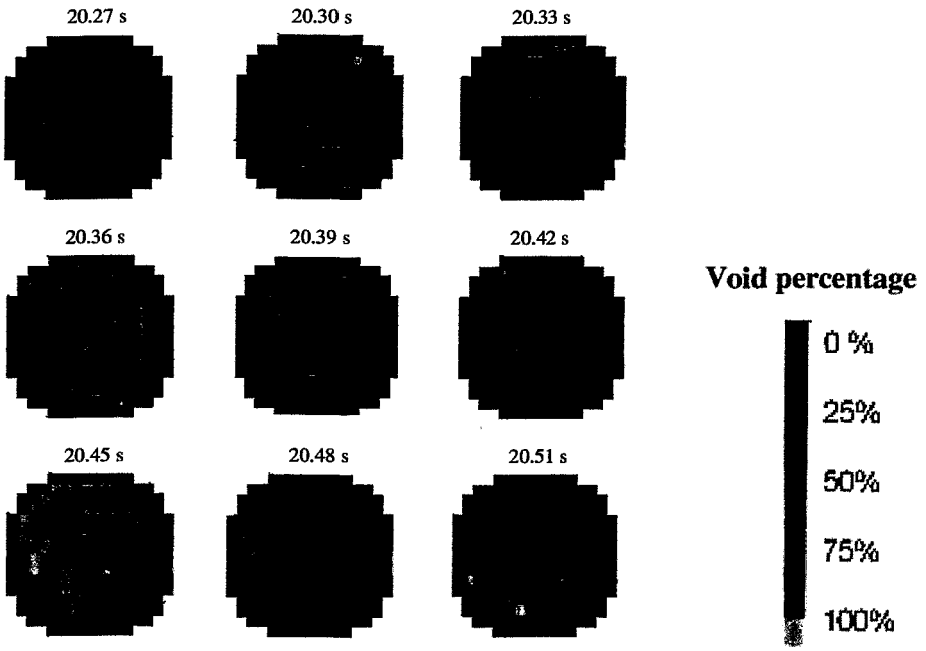

Fig. 3 Void fraction distribution measured by the wire mesh located in the riser

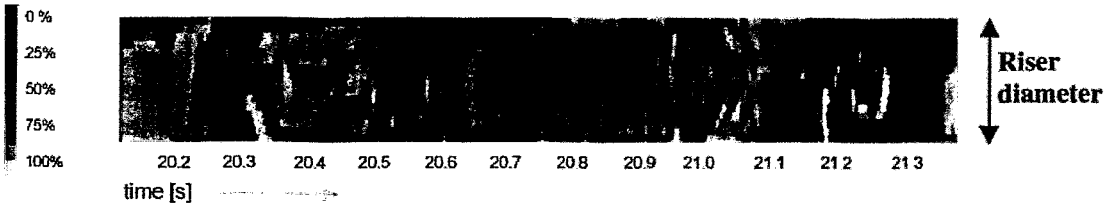

Fig. 4 Void fraction projection on time axis

In Fig. 3 a measurement of the void fraction during a flashing-induced instability performed with the wire mesh sensor located at the top of the riser is shown at different time instants. A graphical reconstruction of the average radial void fraction in the section where the wire mesh is located is shown as function of time in Fig. 4. From Fig. 3 and Fig. 4 it can be seen how rapidly the void distribution changes during flashing. Fast alternation of liquid and steam is in fact observed, giving rise to strong

void fraction fluctuations. This is also shown in Fig. 5, where the time series of the average void fraction in the riser section as measured by the wire-mesh is reported. The periodic character of the flashing instabilities is clearly visible.

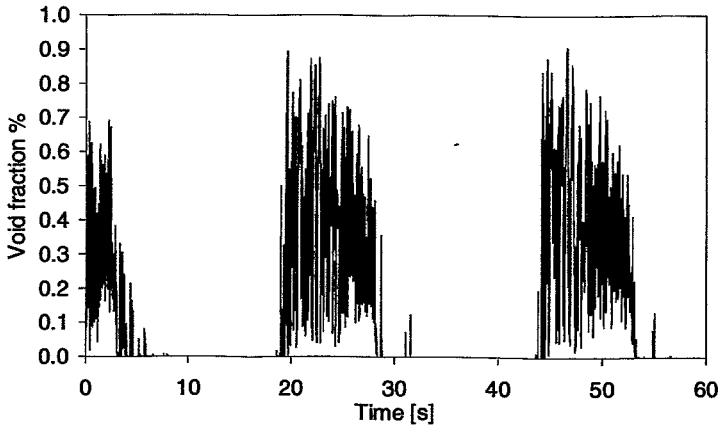

Fig. 5 Average void fraction time series in a section of the riser

The occurrence of periodic void production in the riser is originated by enthalpy perturbations that travel from the heated section to the top of the riser. A confirmation that the feedback mechanism for this kind of instabilities is linked to "enthalpy waves" travelling upward in the system can be found in Fig. 6, where typical time traces of the temperature at the inlet and the exit of the riser encountered during flashing-induced oscillations are presented. The two time series are out of phase, indicating the wavy character of travelling enthalpy variations.

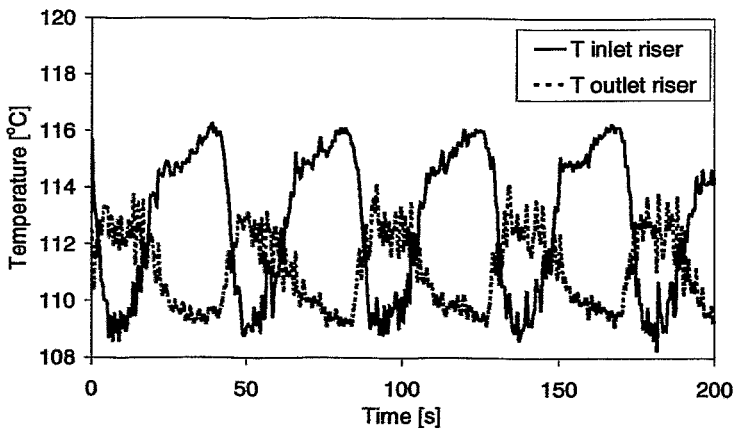

Fig. 6 Typical time traces of inlet and outlet temperatures in the riser during flashing-induced oscillations

The maximum values of the two temperature signals differ by several degrees from each other. This difference comes from energy conservation; in fact to produce void in an adiabatic section the fluid temperature has to decrease.

LDA set-up

Two LDA set-ups are used to measure the velocity in two heated parallel channels simultaneously. The reference beam technique is applied (see Fig. 7): a laser beam of a given frequency f_0 is divided in two parallel beams by means of a beam-splitter. The two beams are focused on the location where the fluid velocity has to be measured. One of the two beams (the so-called reference beam) is sent directly to the detector. The detector will detect the reference beam together with the light of the other beam (the scatter-beam) scattered by the fluid moving in the channel. The frequency of the scattered light depends on the fluid velocity according to the Doppler principle. The output of the detector will oscillate with a frequency $|f_0 - f_S|$, where f_S is the frequency of the Doppler shifted scattered light given by:

$$f_S = f_0 + \frac{2\sin\frac{\theta}{2}}{\lambda_0}|\vec{v}|\cos\alpha \qquad (1)$$

where v is the scattering particle velocity forming an angle α with the channel axis, θ is the angle formed between the reference and the scattered beam, as illustrated in Fig. 7, and λ_0 is the wave length of the laser used.

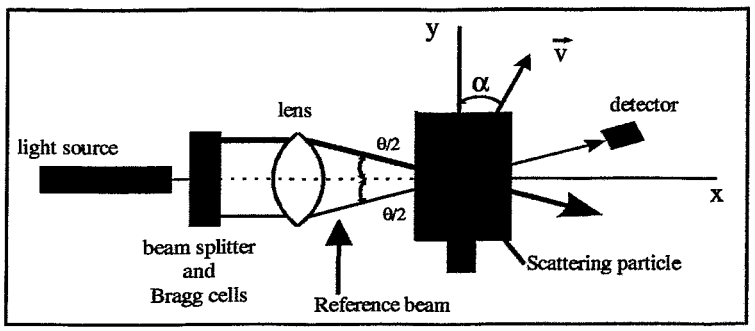

Fig. 7 Schematic representation of the reference beam set-up implemented

In principle, light scattered along the entire path of the scatter-beam will be seen by the detector. However, in practice only scattered light coming from the intersection of the two beams will give rise to a detectable frequency containing the Doppler shift.
As the detector only detects the absolute values of the Doppler shift, no negative velocities can be measured in this way. The measurement of negative velocities is made possible by pre-shifting one of the two beams. This is done by sending each of the two beams through a Bragg cell. The two cells modulate the beams at two chosen frequencies, whose difference is called the shift frequency f_{shift}. In this case the frequency experienced by the detector can be expressed as:

$$f = f_{shift} + \frac{2\sin\frac{\theta}{2}}{\lambda_0}|\vec{v}|\cos\alpha \qquad (2)$$

With an appropriate choice of the shift frequency negative velocities can be measured. In the specific case of the CIRCUS facility a green crystal light laser is used (wavelength of about 530 nm) and a shift frequency of 90kHz has been chosen.
A clear advantage of the LDA technique in comparison with other fast velocity measurement devices (such as, for example, orifice flowmeters) lays in the fact that LDA is not intrusive. The use of forward mode gives an optimal intensity for the

scattered light to be detected, so that no seeds are needed for the detection of the scattered light. This is of particular importance in the study of flashing-induced instabilities since seeds can act as nucleation sites, triggering void production.

Experimental results

Two sets of experiments have been carried out to study the characteristics of natural circulation at low pressure and low power conditions. In both series of measurements the total power has been varied from 5.6 kW to 9.8 kW and the inlet temperature has been ranged from about 98 to 102 °C. In the first set of measurement a symmetric power distribution has been adopted in the four channels, while in the second series of measurements an asymmetric power distribution has been applied. In particular, in the second set of measurements two channels have been kept at constant power equal to 2.8 kW while the power in the other two channels has been varied from 0 to 2.1 kW. Details on the power distributions set during the measurements are reported in Table 1, where P_i indicates the power in the i-th heated channel.

Total power	Series I	Series II
5.6 kW	$P_1 = P_2 = P_3 = P_4 = 1.4$ kW	$P_2 = P_4 = 0$ kW; $P_1 = P_3 = 2.8$ kW
7.0 kW	$P_1 = P_2 = P_3 = P_4 = 1.75$ kW	$P_2 = P_4 = 0.7$ kW; $P_1 = P_3 = 2.8$ kW
8.4 kW	$P_1 = P_2 = P_3 = P_4 = 2.1$ kW	$P_2 = P_4 = 1.4$ kW; $P_1 = P_3 = 2.8$ kW
9.8 kW	$P_1 = P_2 = P_3 = P_4 = 2.45$ kW	$P_2 = P_4 = 2.1$ kW; $P_1 = P_3 = 2.8$ kW

Table 1 Power distribution used during the two set of measurements

From Fig. 8 it can be seen that the oscillation period decreases with increasing power or inlet subcooling for symmetric as well asymmetric power distribution. This is consistent with the increase of average flow rate, reported in Fig. 9 since, as mentioned previously, the period of the oscillation is directly related to the travelling of enthalpy perturbations along the loop.

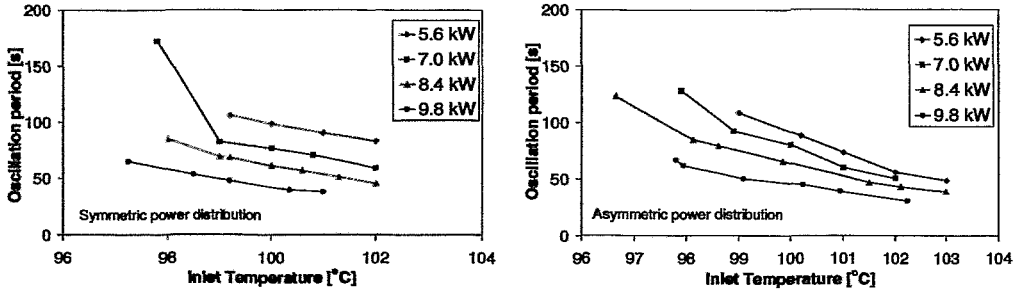

Fig. 8 Period of oscillation as function of power and inlet temperature for symmetric (left) and asymmetric (right) power distribution

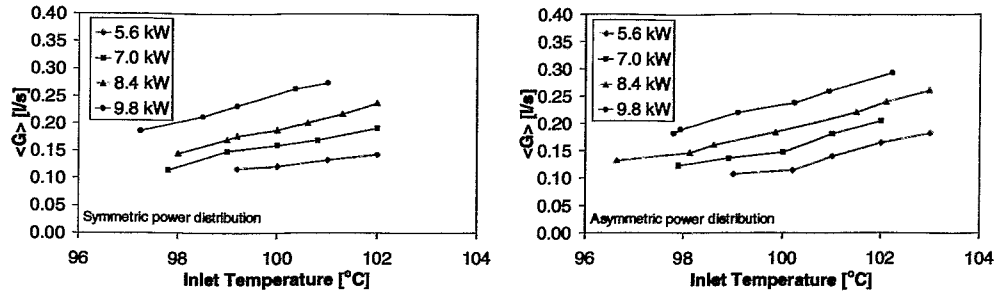

Fig. 9 Average inlet flow as function of power and inlet temperature for symmetric (left) and asymmetric (right) power distribution

In Fig. 10 the oscillation periods recorded during all the experiments performed in the two series of measurements are reported as function of $\tau_{1\phi}$ defined as:

$$\tau_{1\phi} = \frac{V_{core} + V_{riser}}{\langle G \rangle}, \tag{3}$$

where V_{core} and V_{riser} are the volumes of the core and riser section respectively and <G> is the average total flow rate in a period of the oscillation. $\tau_{1\phi}$ is the time needed for the single-phase flow to travel from the inlet of the core to the outlet of the riser with a flow equal to the total average flow rate <G>. It can be seen that, despite the difference in power and in inlet temperatures, most of the cases lay on the same line indicating a relation between period of oscillation and average flow rate. Similar results were already found by Aritomi and Chiang[3,4,5] both in case of natural and forced circulation, although experiments were limited to symmetric power distributions in natural circulation conditions.

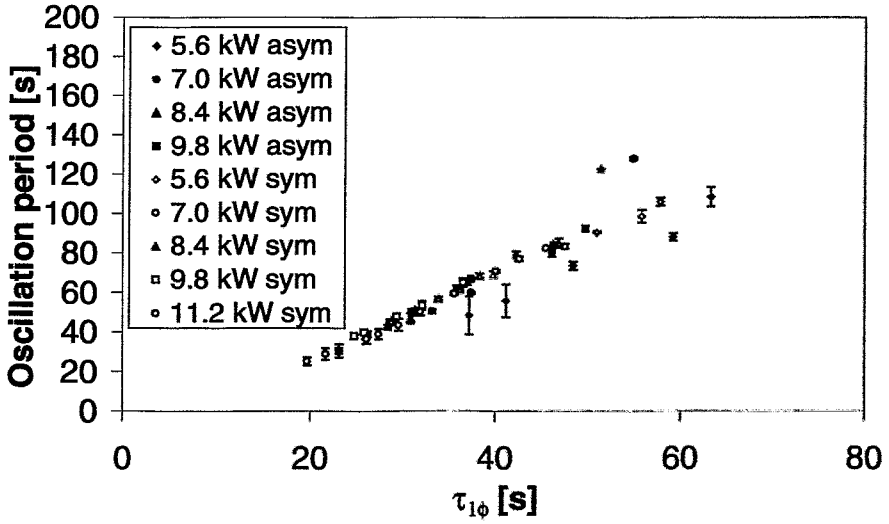

Fig. 10 Relation between oscillation period and average flow rate

Exception to the trend is found at lower flow rates (high $\tau_{1\phi}$) for asymmetric power distributions and all over the experimented range of flow rates for the case of the asymmetric power distribution at 5.6 kW, where the power of two channels is set to zero. The reason for this behaviour is not clear yet. However, in view of the different

flow velocities in asymmetric conditions, it is not surprising that the relation between average flow rate and oscillation period is not linear any longer. As an example, in Fig. 11 the flow velocities measured in two heated channels in case of an asymmetric power distribution are shown. Channel 1 (as well as channel 3) is heated at a power level of 2.8 kW, while channels 2 and 4 are unheated in the case presented. It can be seen that for a long part of the oscillation period the velocity in the unheated channels is much lower than the velocity in the heated channels.

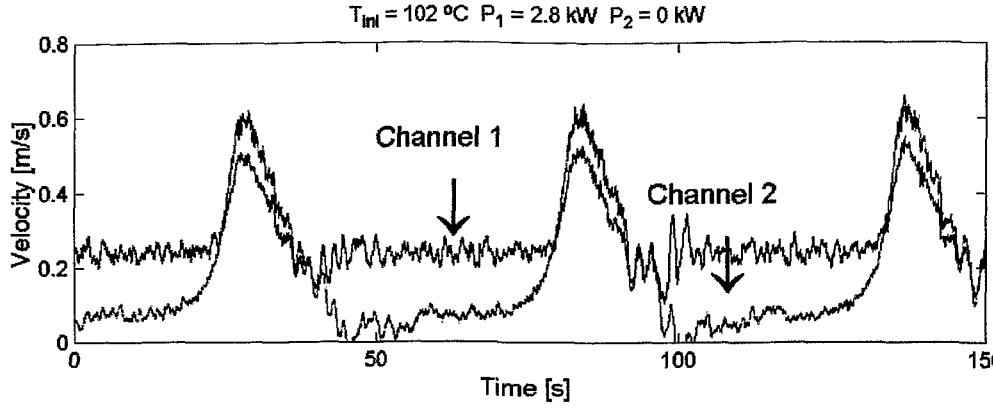

Fig. 11 Lda velocity measurements in two parallel channels for asymmetric power distribution

Conclusions

Different measurements techniques are used simultaneously to study in detail the dynamics of natural circulation cooled systems during flashing-induced instabilities at low pressure and low power conditions. Measurements of the 2D void fraction distribution by means of a wire mesh sensor located at the top of the riser section unveils the complex and fast dynamics of void production due to flashing during natural circulation instabilities. Two sets of experiments carried out at different powers and subcoolings point out a clear dependence of the oscillation period of the instabilities on the average flow rate circulating in the loop. Exceptions are found for some of the asymmetric cases studied.

References

1. MANERA, A., DE KRUIJF, W. J. M., and VAN DER HAGEN, T. H. J. J., "Experiments with the CIRCUS-facility on flashing-induced instabilities during startup of natural-circulation-cooled BWRs," *Proceedings PHYSOR 2000, May 7-11, 2000, Pittsburgh, Pennsylvania, USA (on CDROM)*, 2000,(2000).

2. PRASSER, H.-M., BÖTTGER, A., and ZSCHAU, J., "A new electrode-mesh tomograph for gas-liquid flows," *Flow Measurement and Instrumentation*, **111** (1998).

3. ARITOMI, M., AOKI, S., and INOUE, A., "Instabilities in parallel channel of forced-convection boiling upflow system, III. System with different flow conditions between two channels," *J. Nucl. Sci. and Technol.*, **16**, 343 (1979).

4. ARITOMI, M., CHIANG, J. H., and NAKAHASHI, T., "Fundamental study on thermo-hydrraulics during start-up in natural circulation boiling water reactors, (I) Thermo-hydrauic instabilities," *J. Nucl. Sci. and Technol.*, **29**, 631 (1992).

5. CHIANG, J. H., ARITOMI, M., and MORI, M., "Fundamental study on thermo-hydraulics during start-up in natural circulation Boiling Water Reactors, (II) Natural circulation oscillation induced by hydrostatic head fluctuation," *J. Nucl. Sci. and Technol.*, **30**, 203 (1993).

Methods to investigate the RPV exterior two-phase flow behavior in the event of a core melt

H. Schmidt[1], W. Brettschuh[1], J. Meseth[1], E. Friesen[1], O. Herbst[1], W. Kastner[1], W. Köhler[1] and J.Miettinen[2]

[1]Siemens Nuclear Power GmbH,
P.O. Box 3220, 91050 Erlangen, Germany
Tel.: +49 9131 18 3718
Fax: +49 9131 18 2851
E-mail: Holger.Schmidt@erl11.siemens.de

[2]Technical Research Centre of Finland

1 Introduction

Siemens Nuclear Power (SNP) develops a new boiling water reactor called SWR 1000. It's safety concept will consist of passive safety equipment combined with active systems, and through this diversity, meets the goal of reducing the probability of core damage compared to existing plants. Furthermore, the design is aimed at being able to control a postulated core melt accident to such an extent that the consequences of an accident remain restricted to the plant. The core melt is retained in the Reactor Pressure Vessel (RPV) at low pressure owing to cooling of the RPV exterior. For this purpose a passive flooding system is installed which feeds into the lower area of the drywell from the core flooding pool by gravity. The water will penetrate through apertures in the RPV-insulation in the gap between the insulation and the RPV- wall as it is schematically shown in Fig. 1.

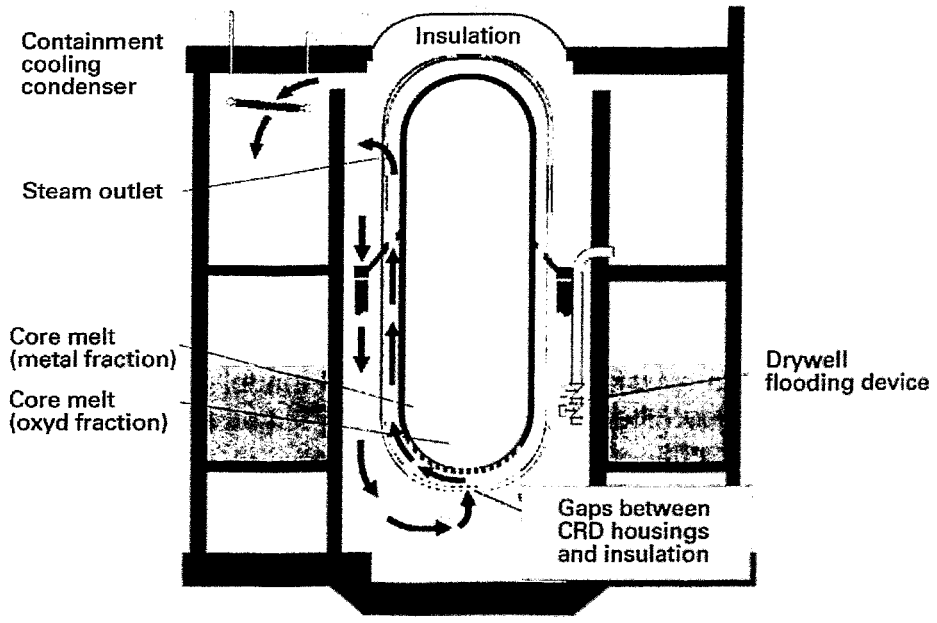

Fig. 1: Scheme of the exterior vessel cooling concept

SNP performs – in co-operation with the Technical Research Centre of Finland (VTT) - tests to quantify the safety margins of the exterior cooling concept of the SWR 1000. A Siemens internal investigation proves that the heat fluxes through the wall will be distributed in such a way that the minimal heat flux will be at the bottom of the RPV. The maximum will be in the spherical part of the RPV with an inclination of almost 50°. The in the literature /1/ to /13/ mentioned critical heat fluxes for comparable configurations are in the range of 300 to 500 kW/m² at the bottom and 1000 to 1500 kW/m² at the side and are almost five times higher than the calculated heat fluxes through the RPV wall. The comparison of literature values and heat fluxes through the RPV indicates high safety margins. Anyhow, the influence of the control rod drive (CRD) housing is unknown. It is the aim of the investigation to demonstrate the functioning of the exterior cooling concept and to quantify the safety margins.

The heat transfer conditions will be very complex. The local heat transfer as well as the global flow behavior may influence the critical heat fluxes (CHF). For that reason it is planned to measure critical heat fluxes in a section model with a 1:1 scaling. The flow and heat transfer conditions will be decoupled in order to prove that the section is representative. The procedure contains three different kinds of tests which are mentioned in Fig. 2 and which are described in the following:

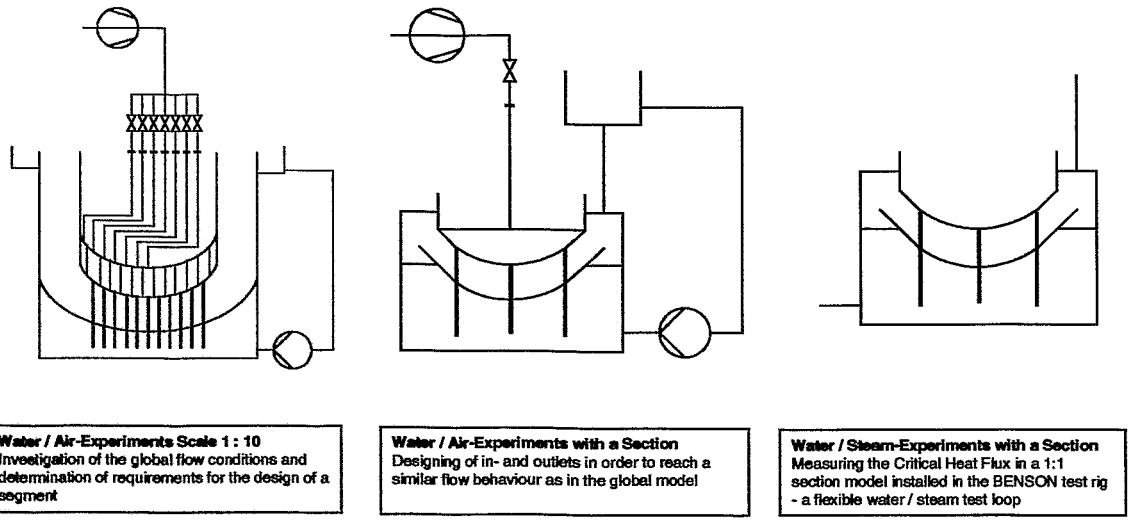

Fig. 2: Decoupling of flow conditions and heat transfer

- Investigation on the flow conditions in a global model
  The aim of the tests with a water/air operated global model is to describe the flow behavior in the gap between the insulation and the RPV and to have a data base to validate or to adapt programs.
- Investigation on the flow conditions in a segment model
  The aim of the tests is to prove that the flow in segment is similar to flow in the global model.
- Measurement of Safety Margins
  The aim of the tests is to measure the CHF up to three times of the heat fluxes which would occur in the event of a hypothetical core melt accident. A segment model will be installed in the BENSON test rig in order to supply it with water of pressure

between 4 and 1,3 bar and a subcooling of 0 to 10 K. The segment model will be heated and the CHF will be identified based on temperature measurements of the wall.

The tests to investigate the flow conditions in the global model are finished. A Laser-Doppler-Anemometer has been used to measure the liquid velocities. The void fraction was determined using a fiber optical needle probe and impedance probes. Mass balances performed based on the measurements prove the plausibility of the applied methods.

2 Setup of the global model

It is the aim of the tests with the global flow model to investigate the flow behavior in the case of the exterior cooling by performing water/air experiments. Fig. 3 shows the model which size is 1:10. The main components are the simulated RPV and the insulation, which is made of a transparent material. The internal pumps and control rod drive housings are simulated by transparent bars. The bottom of the simulated RPV is made of a porous structure. In order to simulate boiling on the outer surface of the RPV air was pressed through this material. The setup of the RPV consists eight rotational symmetric chambers in order to simulate the in chapter 1 mentioned heat flux distribution. Each of the chambers has an own air supply and the air mass flow can be adjusted individually.

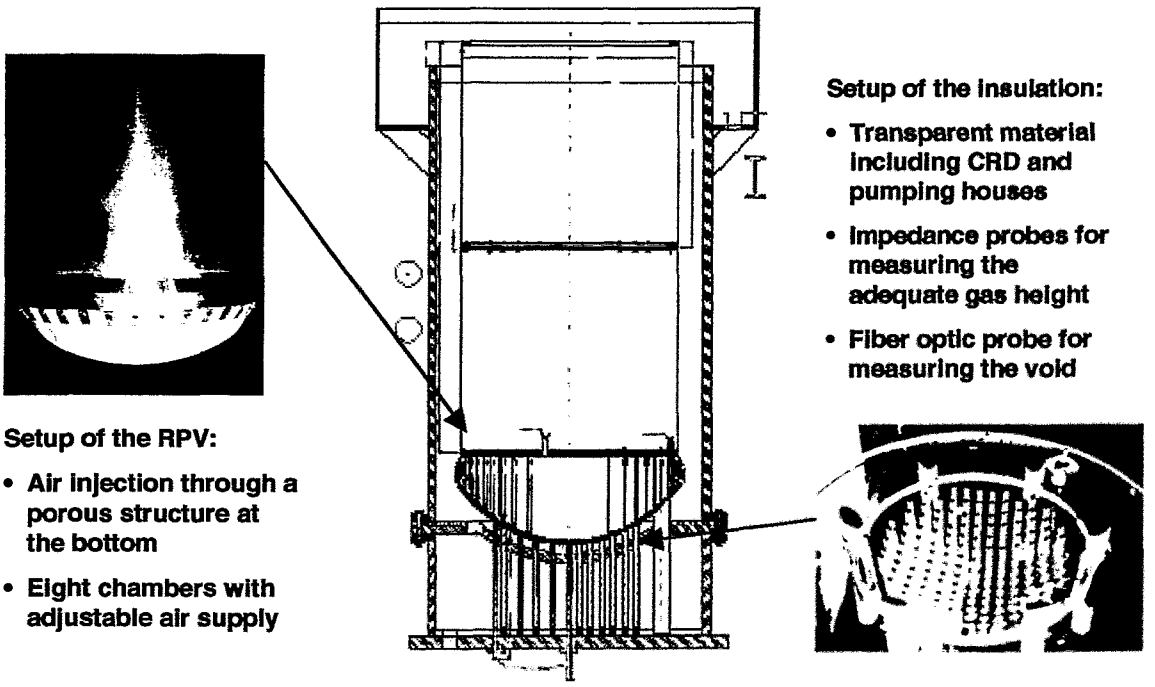

Fig. 3: Global model

3 Phenomenology

Based on visual observation the following impression of the flow behavior was received: The main characteristica are the circulation and the counter-current flow at the bottom of the RPV as it is schematically shown in Fig. 4. One can see that the water/air mixture flows around the calotte of the RPV. Opposite to the direction of the mixture flow one can see a single-phase water flow along the insulation. This proves that water will flow in the direction of the source (heat or in the case of the tests injection). By observing small sized bubbles one has the impression as if water penetrates during the counter-current flow into the water/air mixture. A view from a position below the model in the direction of the RPV gave the impression as if the flow is rotational symmetric and as if there are no preference directions of the water/air flow. The performed measurements underline the visual observation based description of the global flow behavior.

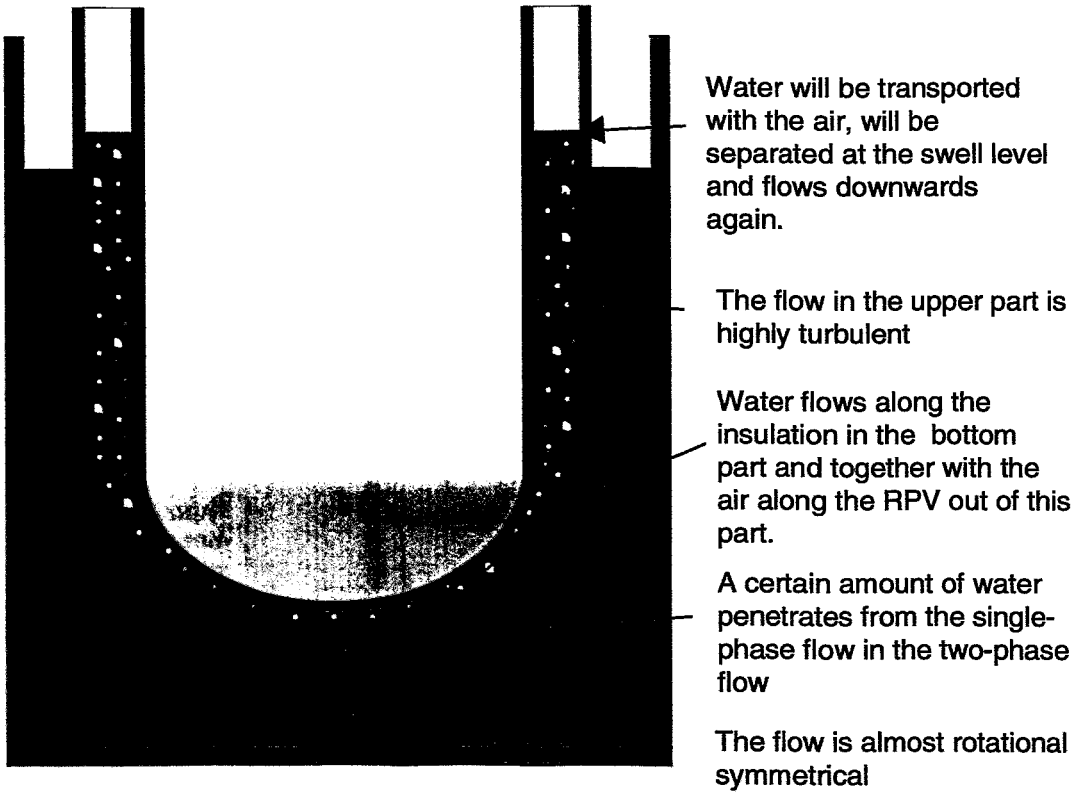

Fig. 4: Phenomenology

4 Measurement techniques

The following three different measurement techniques have been used to investigate the flow around the RPV:

- Fiber optical needle probe – to measure the local void fraction at some positions
- Impedance probes – to measure an averaged void fraction

- Laser-Doppler-Anemometer – to measure local velocities.

4.1 Fiber optical needle probe measurements

Fig. 5 shows the fiber optical needle probe which has been delivered by the Technical University of Darmstadt /14/. It is designed in such a way that the probe can be moved in the direction of the axis of the surrounding tube, that has an outer diameter of the simulated CRD-housings. It has been installed instead of one of the transparent bares as they are shown in Fig. 3. The needle itself consists of two glass wires which are glued together at one side. This end is conical. Light will be submitted in the other end of one of the wires. The light will be reflected or emitted - depending on the phase (water respectively air) at the conical end. At the end of the other wire there is an detector which transforms the optical signal into an electrical one. Fig. 6 shows typical signals as they have been detected during a pre-test in which air has been pressed through a downwards facing horizontal plate. A level defines the period of time in which gas appears at the end of the probe t_g. By dividing this time period by the total observation time t one gets the time averaged local void fraction ε, which is plotted as a function of the height in Fig. 6 and is defined according Eq. (1):

$$\varepsilon = \frac{t_g}{t} \qquad (1)$$

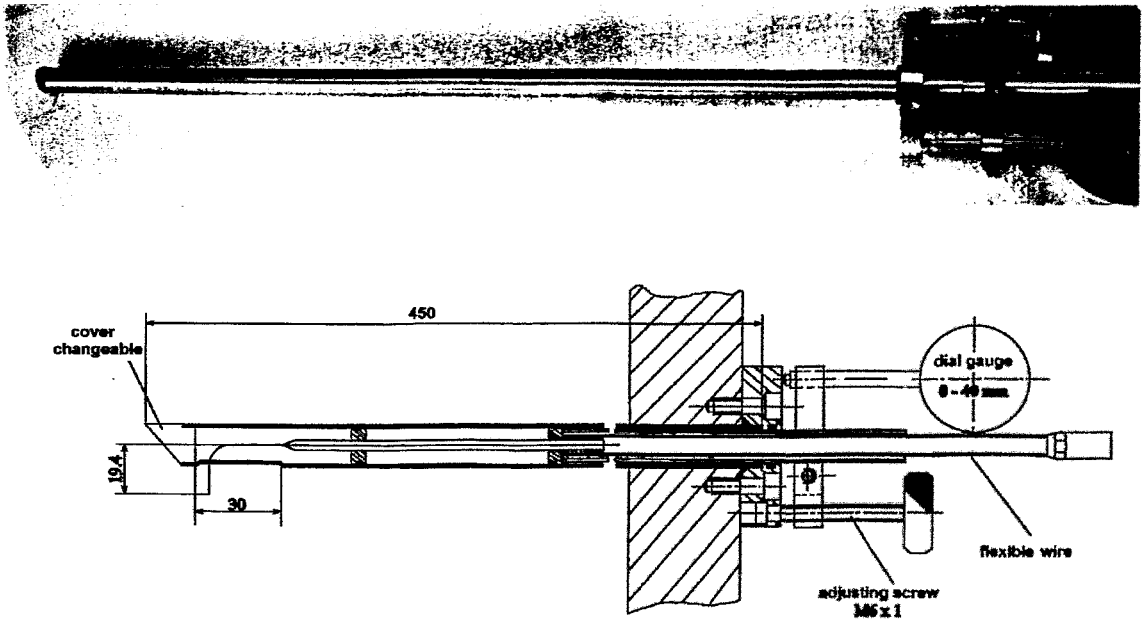

Fig. 5: Fiber optical needle probe

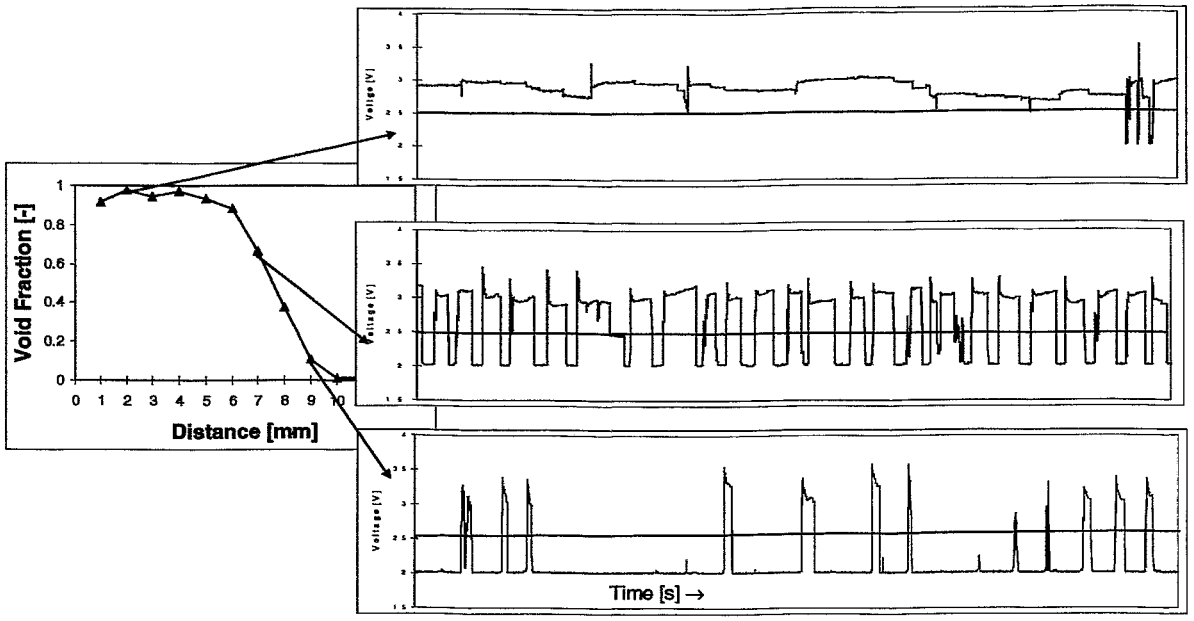

Fig. 6: Local void fraction determination

The fiber optical needle probe has been mounted at two different positions in the global model. The needle itself points into the main flow direction with the effect that the wires will have a minor influence on the measurement of the void fraction. In contrast to pre-tests with an inclination of 0° the void fraction distribution is flatter and almost linear as Fig. 7 shows.

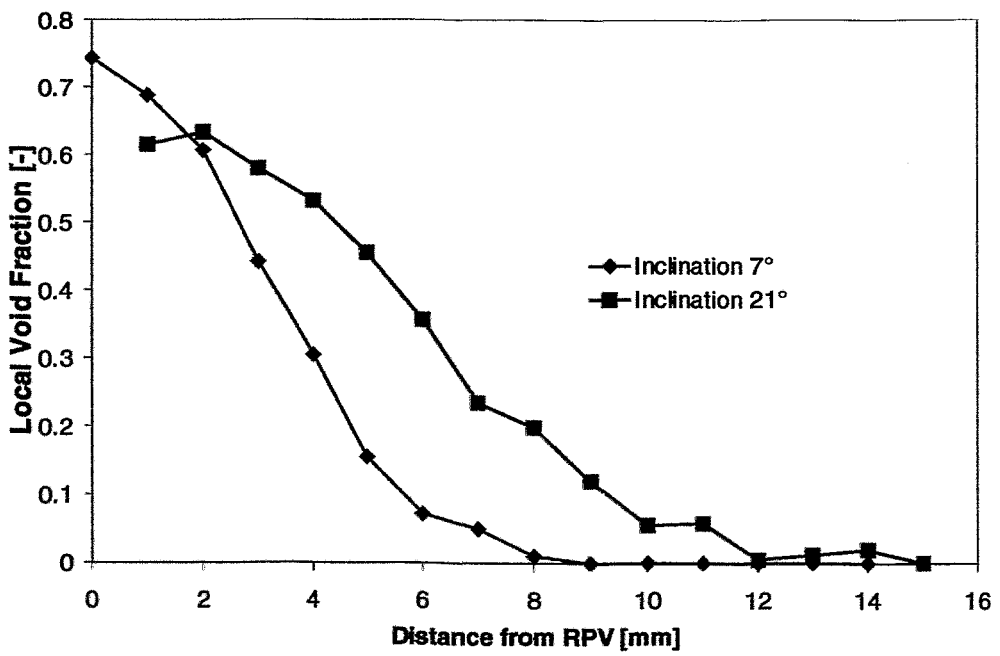

Fig. 7: Local void fractions at different inclinations

4.2 Impedance probes measurements

One quarter of the simulated CRD-drive houses has been replaced by electrodes of the same shape as the transparent bars. The electrical capacity has been measured for all pairs of neighboring electrodes - for single-phase water C_l, single-phase gas C_g and for the two-phase flow mixture C. The volume averaged void fraction $\bar{\varepsilon}$ is:

$$\bar{\varepsilon} = \frac{C - C_g}{C_l - C_g} \quad (2)$$

if one assumes that the void fraction distribution as a function of the height is equal in the whole area between the neighboring electrodes. The void fraction according Eq. (2) is an average over the whole gap between insulation and RPV. In this region a counter-current flow occurs with single-phase water flow along the insulation and two-phase flow along the RPV. To get an impressive description of the such a void fraction it is attractive to transform it into a geometrical value like the gas height h_g, which is described by the height of the whole gap h according Eq. (3):

$$h_g = \bar{\varepsilon}\, h \quad (3)$$

The gas height is supposed to be similar to the integration of the local void fraction over the height according to Eq. (4):

$$h_g = \int_0^h \varepsilon \, dh \quad (4)$$

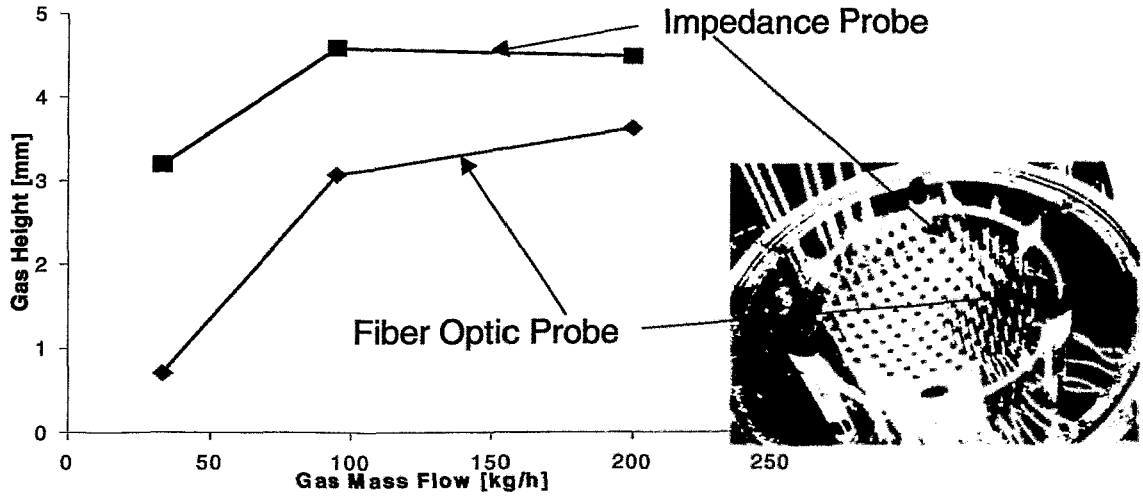

Fig. 8: Average gas height measured with fiber optical needle probe and impedance probes

Fig. 8 shows gas heights measured with impedance probes and the fiber optical needle probe as a function of different injected gas mass flows. The measurements

with the impedance probes deliver a little bit higher gas heights as the measurements with the fiber optical needle probe. This can be explained by the local flow conditions around the control rod drive housings. The needle probe has to be installed in the main flow direction, as explained in chapter 4.1. The pair of impedance probes, which delivers a gas height comparable to the needle probe, has to be in the line of the main flow direction. The visual observation proves, that the gas is pilled up in front of the control rod drive housings, whereas the gas level seems to be a little lower behind the control rod drive housings. These local flow conditions will have two effects. First, the gas height delivered by the impedance probes is a bit to high. Second, the gas height estimated by the fiber optical needle probe is a bit lower than the average gas height between the electrodes. This interpretation, together with the fact that the absolute differences between the gas height curves of Fig. 8 are small, prove the functioning of both void fraction measurement methods. In addition one can assume a higher accuracy for the gas height measurement with the impedance probes for pairs of electrodes which are orientated normal to the main flow direction.

All impedance probes together deliver a gas height distribution in a 90° sector of the model, as it is shown in Fig. 9. The colours of the squares in Fig. 9 represent the gas height between two neighboring control rod drive housings marked by circuits. The gas heights are almost rotational symmetrical distributed, which underlines the visual observation according chapter 2.1.

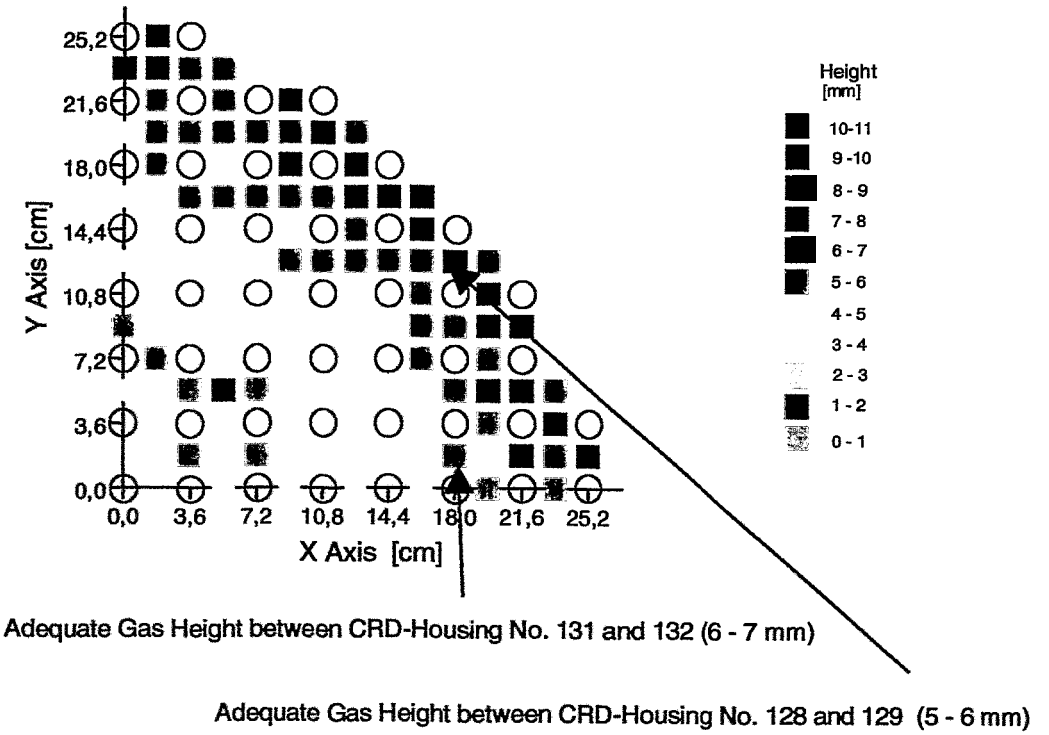

Fig. 9: Gas height distribution

4.3 Laser-Doppler Anemometer measurements

Nowadays Laser-Doppler Anemometers (LDA) are commercial available. Their main application is the measurement of single-phase flow velocities. The theoretical background of this technique is described in publications like /15/. The LDA, which has been used during the described tests, is a product of *Dantec Measurement Technology* (see background figures under www.dantecmt.com). In the following the way how a LDA works is described - so far it is necessary for the handling of the complete system and the interpretation of the results.

The functioning of a LDA is based on the Doppler principle - as the name indicates. Two laser beams (monochromatical and unipolar light) with a defined shift frequency will be focused via an optical system. The beams form an ellipsoidal volume when they are crossing each others. The reflection of a tracer particle crossing this volume will be detected by a photo multiplier. The frequency of the reflected light is proportional to the velocity of the tracer particle, which will be calculated by a computer.

The LDA-system delivers values for the velocity of tracer particles. The definition of the test procedure, the interpretation and the plausibility tests depend on each individual application. In the following part some of the activities are mentioned to get reliable values for the velocity around the RPV.

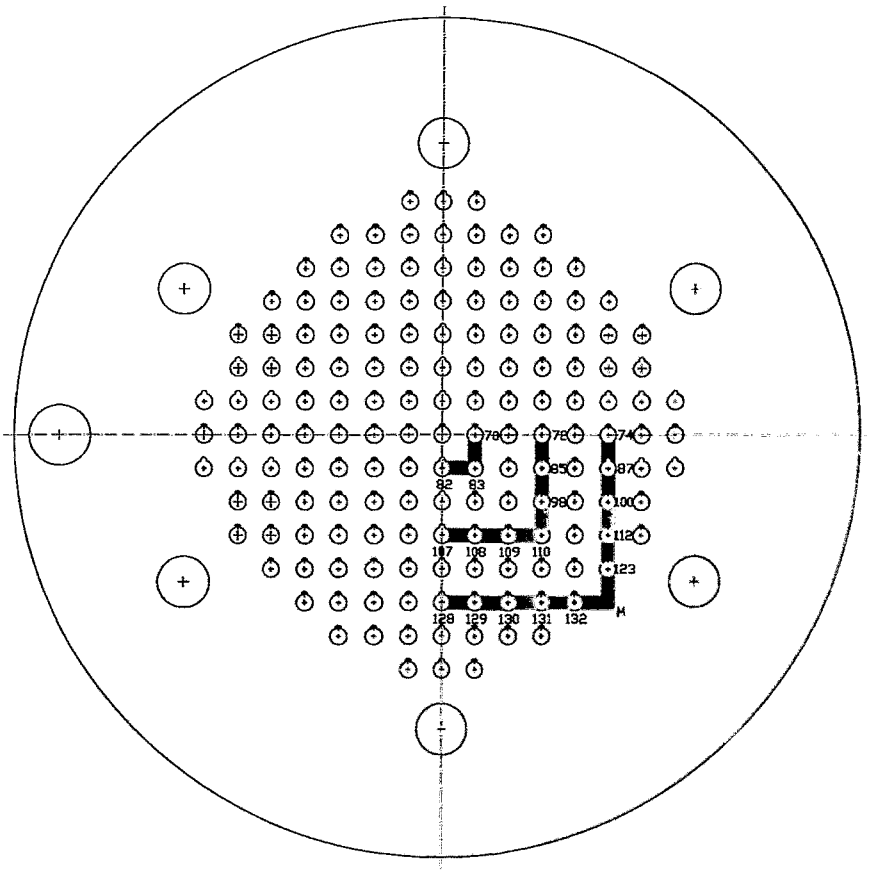

Fig. 10: Positions of the LDA measurements

4.3.1 Test procedure

The flow around the RPV is highly turbulent. For that reason it was necessary to measure some hundreds of velocities at one position to get the real average value. The optical system of the LDA has been moved from a position below the model in the upwards direction. Based on these measurements it was possible to get a velocity profile as a function of the height. The position of each measurement profile is shown in Fig. 10. It is always in the middle between two neighboring control rod drive housings. The measured velocities are normal to a line between the neighboring control rod drive housings and are almost similar to the average values on this line – this has been tested by measuring the velocities along this line at different heights.

The refraction of the laser beams influences not only the position of the measuring volume but also the length of this volume - increased by 50%. This has been taken into account when the optical system was positioned. The increased length of the volume must be considered during the interpretation of the measured velocities.

4.3.2 Interpretation of the velocities

Fig. 11 shows velocity profiles as a function of the height. Typical for these profiles are areas with negative velocities, which indicate a flow along the insulation to the vertex, and positive ones, which indicate a flow along the RPV out of the lower part of the gap between insulation and RPV. The absolute values of the average velocities in the negative area are lower than the ones in the positive area. This is plausible. The negative velocities occur in an area with only single-phase flow water, whereas a two-phase flow mixture occurs in the area with positive velocities. The air will accelerate the water and is herewith responsible for the higher velocities in the area with positive velocity. The measured velocities are water velocities, as plausibility tests proved (see chapter 4.3.3).

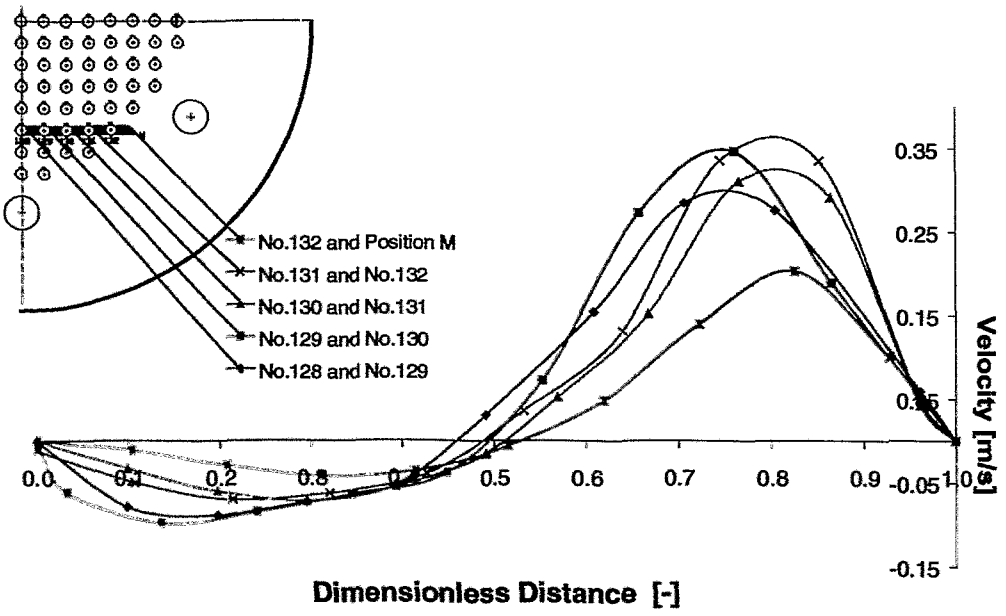

Fig. 11: Velocity distribution as the function of the height

The flatness of the profile is unusual, especially close to the boundaries. The relative long measuring volume is responsible for this effect. Each velocity delivered by the LDA-system is related to the center position of the measuring volume. In reality this value is the one of the average velocity within the length of the measuring volume. According /16/ the probability $p(x)$, that the reflection of the light at a particle occurs at the position x with a distance of $x - x_0$ from the center position of the measuring volume x_0, is proportional to the intensity of the laser $I(x)$ and the velocity $v(x)$:

$$p(x) \sim I(x) \cdot v(x) \tag{5}$$

The intensity of the light is according /16/ proportional to a Normal distribution, which is related to the length of the measuring volume Δx:

$$I(x) \sim \frac{1}{2 \cdot \Delta x \sqrt{\frac{\pi}{2}}} \exp\left(-\frac{2(x - x_0)^2}{(2 \cdot \Delta x)^2} \right) \tag{6}$$

From Eq. (5) and (6) follows Eq.(7) for the measuring volume averaged velocity delivered by the LDA-system:

$$\bar{v}(x_0) = \frac{\int_{x_0 - \Delta x}^{x_0 + \Delta x} p(x) \cdot v(x) \cdot dx}{\int_{x_0 - \Delta x}^{x_0 + \Delta x} p(x) \cdot dx} = \frac{\int_{x_0 - \Delta x}^{x_0 + \Delta x} I(x) \cdot v(x)^2 \cdot dx}{\int_{x_0 - \Delta x}^{x_0 + \Delta x} I(x) \cdot v(x) \cdot dx} \tag{7}$$

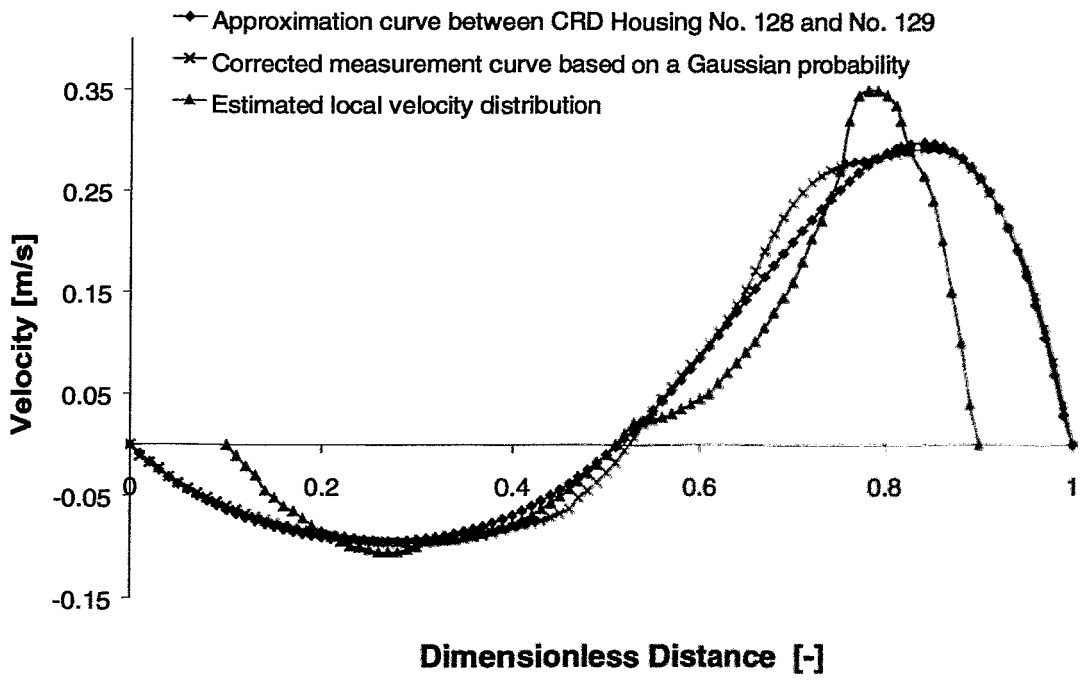

Fig. 12: Local velocities

Fig. 12 shows the local velocity and the averaged velocity profile as it is delivered by the LDA-System and which has been approximated by a polynominyl. One difference is the length of the profiles, which in the case of the local velocities is equivalent to distance between RPV and insulation and which in the case of the averaged velocities is longer. The difference in the length of the profiles is the length of the measuring volume. Another difference is the velocity gradient at the boundaries, which is higher in the case of the local velocities. This is plausible.

4.3.3 Plausibility check

Each of the measurement techniques itself is not new, but their combined application – especially the measurement of the water velocity in the two-phase flow area. For that reason it is essential to perform mass balances as a form of a plausibility check.

The visual observation, the gas height distributions and all velocity measurements together indicate that the flow is almost rotational symmetrical. For that reason it is possible to perform the mass balances based on the velocities between two control rod drive housings with the distance *b*. This means that the water mass balance across the area with negative velocities has to be the same as the water mass balance across the area with the positive values, according to Eq. (8) which represents a numerical integration:

$$\dot{M}_{W;in} = \left\{ \sum_{i=1}^{\substack{\text{Number of positions in the area with negative velocities}-1}} \left[(x_{i+1} - x_i)(v_i\,(\varepsilon_i - 1) + v_{i+1}\,(\varepsilon_{i+1} - 1))\,\rho_L\,\frac{1}{2} \right] \right\} b\,(-1) \overset{!}{=}$$

$$\dot{M}_{W;out} = \left\{ \sum_{i=1}^{\substack{\text{Number of positions in the area with positive velocities}-1}} \left[(x_{i+1} - x_i)(v_i \cdot (\varepsilon_i - 1) + v_{i+1} \cdot (\varepsilon_{i+1} - 1))\,\rho_L\,\frac{1}{2} \right] \right\} b \qquad (8)$$

The void fraction in the area with negative velocities is zero, whereas the distribution of the void fraction in the area with positive velocities is almost linear as a function of the height (Fig. 7 indicates the plausibility of the linear approach). The form of the linear profile can be described by the following two assumptions. First, the void fraction is zero at the defection point of the velocity profile. Second, the integration over the height according to Eq. (4) is the gas height measured with the impedance probes at this position. Based on these assumptions it is possible to check the water mass balance based on Eq. (8).

The gas mass balance has to be performed indirectly. This means, it can be checked whether the effect of the injected gas mass flow, which has been measured, is plausible. An approach is to assume that the area between two control rod drive housings might be described as two channels – one for the area with positive and one for the area with negative velocities. The void fraction in the upper channel is the ratio of the gas height to the velocity deflection point h_2:

$$\varepsilon = \frac{h_G}{h_2} \qquad (9)$$

It is possible to predict the void fraction in such inclined channels according the Chexal-Lellouche /17/ correlation. This correlation requires as a kind of input values the properties, the inclination, the hydraulic diameter (which is in this case $d_h = 2\,b\,h_2/(b+h_2)$) and the superficial velocities of gas and liquid. Fig. 13 shows the void fractions calculated with the Chexal-Lellouche correlation. The superficial velocity of the water is the ratio of the inlet water mass flow of Eq. (8) and the cross section. The gas superficial velocity has been varied. The gas mass flow in Fig. 13 is the superficial velocity multiplied by the cross section of the balance area. The red lines in Fig. 13 indicate the values of gas mass flows affecting void fractions which are equivalent to the measured (defined according Eq. (9)).

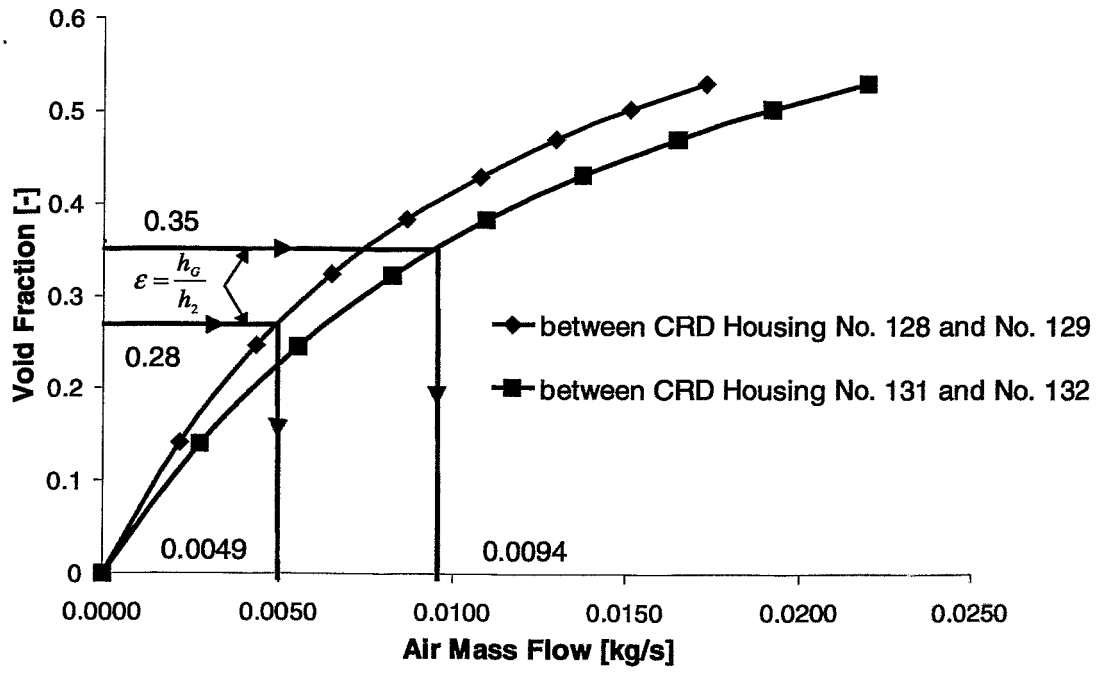

Fig. 13: Gas mass flow balance

Fig. 14 contains the results of mass balances performed at two positions. The accuracy is in the range of 20%, which is a good agreement for two-phase flow conditions. The main conclusion is, that the interpretation of the measurements is plausible.

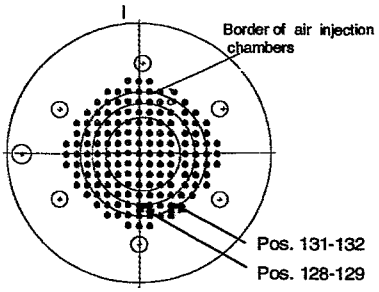

	Position 128-129	Position 131-132
Water Mass Flow, Inlet [kg/s]	1,19	1,36
Water Mass Flow, Outlet [kg/s]	1,40	1,59
Ratio Water Mass Flow Out/In	1,18	1,17
Air Mass Flow, Injected [kg/s]	0,0043	0,0085
Air Mass Flow, Acc. Fig. 13 [kg/s]	0,0049	0,0094
Ratio Out/In	1,14	1,11

Fig. 14: Results of the mass balances

4 Conclusions and outlook

It is the aim of the tests to investigate the flow conditions around the RPV for the case of a hypothetical accident with core melting. Three different measurement techniques have been used for this purpose. The test in the global model have been compared with measurements in section models and the similarity of the flow conditions could be demonstrated. Based on this comparison it was possible to find the size of a section with almost similar flow conditions as they occur in the case of the flow around the whole RPV.

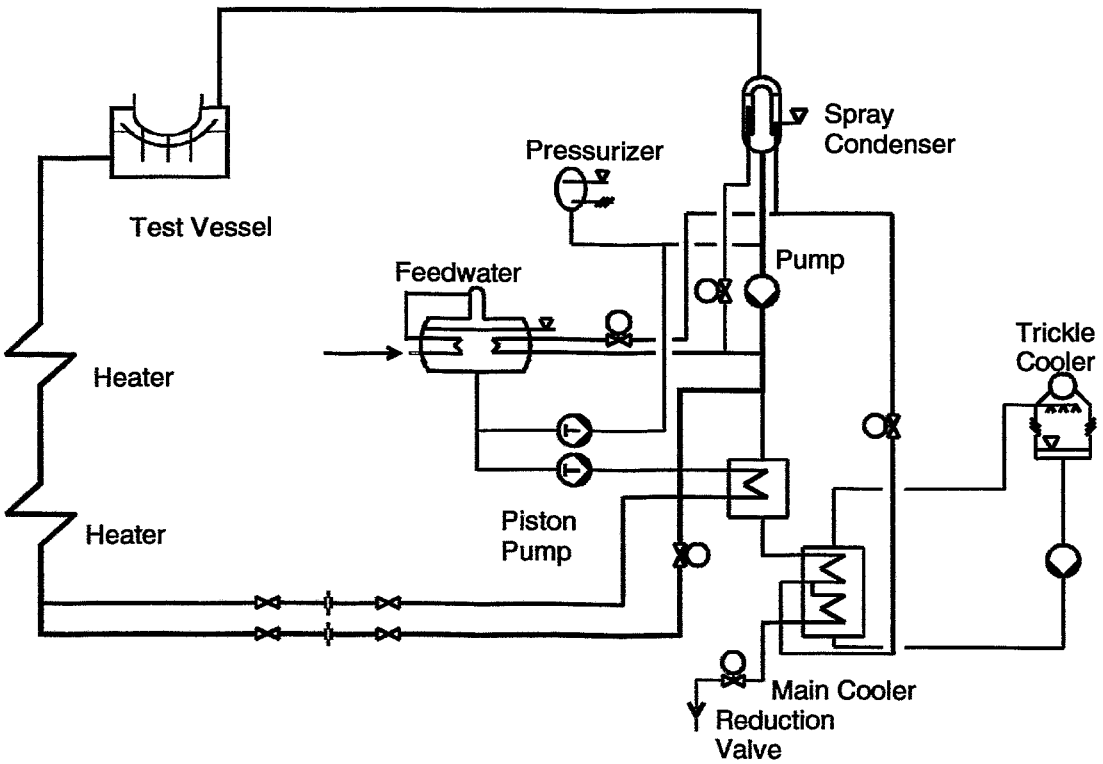

Fig. 15: Measurement of safety margins with the BENSON test rig

In addition, the measurements are the data base to adjust computer codes. VTT will use these codes to confirm the selected size of the heatable section. Such a section (1:1 scale) will be integrated into the BENSON test rig (see Fig. 15) which is a flexible separate effect test facility and which can be operated in the range of pressures from 1 to 330 bar, of fluid temperatures from 20 to 600°C, of mass flows up to 28 kg/s and of electrical heat capacities up to 2 MW. The heat flux will be increased until a boiling crisis occurs or a safety margin of 3 is reached.

To use a LDA to measure the velocity of the liquid phase in a water/air mixture is a new application for this technique. Therefore it was essential to prove the plausibility of these measurements. Water and air mass flow balances prove that the measurements are reliable.

Literature

/1/ Cheung F.B., Haddad K.H., Liu Y.C, Shia S.W., High Heat Flux Nucleate Boiling on the Outer Surface of a Heated Hemispherical Vessel, AIChe Symp. Ser. Vol. 93, No. 314, pp.95-101, 1997

/2/ Theofanous T.G., Liu C., Additon S., Angelini S. Kymäläinen O., Salmassi T., Invessel Coolability and Retention of a Core Melt, DOE/ID-10460 Vol. 1 and 2, October 1996

/3/ Henry R.E. and Fauske H.K., External Cooling of a Reactor Vessel under Severe Accident Conditions, Nuclear Engineering and Design, 139 (1993), pp. 31-43

/4/ Henry R.E. et al., Experiments on the Lower Plenum Response During a Severe Accident, Proc. 4th Int. Topical Meet. on Nuclear Thermal Hydraulics, Operations and Safety, Vol. 1, April 1994, pp. 27-C1-6

/5/ Theofanous T.G., Liu C., Additon S., Angelini S. Kymäläinen O., Salmassi T., Invessel Coolability and Retention of a Core Melt, Nuclear Engineering and Design, 169 (1997), pp. 49-57

/6/ Rouge S., SULTAN Test Facility, Large Scale Vessel Coolability in Natural Convection at Low Pressure, NURETH-7 Conf., Saratoga Springs, NY, USA, Sept. 10-15, 1995

/7/ Rouge S., Dor I. Geffraye G. Reactor Vessel External Cooling for Corium Retention, SULTAN Experimental Program and Modeling with CATHARE Code, OECD Workshop on IN-Vessel Debris Retention and Coolability, Garching, Germany, March 3-6, 1998

/8/ Theofanous T.G., Syri S., Salmassi T., Kymäläinen O., Tuomisto H., Critical Heat Flux through Curved, Downward Facing, Thick Walls, Int. Conf. on New Trends in Nuclear System Thermohydraulics, May 30th –June 2nd, 1994, Pisa, Proc. Vol. 2, pp. 585-597

/9/ Theofanous T.G. and Syri S., The Coolability Limits of a Reactor Pressure Vessel Lower Head, NURETH-7 Conf., Saratoga Springs, NY, USA, Sept. 10-15, 1995

/10/ Seiler J.M., Dossier de'analyse GAREC, Retention du corium en curve. Synthese, CEA STR/LTEM/96-42, pp. 140-174

/11/ Cheung F.B., Haddad K.H., A Hydrodynamic Critical Heat Flux Model for Saturated Pool Boiling on a Downward Facing Curved Heating Surface, Int. J. Heat Transfer, 40 (1997), pp. 1291-1302

/12/ Cheung F.B., Liu Y.C., Natural Convection Boiling on the Outer Surface of a Hemispherical Vessel Surrounded by a Thermal Insulation Structure, OECD Workshop on In-Vessel Debris Retention and Coolability, Garching, May 3-6,1998

/13/ Theofanous T.G., Yuen W.W., Fundamentals of Boiling and Multiphase Flow under Extreme Conditions, Heat Transfer 1998, Proceedings of the11th IHTC, Vol. 1, pp. 131-147, Kyongju, 1998

/14/ Benk H., Information zur Verwendung der faseroptischen Meßtechnik für Strömungsuntersuchungen im RDB-Modell zum SWR 1000, TU-Darmstadt, 1999

/15/ Durst F., Melling A., Whitelaw J.H., Theorie und Praxis der Laser-Doppler-Anemometrie, G.Bauer Verlag, Karlsruhe, 1987

/16/ Waßner E., Strömungsuntersuchungen mit der Laser-Doppler-Anemometrie bei der Extrusion von Polyethylenschmelzen, Shaker Verlag, Aachen, 1998

/17/ Chexal et. al., Void Fraction Technology for Design and Analysis, EPRI-Report TR-106326, March 1997

Verification of Simulation Results of Mixture Level Transients and Evaporation Processes in Pressure Vessels using Needle-shaped Probes

A. Traichel, W. Kästner, S. Schefter, V. Schneider, S. Fleischer, T. Gocht, R. Hampel

Institute for Process Technique, Process Automation and Measuring Technique (IPM)
at the University of Applied Sciences Zittau/Görlitz (FH)
D-02763 Zittau, Theodor-Körner-Allee 16
Tel: +49-(0)3583-61-1383, Fax: +49-(0)3583-61-1288
E-mail: ipm@hs-zigr.de

1 Experiments with depressurisation

For a continuous monitoring, control, and diagnosis of high transient technical processes in safety-related systems in Nuclear Technology it is necessary to provide the knowledge about the actual state of process in form of measurable and non-measurable state variables. Especially the monitoring of water level within pressure vessels with water-steam mixture (pressuriser, steam generator, reactor pressure vessel) during accidental depressurisations is very important. A lot of hydrostatic measuring systems are installed at the technical facility for this task. Our subject of investigation is the monitoring of the mixture level within the pressure vessel, which comes into existence in case of evaporation processes (Fig. 1). The paper deals with the simulation (ATHLET-Code [4]) of mixture level transients and evaporation processes in pressure vessels during the depressurisation. For the verification of the simulation results needle-shaped probes were applied.

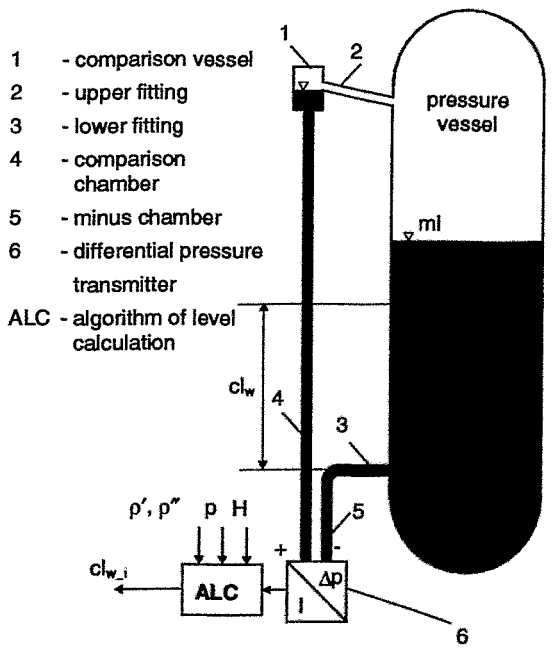

Fig. 1: Pressure vessel with water steam mixture and hydrostatic measuring system,
cl_w – measurable collapsed level between the fittings of wide range system,
ml – non-measurable mixture level within pressure vessel

The additional information about the mixture level is important for e. g. :

⇒ prevention of turbine damage by water entrainment and

⇒ prevention of uncovering of heating systems.

The problem is the fact that the mixture level is a high transient non-measurable value concerning usual hydrostatic water level measuring systems.

Our methodology for the verification of the mixture level transient is the following conception [6]:

⇒ Blow Down experiments with application of measuring systems for transient two-phase mixtures (needle-shaped probes - NSP),

⇒ simulation of thermal hydraulic processes in pressure vessels with water steam mixture using thermal hydraulic ATHLET-Code,

⇒ comparison between experiment and simulation.

For simulation, test and verification of mixture level by needle-shaped probes a lot of Blow Down experiments at the test facility DHVA at the IPM with different boundary conditions were carried out.

The procedure of the experiments will be exemplified:

⇒ achieving a steady state (p = 7.0 MPa)

⇒ opening of leak (starting point of Blow Down)

⇒ feed in of water from the preheater ($p \approx 1.5$ MPa ; $\vartheta \approx 200°C$)

⇒ closing of leak (end of Blow Down)

⇒ new steady state ($p \approx 0.2$ ... 0.3 MPa).

In Table 1 characteristic values of experiment parameters are listed for an example of one Blow Down experiment (BD15SG0). This corresponds to real procedures of disturbances in boiling water reactors (BWR).

Parameter	**Value**
Initial collapsed level	2.09 m
Initial pressure	6.8 MPa
Final collapsed level	1.29 m
Final pressure	0.19 MPa
Maximum rising up of mixture level	2.91 m

Action	**Time**
Opening of leak (starting point Blow Down)	100 s
Begin of feed in	157 s
End of feed in	245 s
Closing of leak	426 s
Time of investigation	500 s

Table 1: Characteristic values of boundary conditions of Blow Down experiment BD15SG0

Fig. 2 shows the associated time response of pressure within vessel and preheater during the depressurisation as well as the post-calculated by ATHLET-Code in comparison.

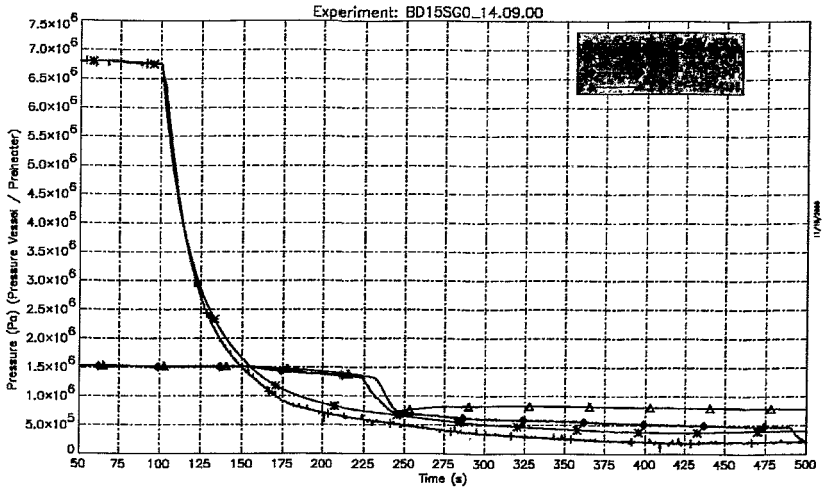

Fig. 2: Time response of pressure within vessel (PV) and preheater (PH) during experiment (EXP) and post-calculated by ATHLET-code (ATH)

The post-calculation reaches a good agreement to the experimental data in high pressure values and a sufficient in the low pressure values.

The mixture level transient is identified by following effects in the vessel:

⇒ rapid increase of mixture level as a result of the initiated evaporation (opening of leak)

⇒ gradual decrease of all water levels as a result of the boiling in connection with mass loss beyond the leak

⇒ gradual increase of all water levels as a result of feed in

⇒ rapid decrease of mixture level as a result of the collapse of water steam mixture (closing of leak)

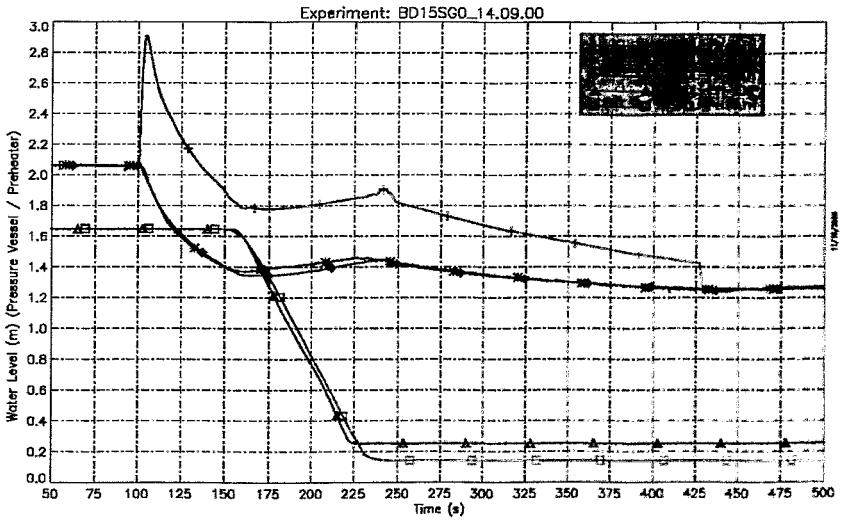

Fig. 3: Time Response of collapsed (CL) and mixture level (ML) within pressure vessel (PV) as well as collapsed level of preheater (PH) during Blow Down experiment (EXP) and post-calculated by ATHLET-code (ATH)

In Fig. 3 the comparison of water level response is illustrated. The mixture level response is the calculated by ATHLET-Code, which is based on the calculated collapsed level. Between

the experimental and calculated data of collapsed level is a very exact correspondence. That means the ATHLET-Code reflects the process behaviour very well [6]. The deviation in the preheater water level after t ≈ 225 s results in fact of the limitation by the measuring system range.

The interesting parameter mixture level, which is non-measurable by usual hydrostatic measuring system, has to be verified by needle-shaped probes for two-phase flow.

2 Detection of mixture level transfer by using needle-shaped probes (special instrumentation)

Needle-shaped probes (NSP) are a special instrumentation for two-phase flow to detect the mixture level interface area as well as a local steam content [1, 2, 3, 6]. In Fig. 4 a construction scheme of NSP in principle is demonstrated. The basic point of the signal processing is established by the different conductivity of steam and water phase. A short overview about the measuring principle gives Fig. 4, too. It deals with a water-steam mixture moving within a time interval. The threshold value phi_65 is fixed, which represents an optimal threshold for detecting steam (U = 3700 mV after ADC in a range between 2800 ... 4100 mV). Depending on this threshold value an impulse-shaped measuring signal with binary character will be generated. It corresponds to respective phases which will be detected at the top of the NSP's.

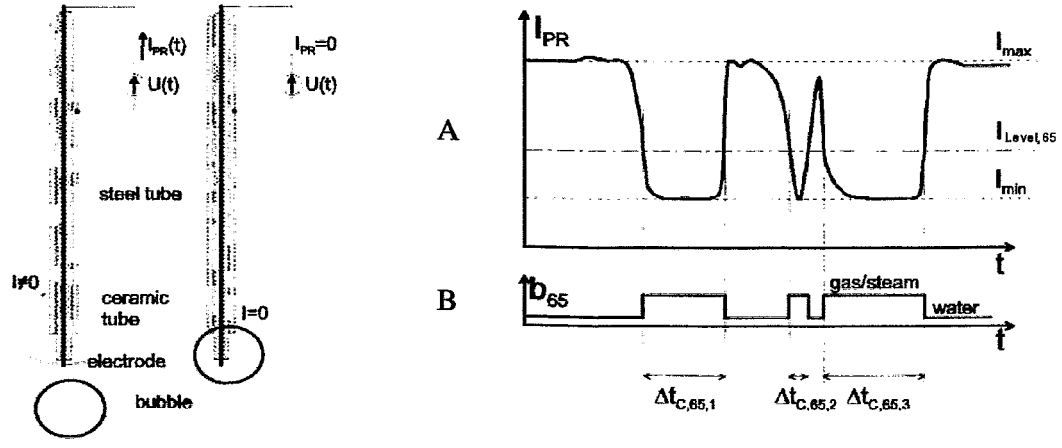

Fig. 4: Construction scheme and signal processing of needle-shaped probes [2]

A The analogous signal (signal of contact with steam bubble and probe top) will be formed in consequence of steam bubble deformation at the needle-shaped probe top. This signal is the basis for the digital signal.

B The binary signal is built on the basis of the threshold value phi_65. Above this threshold value steam will be assumed.

The application is possibly in transient (in this example) and stationary flows with a resolution of ca. 10^{-4} s. As the result a measuring signal by the post operating software module will be generated, which represents the local steam content. The influence of flow parameters may be lead to failures. That must be attend. The exact functionality of NSP is described in [1, 2, 3].

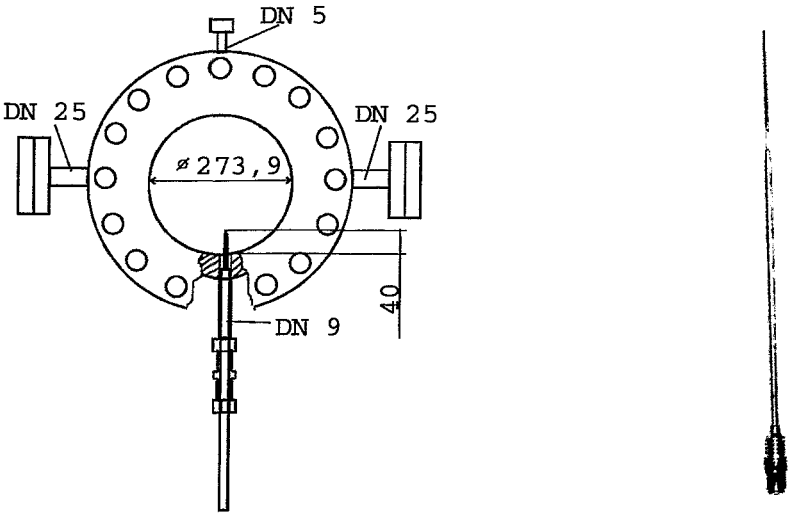

Fig. 5: Scheme of installation position of needle-shaped probes in the pressure vessel and a photo of it

Fig. 5 illustrates the installation position of the NSP's in the pressure vessel. The installation length amounts 40 mm within the vessel with an inner diameter of 273.9 mm. The diameter of probe top is 0.12 mm, and the length of contact is 0.3 mm.

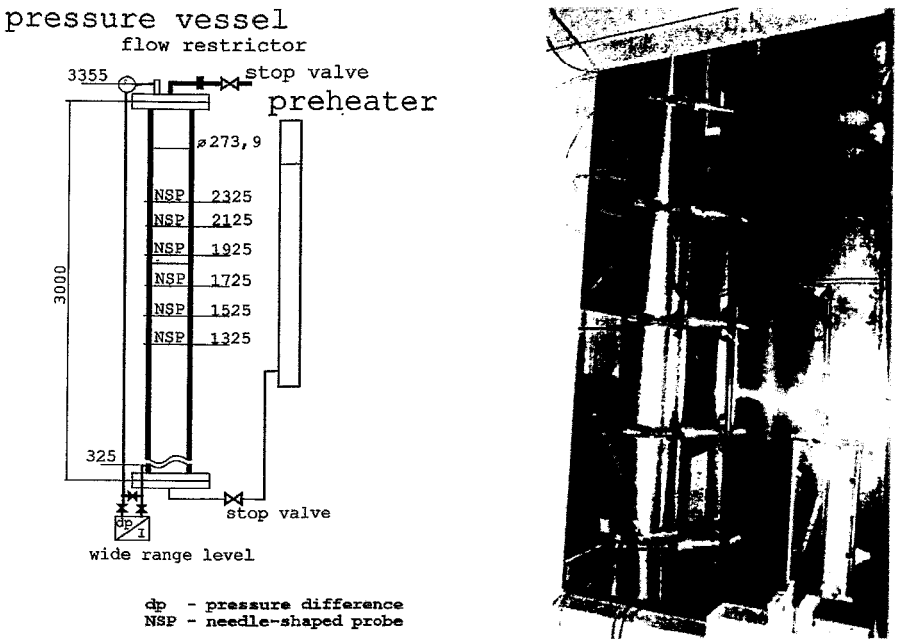

Fig. 6.: Principle scheme of test facility (pressure vessel and preheater) with axial distribution of NSP's and its photo

The NSP's are configured in the pressure vessel orthogonal to the flow path every 200 mm within a height of most likely range of mixture level (Fig. 6).

3 ATHLET-Code calculation of mixture level

This part of contribution deals with the calculation of mixture level by ATHLET-Code. At first, it is necessary to predefine the nodes in the pressure vessel, considering the configuration of measuring instrumentation. The code subdivides every predefined node in two homogeneous volumes:

⇒ one volume for water phase (below the mixture level)

⇒ one volume for steam phase (above the mixture level)

In Fig. 7 the nodalization scheme of pressure vessel is illustrated. The number of nodes over the whole vessel height of 3000 mm is 23. It is necessary to predefine small nodes at the NSP-positions to reproduce local parameters, like steam content at every measuring point. So the ATHLET-Code generates a local steam content at the NSP-position, which is comparable with the measured one by NSP. Thus, an adaptation to real circumstances is considered.

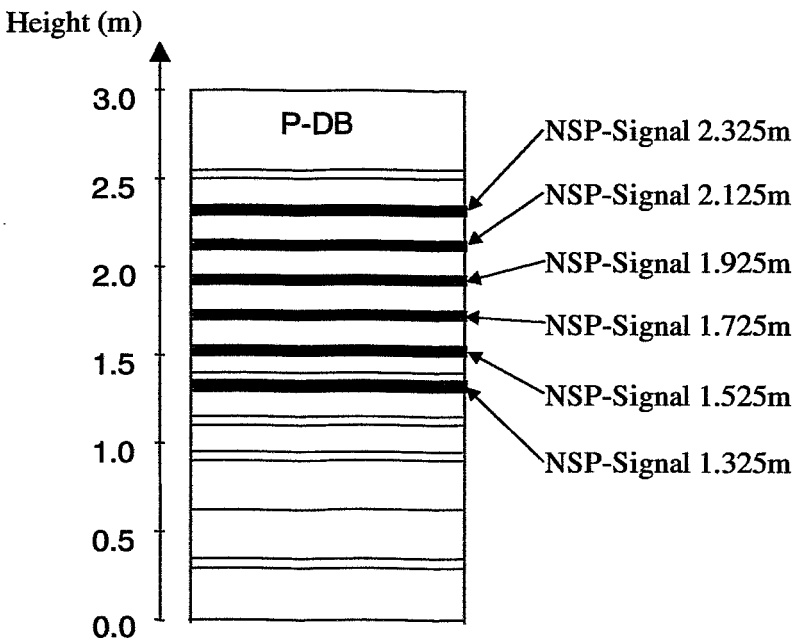

Fig. 7: Nodalization scheme of pressure vessel for ATHLET-Code

The next step is the calculation of mixture level height, which results from the volume-height-polygon formula corresponding to the volume below mixture level. That means, the water phase is the basis for the calculation of mixture level. The basic models for this are the lumped parameter models for different control volumes and flow track as well as drift flow models [5]. The specific characteristic of the ATHLET calculation is, that ATHLET assumes a plain surface of the mixture level without a foam zone in contrast to the experiment. The reality shows, that the surface of mixture level is moved and wavy with a foam zone in case of high transient evaporation process.

4 Evaluation of measured and calculated results

The following time responses of measured and calculated values will be compared for defined NSP-Position:

⇒ mixture level calculated by ATHLET (*ML-ATH*)

⇒ collapsed level calculated by ATHLET (*CL-ATH*) and measured by hydrostatic measuring system (*CL-EXP*)

⇒ local steam content measured by NSP (*PHI-65, PHI-65-MAV*)

⇒ local steam content calculated by ATHLET (*PHI-ATH*)

The PHI-65-MAV was built as moving average signal to reduce the stochastics of the needle-shaped probe signal.

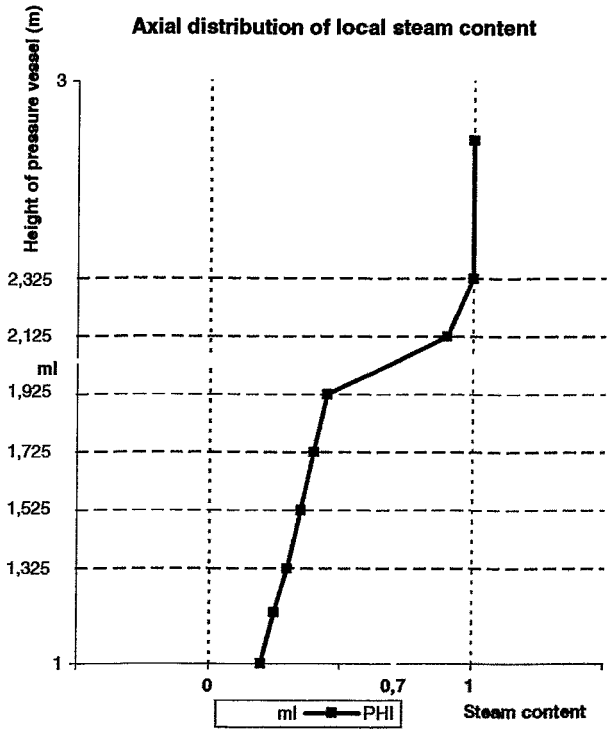

Fig. 8: Definition of mixture level depending on the axial distribution of local steam content

Fig . 8 illustrates the definition of mixture level depending on the axial distribution of local steam content. At the point, where the steam content crosses the value of PHI = 0.7 (70%), the mixture level was determined. The 70% value of steam content is the fixed threshold value, at which the experimental mixture level transfer is completed. So the 70% value signs a dominant phase changing. A continuous fluid phase does not longer there exists. It corresponds to the theoretical, by ATHLET-Code calculated steam content.

Fig. 9 shows the mixture level transfer calculated by ATHLET-Code and measured in experiment for the NSP-position 1.525 m. In the above part the water and mixture level response is illustrated. The part below includes steam content calculated by ATHLET-Code and measured by NSP. By the 70% value the intersection point with measured (by NSP) and calculated (by ATHLET-Code) local steam content is given.

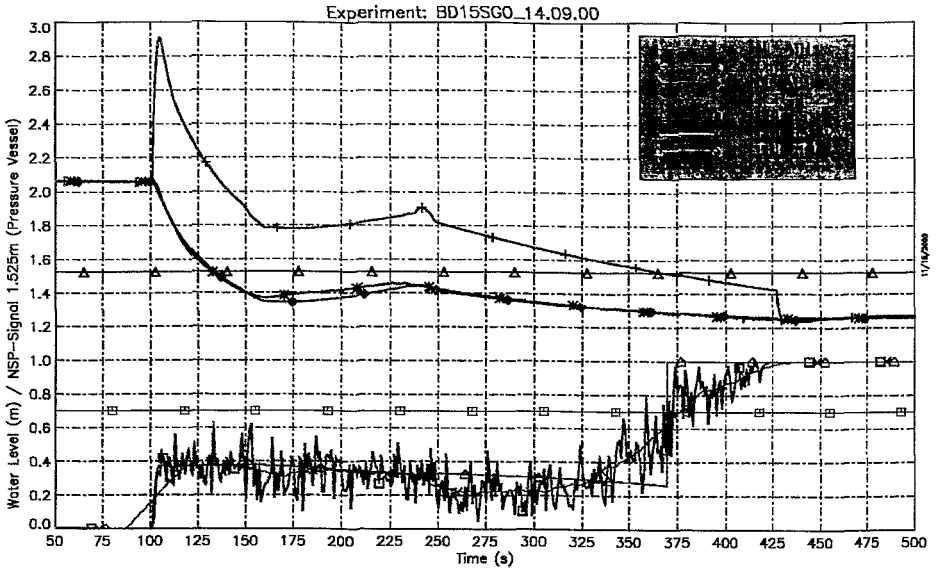

Fig. 9: Mixture level transfer given by time response of calculated mixture level (ATHLET-Code) and measured local steam content (experiment) NSP 1.525

The point of attention is the transfer region of mixture level, the differences between calculated and measured values. The theoretical, by ATHLET-Code calculated steam content, corresponds to the mixture level transfer. The difference between prompt jump of local steam content, calculated by ATHLET-Code and the gradual increasing of NSP-signal should be checked. The result of the investigation regarding the transfer region is, that the time difference between ATHLET-Code and NSP-signal is 5 s in maximum. This fact is very good to be seen in Fig. 10 with a zoom of the scale. There is drawn in a window of $\Delta t\_max = 5$ s over the transfer region. It shows the time difference of calculated mixture level transfer (above) and measured steam content (PHI-65), which passes the 70% value (below). The blue curve (NSP-BIN) represents the impulse rate, which is a measured result of the NSP, too (middle). Within the window, the end of the continuous fluid phase is indicated. This is reflected also by the PHI-65 signal in the parameter range of 70% steam content value. That denotes a process of the mixture level transfer with a foam zone.

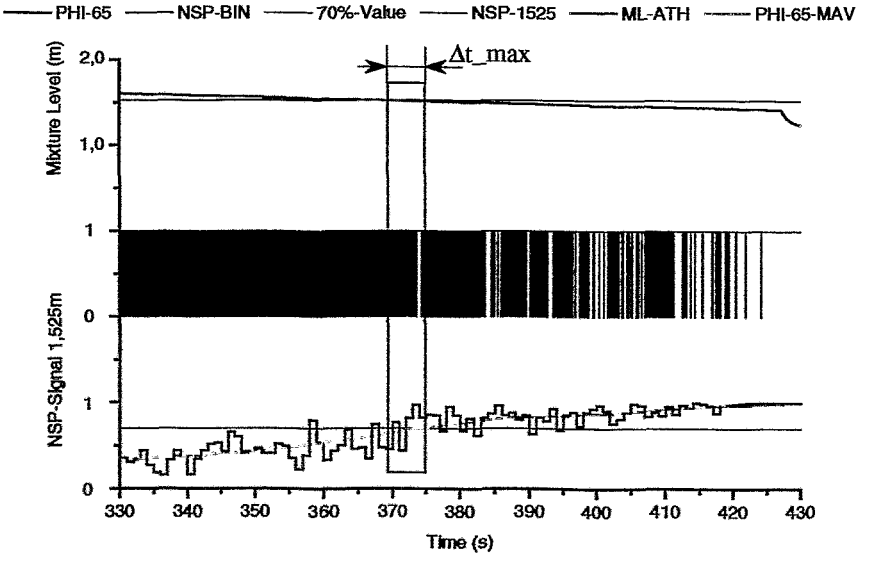

Fig. 10: Mixture level transfer and impulse rate (ATHLET-Code and experiment, NSP 1.525)

The equivalent results for NSP-Position 1.925 m are given in Fig. 11 and 12. There is reached a very good agreement between measured and calculated steam content at the local NSP-position, too.

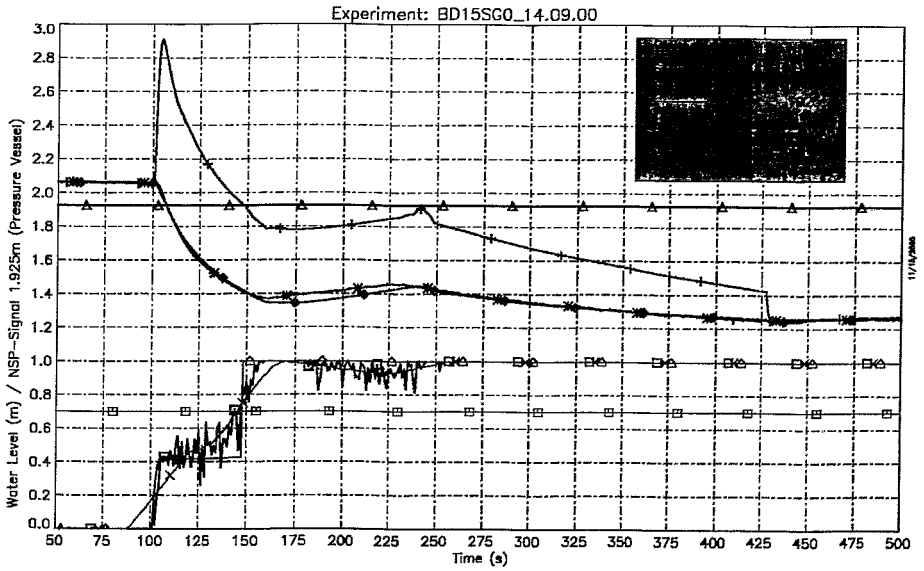

Fig. 11: Mixture level transfer given by time response of calculated mixture level (ATHLET-Code) and measured local steam content (experiment) NSP 1.925

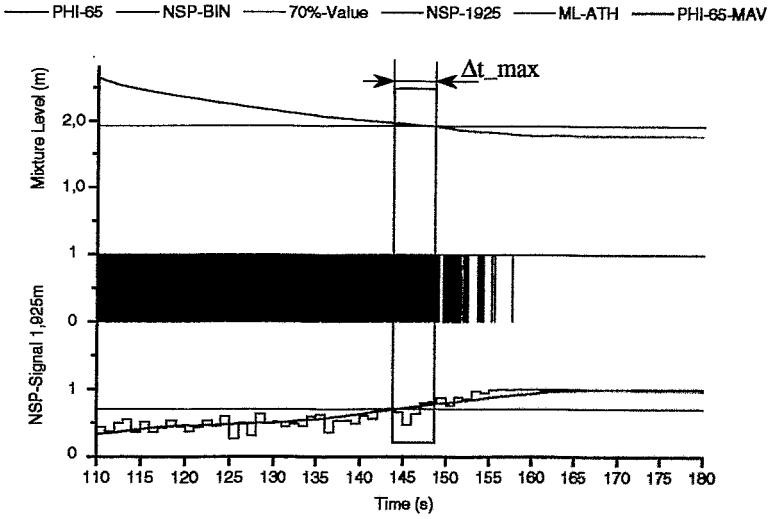

Fig. 12: Mixture level transfer and impulse rate (ATHLET-Code and experiment, NSP 1.925)

In Table 2 quantitative results of experiment and post-calculation are collected. For every NSP-position the time point of mixture level transfer will be confirmed. The formula for evaluating Δt_max is the following:

$$\Delta t\_max = PHI\_65\_MAV - PHI\_ATH \quad (1)$$

Equ. (1) determined the failure of mixture level between calculated and measured signals. The very good result, converted in deviation of mixture level height, is about 1 ... 8 cm. That is an absolute failure of 5% based on the difference of maximal increasing and final value of mixture level.

	PHI_ ATH (pass)	PHI_65 (pass)	PHI_65_ MAV (pass)	Δt_max	dml/dt (cm/s)
P1325	428 s	429 s	433 s	5 s	-7.7
Δml		8 cm			
P1525	370 s	373 s	375 s	5 s	-0.19
Δml		0.6 cm			
P1725	281 s	283 s	283 s	2 s	-0.33
Δml		0.7 cm			
P1925	148 s	148 s	145 s	3 s	-1.2
Δml		0 cm			
P2125	132 s	133 s	130 s	2 s	-1.5
Δml		1.5 cm			
P2325	122 s	124 s	120 s	2 s	-2.3
Δml		7 cm			

Table 2: Comparison of mixture level transfer for needle-shaped probe positions between experiment (PHI_65, PHI_65_MAV) and ATHLET-Code (PHI_ATH)

In Fig. 13 the mixture level transfer for all NSP-position (marked) in the pressure vessel is integrated. The NSP-signals are plotted for the parameter range 0 ... 1 at the NSP-position. The figure shows, that the good results corresponding to the mixture level transfer are valid for all needle-shaped probes at the 70% value.

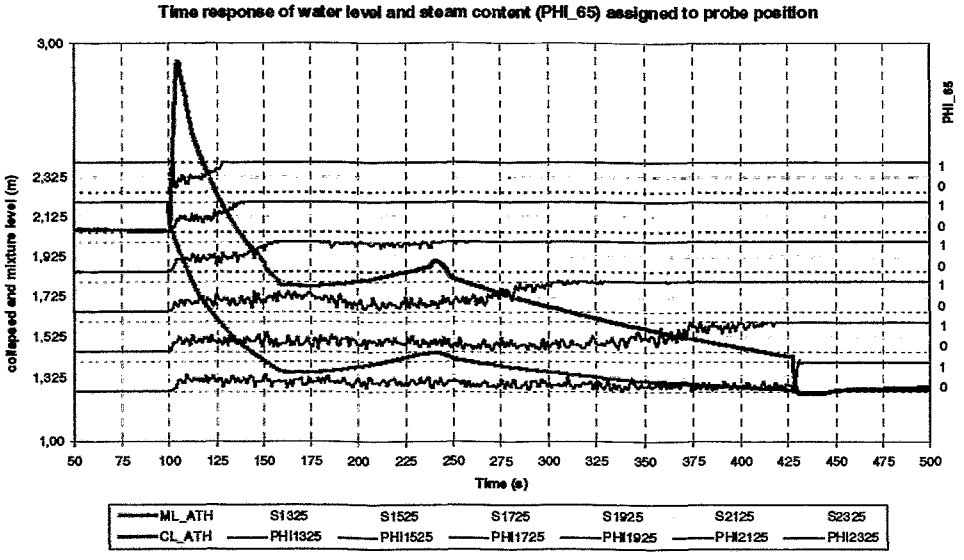

Fig.13: Mixture level transfer (ATHLET-Code and experiment) for all (6) needle-shaped probe positions in the pressure vessel

This fact will be pointed by the presentation in Fig. 14. Here is shown the axial distribution of local steam content in comparison to mixture level transfer at the needle-shaped probe positions scaled for defined points of investigation time. The slight curve of steam content is the measured value PHI-65, the thick one, PHI-ATH is the by ATHLET-Code calculated.

Especially the good correspondence between measured and calculated steam content and the change at the phase border (between 0 and 1) is demonstrated. For example at the time point t = 105 s, short after opening of leak, all NSP's are in the mixture (maximal increased value of mixture level). That means, during mixture level rapid increasing the measured and calculated result is an axial distribution of steam content with gradual increasing in the range of ca. 35-45%. The other axial distributions characterise the lay open of the NSP's corresponding to the mixture level transfer.

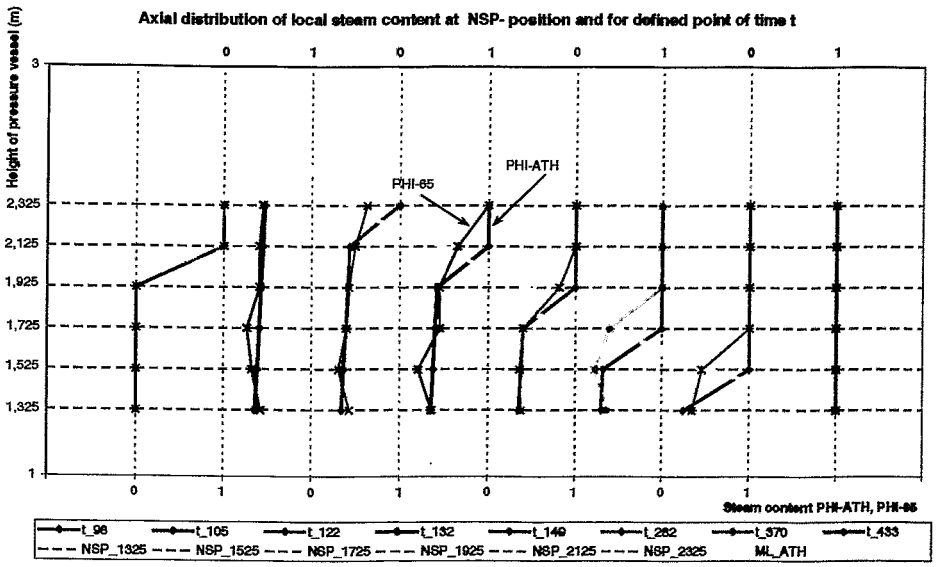

Fig. 14: Axial distribution of local steam content in comparison to mixture level transfer

In Fig. 15 the space curve of mixture level and the assignment of different phases of process state are described. The values absolute mixture level and its gradient are presented. It is to read off, with which gradient and which absolute height the mixture level passes the NSP-positions.

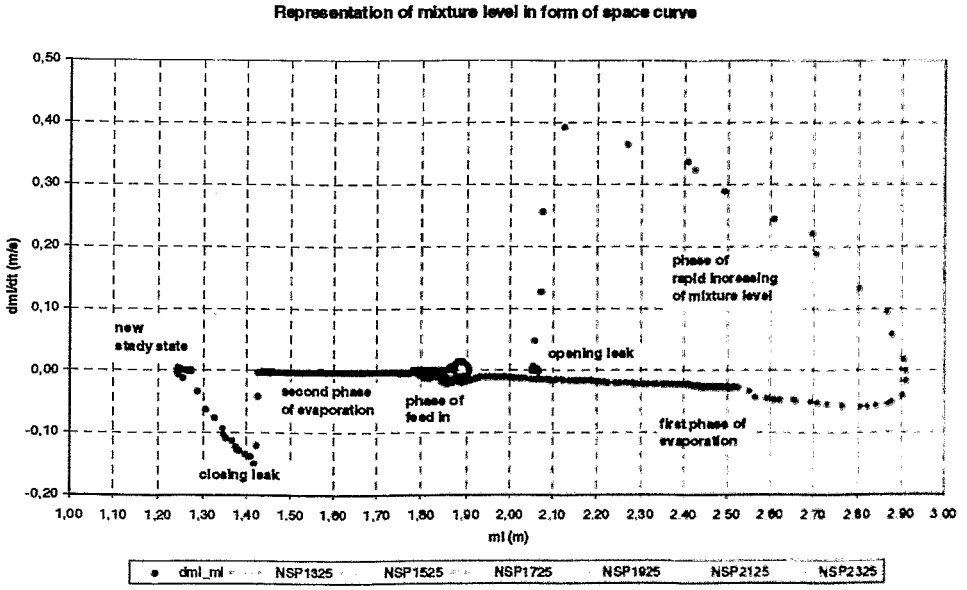

Fig. 15: Space curve of mixture level and assignment of different phases of process state

5 Conclusions

⇒ Needle-shaped probes are well qualified for

* detection of mixture level transfer,
* determination of local steam content.

⇒ A very good correspondence between local steam content calculated by ATHLET and determined by needle-shape probes was achieved.

⇒ Global parameter mixture level was verified by local values of steam content at NSP-positions.

⇒ The simulation program for thermal hydraulic processes in pressure vessels with water steam mixture (ATHLET-Code) was verified.

* That means a proof of iterative link of experiment and simulation.

⇒ Consequently it is possible to verify hydrostatic measuring systems.

The research work was sponsored within the reactor safety research programme (project number 150 12 04) by the Federal Ministry of Economics and Technology.

References

[1] Kern, T.:
Nadelförmige Leitfähigkeitssonden für die Charakterisierung von Schaum. Workshop „Meßtechnik für stationäre und transiente Mehrphasenströmungen", Rossendorf, Germany, 1998

[2] Fleischer, S; Hampel, R.:
Erfahrungen mit nadelförmigen Leitfähigkeitssonden zur Bestimmung von Parametern in Zweiphasenströmungen. Workshop „Meßtechnik für stationäre und transiente Mehrphasenströmungen", Rossendorf, Germany, 1997

[3] Prasser, H.-M.:
Leitfähigkeitssensoren für die Bestimmung von Parametern in einer Zweiphasenströmung. Workshop „Meßtechnik für stationäre und transiente Mehrphasenströmungen", Rossendorf, Germany, 1997

[4] ATHLET-Code Mod. 1.2 Cycle A. Program and User Manual. Gesellschaft für Anlagen- und Reaktorsicherheit (GRS) mbh Garching

[5] Steinhoff, F.:
Thermo- und Fluiddynamikmodelle im Rechenprogramm DRUFAN und im Nachfolgeprogramm ATHLET zur Simulation von Separationsvorgängen und Gemischspiegelbewegungen in vertikalen Strömungskanälen. Teil 1: Entwicklung der Modelle. GRS-A-1539, GRS mbh Garching, 1989

[6] Hampel, R.; u. a.:
Meß- und Automatisierungstechnik zur Störfallbeherrschung - Methoden der Signalverarbeitung, Simulation und Verifikation. Abschlußbericht BMBF-Projekt 150 10 15, HTWS Zittau/Görlitz (FH), 1999

A NEW ELECTRODE-MESH TOMOGRAPH FOR ADVANCED STUDIES ON BUBBLY FLOW CHARACTERISTICS

Steffen RICHTER

Tokyo Institute of Technology
2-12-1 Ohokayama, Meguro-ku, 152-8550 Tokyo, JAPAN
phone: 0081 – 3 – 5734 – 3063
FAX: 0081 – 3 – 5734 – 2959
richter@2phase.nr.titech.ac.jp

Masanori ARITOMI

Tokyo Institute of Technology
2-12-1 Ohokayama, Meguro-ku, 152-8550 Tokyo, JAPAN
phone: 0081 – 3 – 5734 – 3063
FAX: 0081 – 3 – 5734 – 2959
maritomi@nr.titech.ac.jp

Keywords: bubbly flow characteristics, conductive computer tomography, volume flow measurement

ABSTRACT

For studies on the characteristics of bubble flow in a rectangular channel (20x100mm) a new electrode-mesh tomograph have been applied. The measuring principle is based on local conductivity measurement. The applied sensor scans the local void fraction distribution in 2 parallel planes, separated 1.5mm in flow direction, with a resolution of 3.0x2.2mm and a overall sampling rate of 1200Hz (all 256 points). Algorithms for the calculation of the local instantaneous void fraction distribution and the true gas velocity are presented. Based on these values the approximate shape of bubbles was reconstructed and the gas volume flow through the sensor evaluated. The superficial gas velocity as well as the local distribution of the gas volume flux was calculated.
An extensive sensitivity study illustrating applicability and accuracy is presented, based on experimental observations as well as theoretical considerations.
The evaluated results are compared with high-speed video observations of the flow field as well as data comparing the reconstructed volume flow with measurements by a laminar flow meter. Good agreement can be stated in general.

INTRODUCTION

For design improvement of nuclear reactors as well as the assessment of their safety features advanced hydrodynamic computer codes have been developed. It is obvious that from the point of CFD code development, that there is the necessity to verify the developed models with high quality databases, which were obtained from experiments complementing the resolution of modern CFD codes in spatial and temporal concerns. Intensive studies on the sensitivity of all parameters will supply sufficient knowledge that allows to extrapolate data obtained from (scaled) experiments to the real facility as well as to assess the accuracy in the numerical prediction of the real facility's operation characteristics.
Considering the experimental part, several attempts have been made in the past to solve this problem. Remarkable results have been reached by the use of X-ray tomography, which is able to supply data with a resolution in the order of several millimeters and a temporal resolution in the order of some milliseconds. Cited should be Hori et al. [1] who realized a spatial resolution of approximately 2mm by an overall sampling rate of 2000Hz.
Beside of the cost-intensive X-ray technology, attempts have been made be use of intrusive sensors utilizing the measurement of the electrical conductivity. Besides many others, Prasser et al. [4], who used a sensor where 16x16 electrodes were arranged in 2 planes and a temporal resolution of 1024 Hz have been realized, should be cited [4], [5].
Since the approach done by Prasser et al. [4] was considered as outstanding by the authors in terms of temporal and spatial resolution, the aim has been to use this kind of sensor for studies on flow characteristics for bubbly flow in a comparatively narrow channel of 20x100mm cross-section. Beside the local, instantaneous void fraction distribution there have been particular interest in measuring the local true velocity of the dispersed phase, the approximate bubble size as well as their distributions and to calculate from the obtained data the superficial gas velocity as well as to conclude to the distribution of the volume flux.

SENSOR DESCRIPTION

The used sensor was developed and manufactured at the FZR Research Center Rossendorf, Institute of Safety Analysis, Dresden, Germany, and is similar to the device reported by Prasser et al. [4]. An illustration of the applied device is given by Fig.1.

Design

The electrode-mesh sensor, WMT, was designed to cover the entire channel cross-section of 20x100mm size. The normal vector on the cross-section and the channel length coordinate are parallel. 2x8x16 electrodes are spread out crosswise (90°) in 3 planes. Two planes, each containing 8 parallel equidistant electrodes, work as receiver planes, whereby one plane, centered between the two receiver planes, works as transmitter plane. Each plane is separated 1.5mm so that the measured conductivity is an integral value of the fluid properties in an ancient region around the crossing point along this 1.5mm separation distance of the electrodes. Due to the fact that the electrode planes are parallel arranged, two planes of measuring points result (up- and downstream the transmitter plane), where the conductivity of the fluid is evaluated at the coordinates (x_1,x_2). Since transmitter as well as receiver electrodes are arranged equidistantly, an effective spatial resolution of 2.2 x 6.1mm results. With a wire diameter of 0.1mm, a free cross-section of 96% remains. The sensor is mounted in flanges fitting the size of the experimental apparatus. An overall sampling rate of 1200Hz have been realized with the available hardware (1 sample = 2 measuring planes, each containing 128 measuring points).

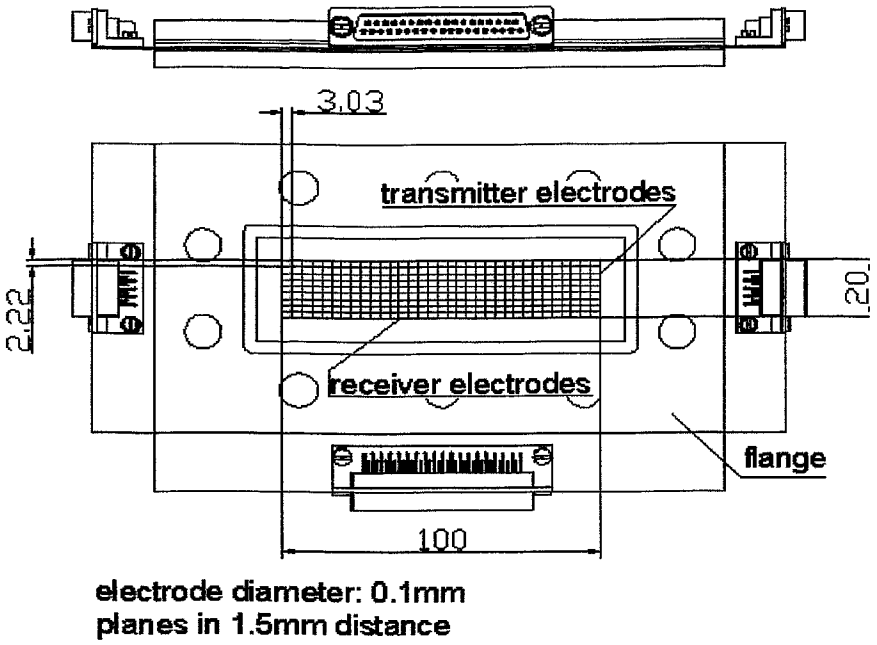

Figure 1 – Layout of the electrode-mesh tomograph, WMT

Control concept and signal acquisition

A simplified electric scheme of the WMT is illustrated in Fig.2. Transmitter wires are successively individually activated by a multiplex circuit closing the switches S1-S4. To avoid electrolysis the potential on the temporarily activated transmitting wire is inverted once in each half excitation-period by switching SP that yields a rectangular shaped supply voltage on the electrodes, as illustrated by U_{T2} in Fig.3. The excitation of a transmitter wire causes a current in the receiving wire (e.g. I_{R3} in Fig.3). Since all receiver wires are scanned separately, each crossing point of transmitter and receiver electrodes is scanned individually. The resulting current is transformed into voltage by operational amplifiers (R1-R4 in Fig.3) and kept by sample/hold circuits. To distinguish between the current that is caused by the influence of the capacity around the scanned crossing point and current that is a function of the local conductivity, the sample/hold circuits are released by the switch S/H after a stable voltage level is reached (Fig.3). The released signal is 12 bit AD converted and stored by a data acquisition computer.

The general possibility of cross-talk between the electrodes is avoided by applying an impedance to the output of the transmitters as well as the input of the receivers, significantly lower than the impedance of the fluid. This keeps the potential of all non-activated electrodes to zero [4]. A proposal by Prasser et al. [4] have been followed for the conversation from measured conductivity values to the local void fractions, assuming a linear dependency of the local void fraction from the conductivity in 1st order. So the instantaneous local void fraction $\varepsilon(t)$ at the point (x_1, x_2) writes for a constant current supplied by the amplifier, [4]:

$$\varepsilon(t)_{X1,X2} = \frac{(U_{el}(t))_{X1,X2} - (U_{el}(t)^W)_{X1,X2}}{(U_{el}(t)^A)_{X1,X2} - (U_{el}(t)^W)_{X1,X2}} \qquad (1)$$

The assumption of a linear dependency between the local void fraction and the induced current is a simplification used and has explicitly to be understood as approximation in 1st order. The obtained quality for void fraction measurements was found to be accurate by 1% in comparison to X-ray tomography [4]. To assure that the correct values for U_{el}^{A} and U_{el}^{W} are used (the case of only Air, Water, respectively), the sensor is calibrated before every experiment.

METHOD FOR FURTHER DATA PROCESSING

The measured void fraction writes in general form:

$$\varepsilon = \varepsilon(\vec{r},t) \qquad (2)$$

and is characterized by a spatial resolution of 2.2 x 6.1mm and a resolution in time of 0.83ms. It has been verified that the measured void fraction is within 1% exact [4]. Based thereon, the general possibility to obtain more advanced data of flow characteristics by use of the available sensor has been investigated. In particular, about the local true gas velocity as well as the possibility for spatial reconstruction of the flow field was thought. The study was limited to pure co-current bubbly flow of an air-water mixture at atmospheric pressure and ambient temperature. The superficial velocity of the water did not exceed 25cm/s and the geometry of the channel has been chosen to 20x100mm.

Local true gas velocity, Basic
The measurement of the local instantaneous true gas velocity is based on the analysis of the time a bubble migrates from one point on one measuring plane to the peripheral measuring point of the

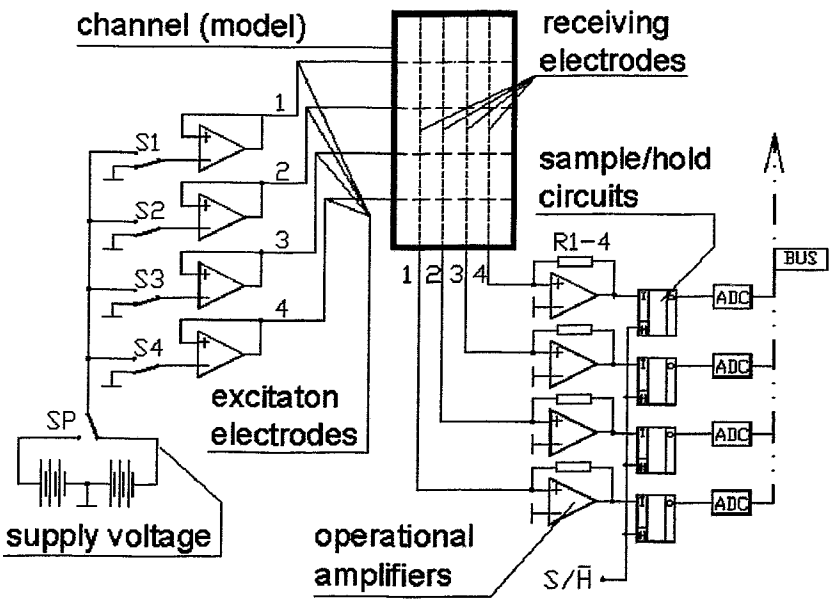

Figure 2 – Simplified electrical scheme, [5]

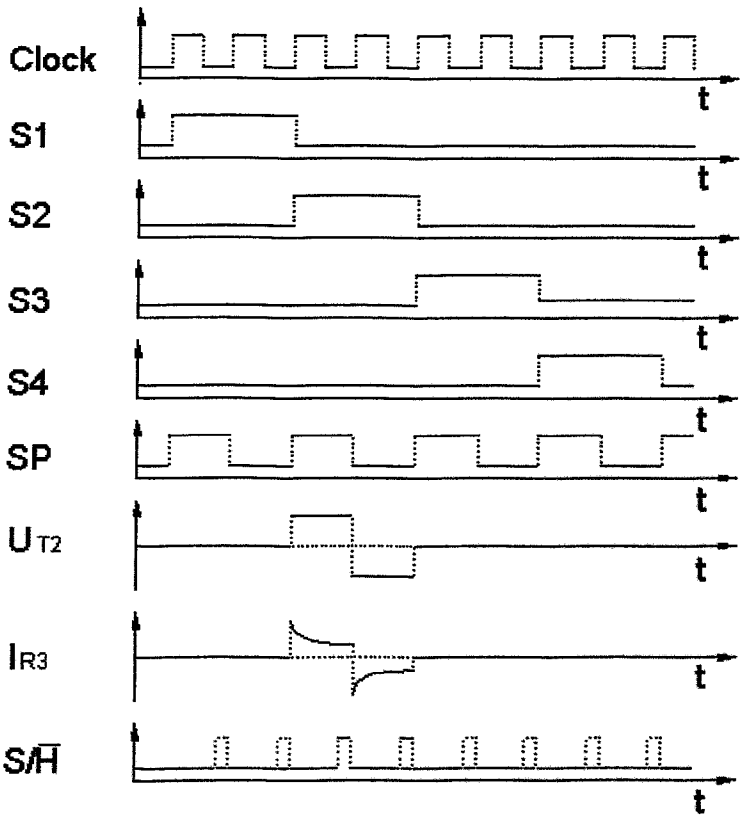

Figure 3 –Simplified control sequence, [5]

opposite plane.
If the bubble enters an ancient region around the crossing point, the (noise free) void fraction signal ε(t) changes from zero to a larger level, as illustrated by Fig.4. This ramp, $\Phi_{\varepsilon,pos}$, can be expressed at a point $\vec{r}$:

$$\Phi_{\varepsilon,pos}(\vec{r},t)=(\varepsilon(\vec{r},t)=0)\cap(\varepsilon(\vec{r},t+dt)>0) \quad (3)$$

So the velocity of the bubble is defined as the surface velocity of the approaching interfacial area. Considering also the negative ramp, $\Phi_{\varepsilon,neg}$, yields less accurate results. The reason is seen in a temporal alteration of the bubble shape by the wires, followed by a non-neglectable difference in between the surface velocity and the volume-averaged rising velocity. This explanation is confirmed by the void fraction course illustrated in Fig.4, where the signal obtained by the downstream plane II is slightly elongated. Due to the same fact, former approaches, utilizing a time correlation function for the evaluation of the local true gas velocity failed, since the character of bubble deformation is statistically not randomly distributed.

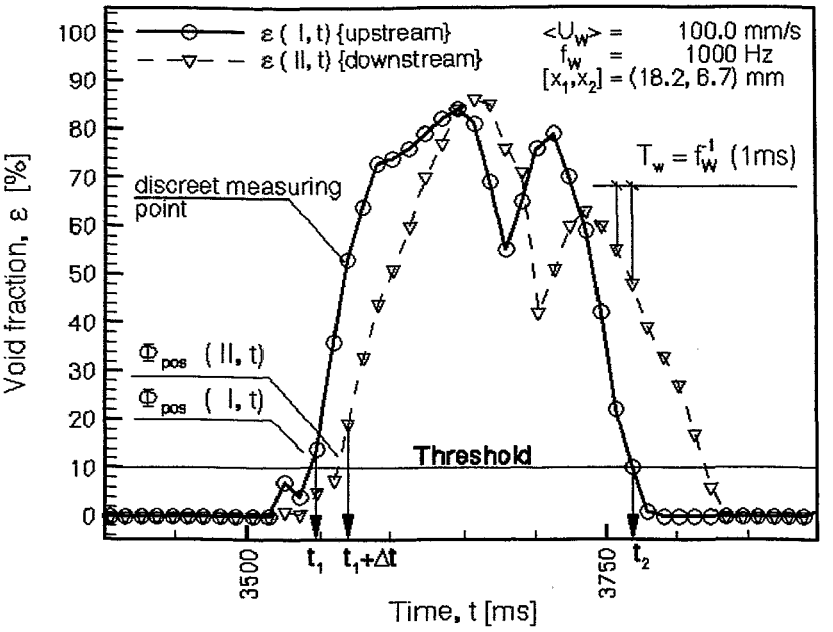

Figure 4 – Local void fraction signal

If two ramps Φ_ε occur, separated by the vector $\vec{s}$, the delay time Δt between these events allows concluding the average surface velocity within the distance $|\vec{s}|$:

$$\Delta t:\Phi_{\varepsilon,pos}(\vec{r},t)\cap\Phi_{\varepsilon,pos}(\vec{r}+\vec{s},t+\Delta t) \quad (4)$$

To ensure that identified ramp events result from the migration of one and the same continuously by the gaseous phase occupied volume, Eq.(4) have been extended:

$$\Delta t:\Phi_{\varepsilon,pos}(\vec{r},t)\cap\Phi_{\varepsilon,pos}(\vec{r}+\vec{s},t+\Delta t) \cap[\varepsilon(\vec{r},t+\delta t)>0:\delta t\in[0,\Delta t]] \quad (5)$$

The use of the delay time Δt for the evaluation of the surface velocity u in the described way implies that there is a maximum measurable velocity u_{max} for an overall sampling frequency f_W and the distance between the measuring planes Δ_W :

$$u_{max}=\Delta_W\cdot f_W \quad (6)$$

Any object moving faster than u_{max} and large enough to be detected by both measuring planes would be identified

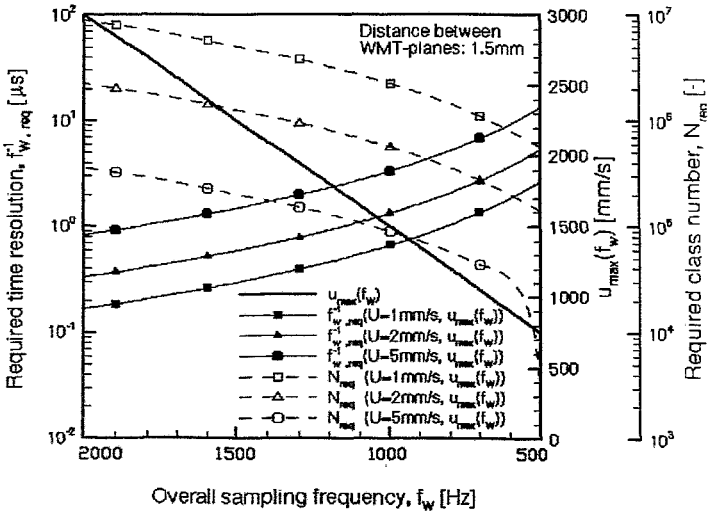

Figure 5 – Comparison, realized and required temporal resolution

as migrating with the maximum velocity u_{max}. Slower objects yield a measurable delay time that can be expressed in terms of delay frames δ (i.e. number of overall samples):

$$u_\delta = \frac{\Delta_W \cdot f_W}{\delta} \tag{7}$$

, which is characterized by a measuring uncertainty between u_δ and $u_{\delta+1}$:

$$U_\delta = \frac{\Delta_W \cdot f_W}{\delta(\delta+1)} \tag{8}$$

The true velocity u: $u_\delta < u \leq u_{\delta+1}$ remains unknown. Further it is obviously that the p.d.f. for the delay-time appears algebraically stretched if it is plotted over velocity arguments. In Fig.5 a comparison between the realized overall sampling frequency f_W, the corresponding maximal measurable velocity u_{max} and the required time resolution $f_{W,req}^{-1}$ is shown for aimed uncertainties in the velocity evaluation U_δ of 1,2 and 5mm/s. The graph proceeds assumes Δ_W = 1.5mm. Obviously, the required temporal resolution f_W is about 1 order higher for a given maximum velocity u_{max} than the present available hardware is able to realize.
However, considering the mentioned uncertainty in the velocity evaluation with mathematical rigor besides the feature being able to supply detailed information about the instantaneous void fraction distribution were promising enough to make an approach toward the defined aim.

Local true gas velocity, Approach
In general, the statistical characteristic of the delay time Δt between two (positive) ramp events $\Phi_{\varepsilon,pos}(\vec{r},t)$ and $\Phi_{\varepsilon,pos}(\vec{r}+\vec{s},t+\Delta t)$ are determined by a p.d.f. p_T:

$$p_T = \frac{\partial P(\Delta t < T)}{\partial \Delta t} \tag{9}$$

Sufficient high time resolution supposed, the delay-time mean value $E(\Delta t)$ gives directly the statistically expected velocity of the gaseous phase E(U), corresponding to a velocity oriented p.d.f.: p_u.
The uncertainty in the velocity measurement, Eq.(8), yields that evaluated velocities u: $u_\delta < u \leq u_{\delta+1}$ are accumulated at the measurable velocities $u_{\delta+1}$. However, the number of detected events belonging to a velocity class U_δ , as defined by Eq.(8), is constant, independent if all events appears to be accumulated at a velocity u_δ within U_δ or if they are distributed by a distribution function $\tilde{\tilde{p}}_u$ over U_δ. With the discreet distribution function $\tilde{\tilde{p}}_u$ (which is sufficient to serve the requirements in time-resolution and normalized in U_δ), the velocity distribution function p_u can be replaced by a new distribution function $\tilde{p}_u$. The probability P(Δt<T), or correspondingly 1-P(u<U), can so be expressed either by the measurable velocity classes U_δ or by the redistributed one, $\tilde{U}_i$:

$$\sum_{\{\delta\}} p_{u\delta} U_\delta = \sum_{\{j\}} \tilde{p}_{uj} \tilde{U}_j = \sum_{\{\delta\}} \sum_{\{k\}} \tilde{\tilde{p}}_{uk} p_{u\delta} U_\delta \tag{10}$$

with:

$$\sum_{\{\delta\}} U_\delta = \sum_{\{j\}} \tilde{U}_j \tag{11}$$

The spectrum of local gas velocities in bubbly flow does not show any singularities and behaves smooth since the velocity fluctuation of a single bubble around the time averaged value have been found as distributed with a steady, "sufficient smooth" function, [2],[3],[6]. Facing this point, an approach in 1st order can be legitimized by assuming that the frequency of all true velocities u within one measurable velocity class U_δ are equally distributed and so $\tilde{\tilde{p}}_u$ is constant over U_δ. The introduced p.d.f. $\tilde{\tilde{p}}_u$ is normalized within U_δ:

$$\sum_{\{U_\delta\}} \tilde{\tilde{p}}_{uk} = 1 \tag{12}$$

The redistribution of the N_δ velocity classes that are larger in class-width U_δ than the required class-width $\tilde{U}_k$ writes for temporal equidistant sampling cycles δ:

$$N_\delta < N_j : p_{u\delta} U_\delta = p_{u\delta} \sum_{\{k\}} \tilde{\tilde{p}}_{uk} \tilde{U}_k \tag{13}$$

With:

$$U_\delta = \sum_{\{k\}} \tilde{U}_k \tag{14}$$

The statistical moments are altered slightly if an assumption for the statistical behavior of the bubble rising velocities within the uncertainty is made by introduction of $\tilde{\tilde{p}}_u$. The mean value E(u) and the standard deviation $D^2(u)$ are of particular interest:

$$\mathrm{E}(u) = \int_{u=0}^{\infty} u \cdot f(u) du = \sum_{j=1}^{\infty} \tilde{p}_{Uj} \cdot \tilde{U}_j \tag{15}$$

$$\mathrm{D}^2(u) = \int_{u=0}^{\infty} (U - \mathrm{E}(u))^2 f(u) du = \sum_{j=1}^{\infty} \tilde{p}_{Uj} \left(\tilde{U}_i - \mathrm{E}(u)\right)^2 \tag{16}$$

The results obtained by application of the proposed algorithm are discussed in the section 'Test results and comparison'.

Phase reconstruction

The algorithm for the velocity evaluation supplies information about the statistically expected local true gas velocities in a two-phase mixture. Simultaneously, the local void fraction is measured.

With these information an approximate reconstruction of the bubble shape and its volume can be carried out. This idea has been first reported by Prasser et al. [4] and is based on the localization of a volume continuously filled with gas, which is appropriately clustered.

The algorithm proposed by Prasser et al. [4] has the disadvantage that the volumetric flux is supposed to be constant over the cross section. This simplification is not further necessary since the local instantaneous true gas velocity, u_G, is known, Eqs.(9)-(16).

To evaluate the area in A_c, which is occupied at a certain time by the gaseous phase, and to repeat the process for all t till the entire structure in the $\varepsilon(x_1,x_2,t)$-field is clustered, a list Lε is introduced:

$$\mathrm{L}\varepsilon = [\varepsilon(\vec{r}_1,t_1), \varepsilon(\vec{r}_2,t_2), \ldots, \varepsilon(\vec{r}_n,t_n)]^T = [\varepsilon((x_1,x_2)_1,t_1), \varepsilon((x_1,x_2)_2,t_2), \ldots, \varepsilon((x_1,x_2)_n,t_n)]^T \tag{17}$$

This list Lε, given by Eq.(17), contains all local instantaneously measured values of the void fraction resulting from the same bubble structure. It have been found by extensive studies on single bubbles and bubble collectives that there exists a unique value of ε, ε_{thresh}, which is a certain identifier that a gas structure is in between these points. The value is independent from the cross-sectional averaged void fraction and slightly altered by bubble rising velocity (+/-5% for rising velocities between 200~500mm/s). This threshold have been set to ε_{thresh}=10% and is kept constant for every flow condition. The void fraction signal have been triggered by ε_{thresh} and in the following only this triggered signal, noted with ε, is considered. So it has been avoided to jump during the scan procedure from one bubble to the next, except for situation where two bubble are shortly before coalescence, which corresponds to a local void fraction of significantly more than 10%. A qualitative criteria to assess, if a certain instantaneous void fraction distribution over A_c is caused either by 2 small bubbles, which are closed before coalition, or by 1 larger structure have been found: If the clustered $\varepsilon(x_1,x_2,t)$-field shows more than one local maximum, it is supposed that there exist more than a single bubble. This case is only important for the correct evaluation of the bubble diameter. The local gas volume flux distribution is not influenced. The proposed utilized clustering procedure can be expressed by the recursive-implemented formula noted below:

$$L\varepsilon_i^{k+1}\begin{pmatrix}\tilde{x}_1\\ \tilde{x}_2\\ \tilde{t}\end{pmatrix} := \bigvee_{m=0}^{1}:\bigvee_{n=0}^{1}:\bigvee_{o=0}^{1}:L\varepsilon_j^k\begin{pmatrix}x_1+1-2m\\ x_2+1-2n\\ t+1-2o\end{pmatrix} > 0 \cap L\varepsilon_i^{k+1} \notin L\varepsilon_l^{\kappa} : \kappa \in [0,k+1] \tag{18}$$

The points in the $\varepsilon(x_1,x_2,t)$-field are scanned at the step k+1 by application of a 6-point stencil to all points in the list $L\varepsilon^k$, while checking if the identified new points ($\varepsilon>0$) had been scanned by a former step. The procedure is repeated till the successor of the last lists remains empty. With the information about the integral void fraction of a bubble, scanned in the $\varepsilon(x_1,x_2,t)$-field by Eq.(18), with the expected value of the rising velocity of this structure, Eq.(5), and with the spatial resolution of the sensor, Δx_1, Δx_2, the bubble volume V_B^0 writes at physical standard condition for p^0, T^0:

$$V_B^0 = \frac{p}{p^0}\frac{T^0}{T}\Delta x_1 \Delta x_2 \cdot \Delta_W \cdot \sum_{\{V_B\}} \varepsilon \cdot \left| \frac{1}{\delta} + \int_{T_{\delta-1}}^{T_\delta} \tilde{\tilde{p}} dt \right| = \frac{p}{p^0}\frac{T^0}{T}\Delta x_1 \Delta x_2 \cdot \Delta_W \cdot \sum_{\{V_B\}} \varepsilon \cdot \left| \frac{1}{\delta} + \frac{1}{2\delta(\delta+1)} \right| \tag{19}$$

It has to be noted that the first formulation of the bubble volume is of general validity. The second line is based on the assumption that $\tilde{\tilde{p}}_u$ is constant distributed over the velocity class U_δ, yielding that the mean value is given by $u_\delta + 0.5\, U_\delta$. For any approximation of the velocity distribution within a measurable class-width U_δ higher in order the first line of Eq.(19) has to be considered. The presented research work concentrates on two-phase bubbly flow, where bubbles are ranging in diameter between 4~7mm. These bubbles are under experimental conditions spherical or show only a slight tendency for ellipsoidal distortion (lg(Mo)~-14,Eo~1). The volume V_B^0 at standard conditions has been expressed by the diameter d_B, supposing a spherical shape (notation: $d_{B,sph}$). A distribution function f_B is introduced by Eq.(20) that allows to calculate the expected bubble diameter $E(d_{B,sph})$ at (x_1,x_2):

$$f_B(d_{B,sph}) = \left[\frac{\partial P(d_{B,sph} < D_B)}{\partial d_{B,sph}} \right] \tag{20}$$

The local gas volume flux can be evaluated from information about local instantaneous true gas velocity and simultaneous measured void fraction by Eq.(21):

$$< u_G > (x_1,x_2) = \varepsilon(x_1,x_2,t) \cdot u_G(\varepsilon(x_1,x_2,t)) \tag{21}$$

TEST FACILITY

The electrode-mesh tomograph (Fig.1) has been applied for studies on developing co-current bubbly flow at atmospheric conditions, realized with the test facility that is illustrated by Fig.6.

The rectangular channel (2) has a cross-section of 20x100mm over the entire length of about 55 hydraulic equivalent diameter. The channel is made from acrylic glass and modular in design, so that the WMT (3) can be set at locations every 100mm downstream the strainer unit (4).

The channel is supplied with water from a lower plenum (6) that is flooded by a circular drilled distribution pipe. Water is accelerated through a 3-dimensional shaped inlet nozzle, which is followed downstream by a strainer unit (5). The strainer unit (5) consists of blades with 0.8mm thickness, fixed in 5mm distance, aiming a homogenization of the velocity profile in x_1, x_2 direction. Also contained in the strainer unit (6), there is a sieve for turbulence profile equalization (stainless-steel wire-mesh, 0.5mm mesh size, 1.5 hydraulic diameter downstream the strainer-blades).

Air is injected through steel needles, which are supplied through the channel wall of the air injection unit (4), 110mm downstream the turbulence sieve. The needles have an outer diameter of 2mm and a precisely drilled hole of 1.0mm diameter in their wall, pointing in x_3 direction (i.e. main flow direction). The needles are inserted into the channel through steel-sockets, which are mounted at the wall and fit the size of the air injection needles perfectly. The surface inside the channel as well as of the air injection needles is absolutely planar and smooth. The connection between air injection needles and sockets is sealed outside the channel by use of a rubber package that allows a positioning of the air injection needle with about 1mm accuracy in x_1-direction. The closest distance of the air injection hole to the wall is also approximately 1mm. There are 5 sockets in x_2-direction mounted at the channel wall at x_2=10,30,50,70 and 90mm on each side of the channel wall. The outlet of the testing-channel was realized as an upper plenum (1) consisting of a diffuser and two suction pipes. The suction

pipes are 1" in diameter and adjustable in their height in order to optimize the run-off condition. Water flows from the upper plenum (1) into a container (13) by gravity. The storage container (13) is used to separate the head for the centrifugal-pump (16) hydraulically from the outlet-condition of the channel to avoid pressure oscillations.

Water volume flow is controlled by use of two parallel switched control valves (9), sized 1:10 in their nominal flow rate. The pressure upstream the control valve block (9) is kept constant by an overflow pressure regulator (12). The flow rate is measured by a 2-stage orifice cascade (8). The flow rate can be detected with average accuracy of approximately 2.5%. It is possible to keep the flow rate constant over the test series within about 1% shift.

The air for bubble generation was supplied by an oil-free piston compressor (15). In order to avoid pressure fluctuations, a pressurized vessel (14) have been utilized. To keep the air pressure upstream the control valves (10) constant a pressure regulator (11) have been installed. The control valves block consists of 2 parallel needle valves, sized 1:10 in their nominal flow rate. The flow rate of the air is measured upstream the control valves in a zone of constant pressure by use of a laminar-flow-meter. The volume flow can be detected with approximately 1.5% accuracy in average. The amount of air is sufficient to realize superficial velocities of up to 5cm/s.

During all experiments referred, the electrode-mesh sensor have been installed 580mm downstream the strainer unit (6), i.e. 470mm downstream the injection needles.

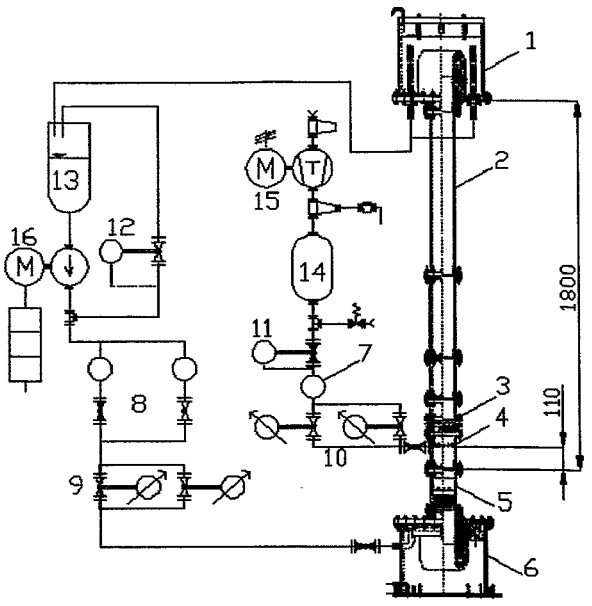

Figure 6 – Test facility

Table 1 Experimental conditions.

		Series No.1	Series No.2
Injection needle coordinates in (x_1,x_2)	[mm]	[(10,10),(10,30),(10,50),(10,70),(10,90)]	[(10,10),(10,30)]
WMT position downstream strainer	[mm]	480	480
Applied overall sampling rates, f_W	[Hz]	500, 800, 1000, 1200	500, 800, 1000, 1200
Superficial velocity range, gas, $<U_G>$	[mm/s]	0.5 .. 10.0	0.5 .. 10.0
Superficial velocity range, water, $<U_W>$	[mm/s]	0 .. 200	0 .. 200

RESULTS AND DISCUSSION

The verification of the proposed methods was carried out by use of extensive testing series: a first one to study the general void fraction measurement according the proposal by Prasser at al. [4], aiming the localization of a single bubble as well as studies on the probability distribution of the void fraction. Based on this elementary study, the validity of the proposed method for the evaluation of the local true gas velocity has been investigated in comparison with video data. Finally, the obtained data for the local true gas velocity the flow field were reconstructed in space, the volume flow was calculated and compared to values, alternatively supplied by a laminar flow meter, LFM.

Table 1 gives an illustration over the experimental settings used in the third and below discussed series.

Sparkling experiments

Aim was to clarify the order the noise level in the signal have to be imagined as well as to study its dependency from superficial gas and liquid velocities. Furthermore the necessary sampling duration should had been investigated in order to ensure a predefined certainty for the evaluation of various mean values.

A typical void fraction probability function is illustrated in Fig.7. The superficial velocity of the gas was $<U_G>$=2.1mm/s and the superficial liquid velocity was $<U_W>$=100.0mm/s with an overall sampling rate of

f_W=1000Hz. A log-log plot has been chosen to enlarge the area of low void fractions. It is obvious that the entire p.d.f. is characterized by 2 zones (Fig.7): Void fraction level lower 7% occur often, independent from the measuring point. This region is supposed to result from the action of different electromagnetic fields around the sensor. The signal is identical with signals measured during a single-phase experiment. The value of ε=7% was found as almost independent from <ε> and f_W. The second zone in Fig.7 can be identified by the field that is approximately equally distributed at void fraction values higher 7%. The minimum for the PDF level of $p_\varepsilon=10^{-4}$ results from 10.000 sampled data-points. Maximum reached void fractions are in the order of 70~80%. The shape of this field has been found as slightly dependent on <ε>. Large values of <ε> yield higher void fractions (ε_{max}=70-80%). The reason therefore is seen in a reduction in lateral mobility of bubbles, so that they were forced more a more in an ancient region of the wires.

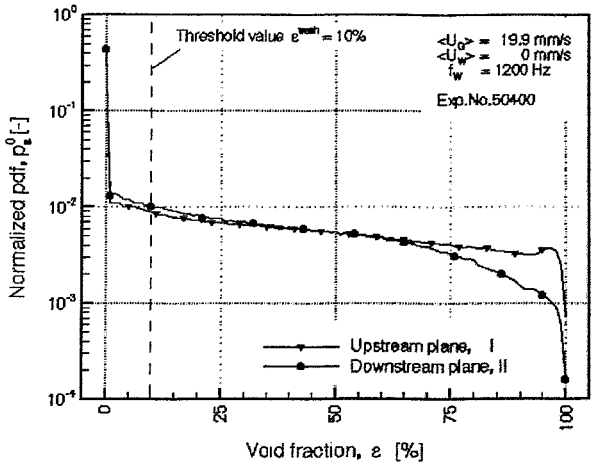

Figure 7 – Void fraction frequencies

The influence of the sampling number on the calculation of mean values has been investigated. For this purpose the behavior of the void fraction and true bubble rising velocity mean values, calculated by use of the above-introduced algorithms, have been studied. The deviation of the superficial mean value, achieved with a limited sampling number from the true mean value, which is given per definition for $t \rightarrow \infty$ and have been realized by analysis of a sliding, is plotted in Fig.8 for a wide range of flow condition. It can be seen that the relative difference between the calculated values for ε and $\langle U_G \rangle_G$ and the values, achieved by a limited sampling duration, falls to a certain level lower than 1% and remains oscillating for increasing time. In the case of high superficial gas velocity, the sampling number depending mean values of the local void fraction oscillates with about 0.5% around the "true" on. Lower superficial gas velocities yield an oscillation free convergence. The behavior of the mean value for the true gas velocity seems to be less depending on the cross sectional void, since -independent from the flow condition- all mean values oscillates for long time with an amplitude of about 0.25%.

Based on this investigation, the minimal sampling duration has been fixed appropriately in order to ensure a certainty in the measured value of more than 99%. Since data for the void fraction are locally and time dependent available, graphs can be provided for the instantaneous and the time averaged void fraction distribution. An example of the local time-averaged void fraction distribution is given in Fig.9 (non-symmetric air injection, Series No.2 in Table 1, $\langle U_G \rangle$=2.1mm/s, $\langle U_W \rangle$=100.0mm/s, f_W=1000Hz). At the channel walls the void fraction is naturally zero. A significant maximum of the void fraction (ε~6%) on the left-hand-side can be seen, corresponding with the locations of the air injection needles.

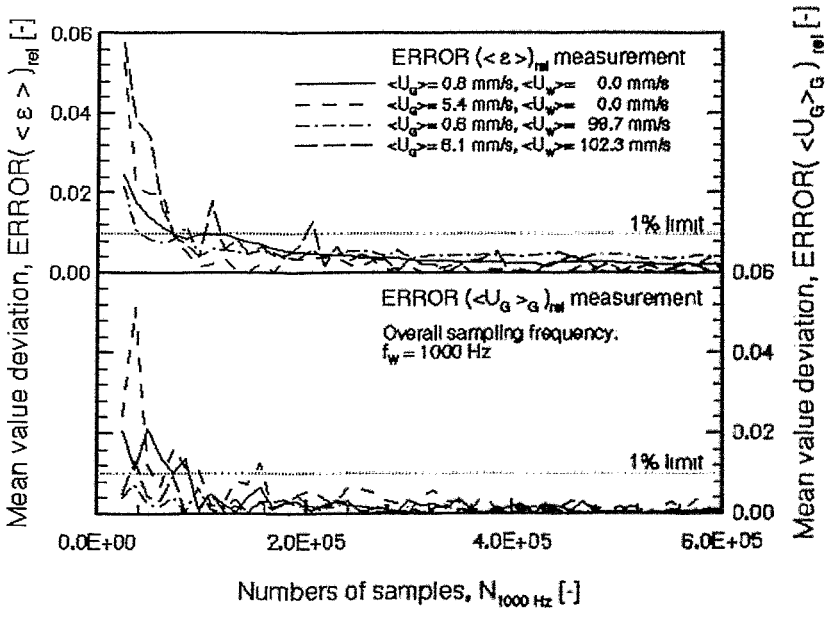

Figure 8 – Certainty in prediction of statistical momentum

Velocity measurement

The evaluation of the local true gas velocity has been carried out according Eqs.(4)-(15). Single bubbles as well as collectives of them were sparkled into the channel. The bubbles had a diameter of approximately 2~7mm. The data supplied by the WMT have been analyzed in order to obtain the delay time distribution Eq.(9). An example is shown in Fig.8 ($<U_G>$=2.1mm/s, $<U_W>$=100.0mm/s and f_W=1000Hz). The discreet function p_t is plotted over the logarithmic stretched arguments (classes T_i) in order to obtain equidistant velocity classes. The delay-time based p.d.f., according Eq.(9), have been redistributed by Eqs.(10)-(13). The obtained velocity classes are equidistant and plotted in the lower half of Fig.10. The arguments U_i are corresponding to the delay-time classes T_i used for the plot in the upper half of Fig.10. It can be seen that the velocity based function p_u is flatter than p_t in a region of high velocities. In an area of low velocities, the function p_u reaches higher level than p_t – a result of the summation of delay time classes T_i that belong to the same velocity class U_i.

Mean values for true gas velocities at different flow condition measured by the WMT, $U_{G,WMT}$, are plotted vs. the velocities $U_{G,video}$, obtained by the Video Image Processing Technique in Fig.11 for U_G=200-450mm/s and f_W as parameter.

There is a general good agreement of all data. Higher true gas velocities U_G scatter more. For data obtained with $f_W \geq 1000$Hz agreement can be confirmed within a 5% margin.. A sampling rates of lower than 800Hz have to be considered as insufficient for velocity evaluation in the studied parameter range.

In Fig.11 the uncertainty-bars for some of the measured velocity values are shown (standard deviation of u_G, $D(u_G)$). The order is 5-10% of the indicated bubble rising velocity U_G. The video measured data and the values predicted by the WMT are of same order. The quality of the velocity distribution approximation by introduction of the interclass distribution function $\tilde{\tilde{p}}_u$ in 1st order can be stated as good. An illustration of further measurement possibilities is given by Fig.12, where velocity data of an experiment with $<U_G>$=2.1mm/s and $<U_W>$=100.0mm/s are shown for a non-symmetric gas injection (series No.2 according Table 1). To give a realistic picture of the gas velocity distribution, the bubble repetition frequency has to be shown in the diagram, as well. By doing so it can be distinguished clearly, if the expected interval wherein the

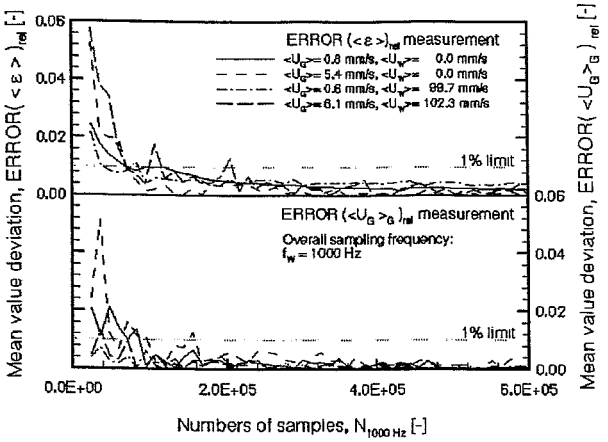

Figure 9 – Time averaged void fraction

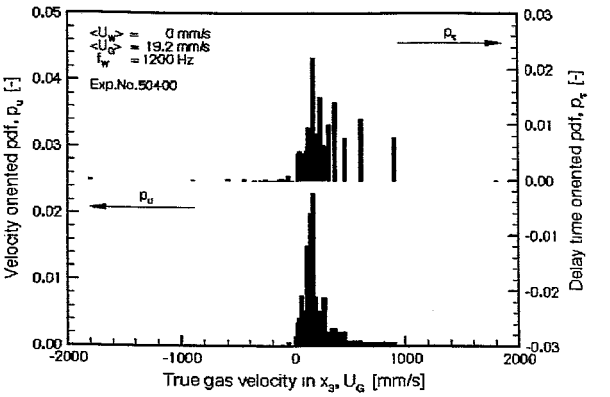

Figure 10 – Delay time p.d.f., measured and corrected

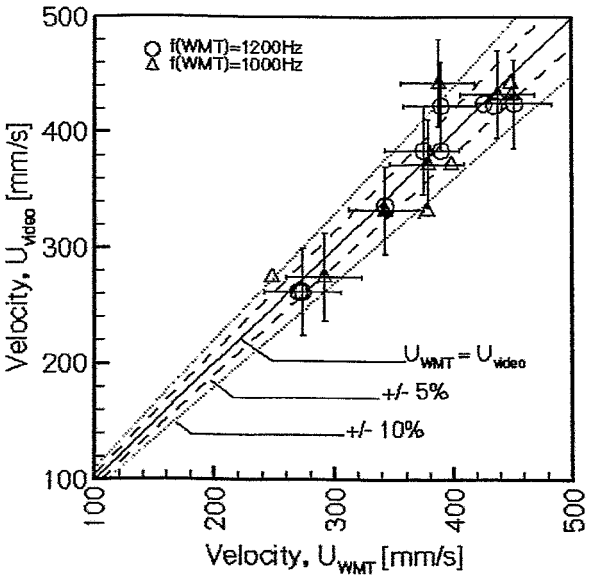

Figure 11- Quality of $U_{G,G}$ evaluation

velocity will range is due to a real physical behavior (i.e. action of turbulence), or due to a limited number of available data.

Bubble diameter and volume flow

With the evaluated information about the local instantaneous gas velocity, there is the possibility of bubble volume reconstruction, as demonstrated by Eqs.(17)-(19). With the assumption that the bubble shape is approximately spherical, this volume can be converted into an equivalent bubble diameter and a corresponding p.d.f., f_B, Eq.(20). An example of evaluated experimental data is illustrated by Fig.11.

An illustration of further measurement possibilities is given by Fig.12, where velocity data of an experiment with $\langle U_G \rangle$=2.1mm/s and $\langle U_W \rangle$=100.0mm/s are shown for a non-symmetric gas injection (series No.2 according Table 1). To give a realistic picture of the gas velocity distribution, the bubble repetition frequency has to be shown in the diagram, as well. By doing so it can be distinguished clearly, if the expected interval wherein the velocity will range is due to a real physical behavior (i.e. action of turbulence), or due to a limited number of available data.

Bubble diameter and volume flow

With the evaluated information about the local instantaneous gas velocity, there is the possibility of bubble volume reconstruction, as demonstrated by Eqs.(17)-(19). With the assumption that the bubble shape is approximately spherical, this volume can be converted into an equivalent bubble diameter and a corresponding p.d.f., f_B, Eq.(20). An example of evaluated experimental data is illustrated by Fig.11 of

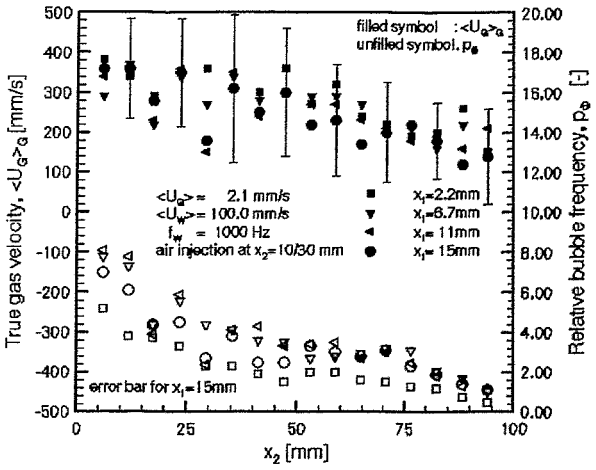

Figure 12 – $U_{G,G}$ distribution in A_c

the above-cited experiment. A significant peak value can be seen at approximate d_B=5.5cm. The bubble diameter mean value as well as the statistically (physically) expected interval, determined by the standard deviation, is given. Also uncertainty-bars of the p.d.f. are shown (not for moments). From Eq.(19) it follows directly that the evaluated diameter is directly proportional to the indicated velocity. In Eq.(19) the mean value of $\tilde{\tilde{p}}_u$ within U_δ have been used to evaluate the true rising velocity and thereby the true bubble volume. The possibility to plot the evaluated bubble diameters d_B in their spatial distribution over the cross-section A_c have been

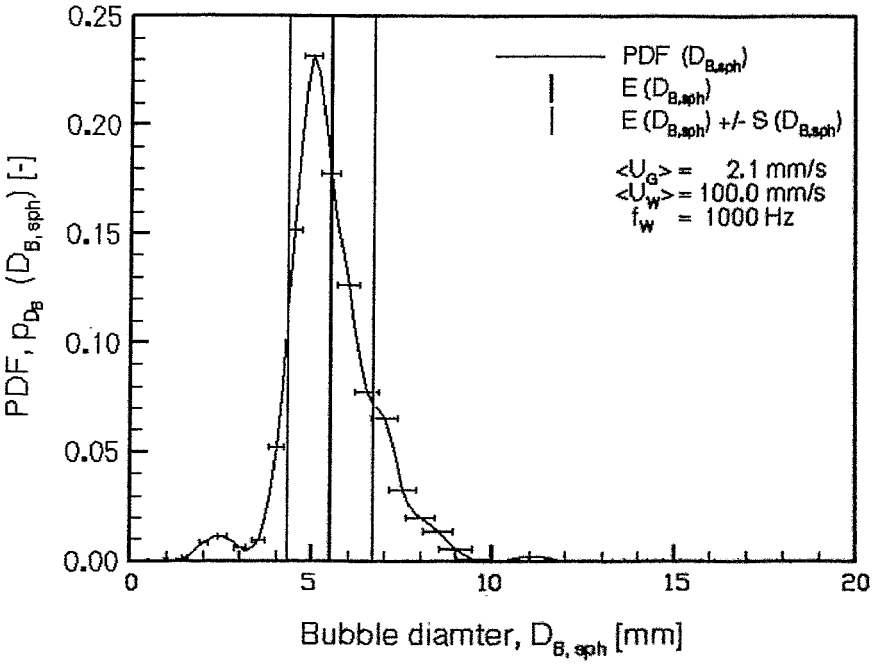

Figure 13 – Bubble diameter spectrum

realized in Fig.14 for the above described experiment with an non-symmetric air-injection ($\langle U_G \rangle$=2.1mm/s, $\langle U_W \rangle$=100.0mm/s and f_W=1000Hz). It can be seen from Fig.14 that the bubble diameter is approximately constant distributed over A_c. Since there are practical difficulties to obtain data of the bubble diameter from alternative experiments, the volume flow has been chosen as a suitable criterion to assess the quality of the reconstruction of bubble size in connection with the prediction of the velocity (wherefore the accuracy was discussed independently). By use of Eq.(21) the local volume flow and its equivalent in the flux velocity can be calculated. For the cited experiment, the local distribution of the superficial velocity over A_c is shown in Fig.15. Two strong maxima can be identified in the region of air injection (x_2=10,30mm). The volume flux outside this region is neglectable small. Furthermore, there is a connection between Fig.15 and the bubble diameter- as well as local the gas velocity distribution, given by Fig12 and Fig.14, respectively: The volume flow reaches maximum values in region, where big

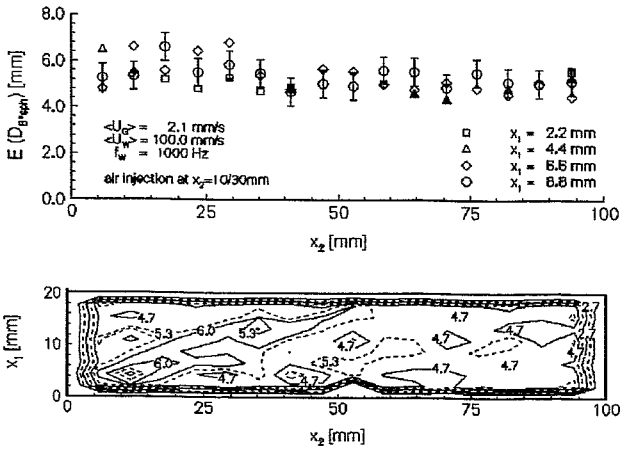

Figure 14 – Bubble diameter distribution

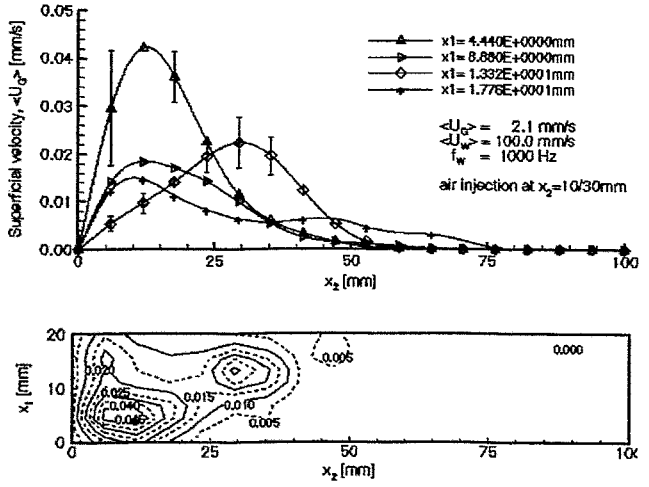

Figure 15 – Volume flux distribution

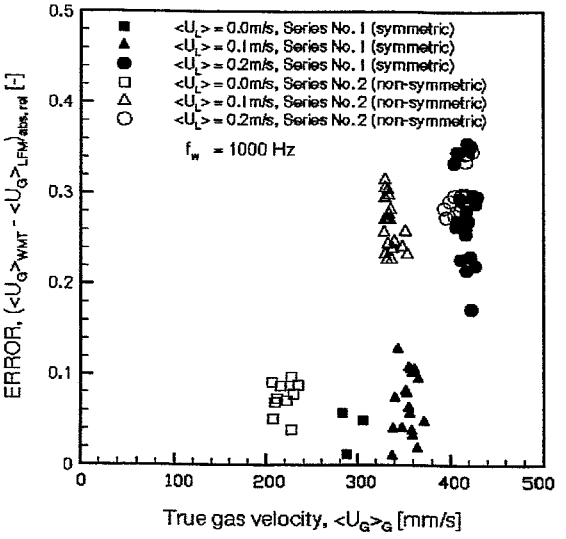

Figure 16 – Quality of $\langle U_G \rangle$ evaluation

bubbles migrate at high true velocities. The time and cross sectional averaged superficial velocity of the gas, $\langle U_G \rangle$, reconstructed from data supplied by the WMT, were compared to data alternatively obtained data by a laminar-flow meter, LFM. The deviation in these data is shown in Fig.16 in a plot vs. the cross-sectional and time averaged true gas velocity, $\langle U_G \rangle_G$. For low true gas velocities (<300mm/s) an error of less than 10% can be confirmed. For larger values of $\langle U_G \rangle_G$, there are relative deviations up to 30%. The reason for these deviations is seen by the authors in a strong bubble deformation as well as the invalidity of the assumption that the integral-surface velocity of the bubble can be assumed as equivalent to the velocity of the approaching surface, whereon the algorithm for the evaluation of the rising velocity is based. Also obvious is that the measuring accuracy is lower for non-symmetric injected bubbles. The bubble concentration per unit volume increases for the same superficial gas velocity in the case of non-symmetric injection and so the source for a measuring error is given in a similar way than for higher superficial velocities but homogeneous bubble distribution.
To improve the accuracy of these values, there is the necessity for further extensive research.

Accuracy and certainty

Prasser et al. [4] found that the new electrode-mesh sensor is able to predict the time and sectional-cross averaged void fraction with an accuracy of approximately 1%. Furthermore there is evidence in Prasser et al. [4] that the accuracy for the local void fraction measurement is similar in order than the integral value.

The measurement of the true gas velocity is based on the analysis of the delay-time between the two signals that a migrating bubbles causes at two peripheral electrode crossing points of the WMT. For the identification of these events a change in the local void fraction ($\Phi_{\varepsilon,pos}$) is used. This event is independent from the amplitude of the void fraction signal. Insofar it can be concluded that there is theoretically no error on the measurement of the delay-time's mean value, caused by a deviation in the void fraction measurement. This is not the case for the instantaneous delay-time: a deviation in the measurement of the void fraction of one point might cause a time shift of the ramp event, $\Phi_{\varepsilon,pos}$, in the triggered signal since a different sector, i.e. ε-thresh, of the ramp is utilized (compare Fig.4). But if it is supposed that the error in void fraction measurement is randomly symmetrically distributed around a mean value in time and space the statistical mean value of the delay time can be correctly reflected. Evidence of this assumption have been achieved by variation of the threshold value ε_{thresh}, used to trigger the raw signal from the noise. A variation in between ε_{thresh} = 9-12% did not yield any remarkable deviation in the evaluated delay time mean value Δt. (The time and cross-sectional averaged void fractions was larger $<\varepsilon>$=0.2%.)

Beside of the delay-time Δt, the electrode distance Δ_W is of importance. This discussion goes alone with the question of linearity in the conversion from a voltage level U_{el}, caused by the conductivity of the surrounding two-phase mixture, into a void fraction, ε. The electromagnetic field around two orthogonal spreads out wires, inside an artificially "0"-fixed electrical potential environment, is a very complex, 3 dimensional structure, which can not be recalculated by the obtained output signals [4],[5]. So it is supposed, as mentioned at the very beginning, that the output signal U_{el} is a function of the average distribution of the multiphase mixture in a volume, corresponding to one mesh size (2.22 x 6.06mm). This assumption seems to be valid since the mesh size is very small and the distance in between the wires is narrow. Furthermore the size of 1 mesh is limited since the interaction between the 2 excited electrodes is marginally low if all other electrodes are kept to 0 by low in and output impedance, respectively. Due to this - necessary – simplification, there is no possibility to take the wire distance or the influence of the stretched electromagnetic field into consideration. However, the legitimacy of this assumption is confirmed by the experiments for velocity measurement (Fig.11), where no deviation of predicted gas velocity values to a certain were obviously.

The strongest source of possible deviations, uncertainty, respectively, is given by the introduction of the interclass velocity distribution $\tilde{\tilde{p}}_u$ in order to overcome the difficulties with insufficient time resolution. The PDF $\tilde{\tilde{p}}_u$ is supposed to be equally distributed within U_i. Since there is no knowledge of the real characteristics of $\tilde{\tilde{p}}_u$ the worst case has to be assumed. This situation is given if in the first case all velocities u_j , belonging to U_i, are concentrated at the lower velocity value U_i. The other case is given if all velocities u_j are concentrated at U_{i+1}. Both cases are highly unlikely, but have to be considered as possible. The result is that for velocities closed to u_{max} (down to approx. $u_{max}/5$) an expected interval of up to 20% results. This uncertainty is less important for the prediction of the velocity mean value U as much more for the prediction of an instantaneous velocity u. The statistical mean value can be considered as within +/-5% correct (Fig.11), but the instantaneous value have to be assumed within the above mentioned larger interval. This is of particular interest for the calculation of equivalent bubble diameter (Fig.13) as well as volume flux (Fig.15), where the instantaneous value of the velocity is taken for calculation. Both cited figures show large uncertainty-intervals in which mean value is expected. Especially the plot of the superficial velocity distribution $<U_G>$ over the cross section A_c in Fig.15 illustrates this effect: in regions of low flux value ($(<U_G>)$ < 1mm/s), resulting from slow gas velocities (bubble diameters are approximately equally distributed over A_c) are less influenced by $\tilde{\tilde{p}}_u$ since the temporal resolution of the sensor is sufficient (interval about 3%). Areas of high flux values ($(<U_G>)$ > 3mm/s) are characterized by large uncertainties, (~10%) resulting from the approximation of the true velocity probability function p_u by use of $\tilde{\tilde{p}}_u$.

So it is not surprisingly that the prediction of the gas volume flow at standard condition suffers high deviation from the alternatively supplied data. As illustrated in Fig.16, the standard volume flow, expressed by the superficial velocity is reconstructed with a deviation lower 10% for bubble rising velocities, where the temporal resolution of the sensor is. Furthermore it have to be noted that an error occurs due to the slice-wise reproduction of a bubble in regions of higher rising velocities: as higher as faster as the bubble migrates as rougher the approximation of volume reconstruction according Eq.(19) seems to be. It have to be stated that the applicability of the sensor to volume flow modeling is lost for rising velocities higher than 300mm/s, where errors of about 30% were found. However, the authors sharing the opinion that these values will be significantly improved with further hardware development.

SUMMARY

A new electrode-mesh device has been applied to studies on bubble flow. Extensive data processing methods have been developed that offers the possibility to evaluate the local instantaneous void fraction, bubble rising velocity and bubble volume as well as their time and cross-sectional averaged values. These averages were used to conclude on the local distribution of the superficial gas velocity.
The proposed algorithms have been applied to bubble flow in a rectangular channel (A_c=20x100mm, $\langle U_G \rangle$=0-5mm/s,$\langle U_W \rangle$=0-25mm/s and two air injection configuration). Accuracy in the prediction of void fraction was found within 5% by comparison with video supplied data. The reconstructed volume flow showed uncertainties in the order of up to 10% for true gas velocities lower 300mm/s and up to 30% above.

NOMENCLATURE

A_C	Cross section	1 m²
C_0	Distribution coefficient	-
D	Standard deviation	-
d_B	Bubble diameter, spherical	1 m
D_B	Bubble diameter class	1 m
E	Mean value	-
f	Probability density function	-
f_W	Wire Mesh Tomograph, WMT, overall sampling rate	1 Hz
i,j,k,l,m, n,o	Counting variables	-
$\langle u_G \rangle$ $\langle U_G \rangle$	Superficial velocity of the gas (instantaneous/ time averaged)	1m/s
L	List	-
N	Number	-
p	Pressure	1 Pa
p	Probability density function, general	-
$\tilde{p}_u$	p.d.f. for equidistant velocity classes	-
$\tilde{\tilde{p}}_U$	p.d.f., locally restricted	-
P	Distribution function	-
$\vec{r}, \vec{s}$	Vectors in space R³	1 m
t	Time	1 s
T_i	Time class	1 s
T	Temperature	1 K
U_{el}	Voltage	1 V
u, U	True velocity (instantaneous,time averaged)	1m/s
U_i	Velocity class, general	1m/s
$\tilde{U}_i$	Velocity class, equidistant	1m/s
V_B	Bubble volume	1 m³
x_1, x_2	Coordinates in the cross-section	1 m
Φ	Ramp event	-
ε	Void fraction	-
δ	Delay frames	-
Δ_W	Distance between measuring planes	1 m

Superscript

0	Normalized or referring standard condition
A	Referring air
k, κ	List counter
W	Referring water

Subscript

δ	Referring delay frame number
ε	Referring void fraction
B	Referring bubble
i,j,k,l,m,n,o	Counting variables
LFM	Referring laminar flow meter
max	Maximum
req	Required
sph	Spherical (equivalent)
thresh	Threshold
T	Referring time delay
U	Referring velocity
Video	Referring video
WMT	Referring Wire-Mesh Sensor
X1, X2	Referring coordinates in the cross section

REFERENCES

[1] Hori, K., Fujimoto, T., Kawanishi,H., Nishikawa,H., Advanced high speed X-ray CT scanner for measurement and visualization of multi-phase flow. In: *OECD/CSNI Specialist meeting on Advanced Instrumentation and Measurement Techniques*, Santa Barbara, USA, March 17-20, 1997.

[2] Kataoka,I., Serizawa,A. Statistical behaviors of bubbles and its application to prediction of phase distribution in bubbly two-phase flow. In: *The International Conference on Multiphase Flows '91,* Tsukuba, Japan, September 24-27, 1991, 459-461.

[3] Mercier,J., Lyrio,A., Forslund,R. Three-dimensional study of the non-rectilinear trajectory of air bubbles in rising water. *Transaction of the ASME - Journal of Applied Mechanics*, 1973, 650-654

[4] Prasser, H.-M., Böttger, A., Zschau, J., A new electrode-mesh tomograph for gas-liquid flow. *Flow Measurement and Instrumentation*, 1998, **9**, 111-119.
[5] Reinecke,N., Mewes,D., Recent developments in industrial research application of capacitance tomography. *Measurement Sci. Technol.*, 1997, **7**, 233-246.
[6] Sadatomi,M., Sato,Y. Two-phase flow in vertical non-circular channels. *Int. J. Multiphase Flow*, 1982, **8**, 641-655.
[7] Zuber,N., Findlay,J.A., Average volumetric concentration in two-phase flow systems. *J. Heat Transfer*, 1965, **87**, 453-468.

4. Workshop - Final Programme

Measurement techniques for stationary and transient multiphase flows

16.-17. November 2000 / Rossendorf

16 November

10:00 Welcome, ***F.-P. Weiss***

Ultrasonic methods

10:15 ***M. Aritomi, H.Kikura, Y.Suzuki*** *(Tokyo Institute of Technology)*: Ultrasonic doppler method for bubbly flow measurement

11:00 ***V. V. Kontelev, V. I. Melnikov*** *(TU Nishny Novgorod)*: An ultrasonic mesh sensor for two-phase flow visualisation

11:30* ***A. Dudlik, H. Fahlenkamp*** *(Fraunhofer UMSICHT)*: Fast measurement of the liquid flow rate in pipelines

12:00 ***A. V. Duncev*** *(TU Nishny Novgorod)*: Waveguide ultrasonic liquid level transducers for power generating equipment

Optical Methods

12:30* ***A. Breuer*** *(TSI)*: Recent developments in laser doppler measurements

13:00 Lunch

Optical Methods (cont.)

14:00* ***R. Maurus, T. Sattelmayer*** *(TU Munich)*: Study of bubble behaviour in subcooled flow boiling using high-speed cinematography and digital image processing algorithms

Wire-mesh sensors (1)

14:30** ***H.-M. Prasser*** *(FZR)*: Wire-mesh sensors - function, flow visualisation and measurement of gas fraction profiles, bubble sizes and bubble velocities

15:15 Coffee break

16:00 ***D. Scholz, C. Zippe*** *(FZR)*: Validation of bubble size measurements with wire-mesh sensors by high-speed video observation

16:30 ***A. Manera, W.J.M. de Kruijf, T.H.J.J. van der Hagen, R.F. Mudde, H. Hartmann*** *(TU Delft, IRI)*: Low-pressure dynamics of a natural-circulation two-phase flow loop.

17:30 Individual discussions, visits to test facilities of FZR:

- Coolant mixing in PWRs
- Water hammers and cavitation in pipes
- Two-phase flow pattern

20:00 Open discussion: "Burghotel Stolpen"

17 November

Impedance & others

09:00 ***H. Schmidt, O. Herbst, W. Kastner, W. Köhler*** *(Siemens AG KWU)*: Measuring methods for the investigation of the flow phenomena during external pressure vessel cooling of the boiling water reactor SWR1000

09:30 ***A. Traichel, W. Kästner, S. Schefter, V. Schneider, S. Fleischer, T. Gocht, R. Hampel*** *(HTWS Zittau/Görlitz - IPM)*: Verification of simulation results of mixture level transients and evaporation processes in level measurement systems using needle-shaped probes

Wire-mesh sensors (2)

10:00* ***T. Lex, F. Hoselt, T. Sattelmayer*** *(TU Munich)*: Flow visualisation and pressure losses of a gas liquid flow through a continuously closing globe valve

10:30 Coffee break

11:15 ***S. Richter, M. Aritomi*** *(Tokyo Institute of Technology)*: Methods for studies on bubbly flow characteristics applying a new electrode-mesh tomograph

11:45** ***J. Zschau*** *(FZR)*: Fast wire-mesh sensors with 10,000 frames / s

12:15 End - time for more discussions & visits

* No print version of the paper submitted

** The presentations of H.-M. Prasser and J. Zschau are merged to one paper in the proceedings: ***H.-M. Prasser, E. Krepper, D. Lucas, J. Zschau*** *(FZR)*, ***D. Peters, G. Pietzsch, W. Taubert, M. Trepte*** *(Teletronic Ingenieurbüro GmbH)*, Fast wire-mesh sensors for gas-liquid flows and decomposition of gas fraction profiles according to bubble size classes.